EFFECT OF DOPANT SIZE ON ANELASTIC RELAXATION IN SOLID STATE IONICS WITH FLUORITE STRUCTURE

A Dissertation

by

AMY MARIE BOLON

Submitted to the Office of Graduate and Professional Studies of
Texas A&M University
in partial fulfillment of the requirements for the degree of

DOCTOR OF PHILOSOPHY

Chair of Committee,	Miladin Radovic
Committee Members,	Raymundo Arroyave
	Tahir Cagin
	Hong Liang
Head of Department,	Ibrahim Karaman

December 2016

Major Subject: Materials Science and Engineering

ABSTRACT

Solid State Ionic (SSI) materials are key materials for devices where high ionic diffusivity and conductivity are crucial for their proper operation. The most common SSI materials for these applications are doped zirconia or ceria based materials, with yttria-stabilized zirconia (YSZ) being the benchmark one. The mechanical properties are extremely important for their use as electrochemical devices which frequently operate under high temperature, mechanical stresses, electric fields and reducing or oxidizing environments. In this study, Resonant Ultrasound Spectroscopy (RUS) is used to evaluate the mechanical properties of these materials at high temperature and under electric fields.

A high temperature RUS system was developed for measuring moduli of solids from room temperature up to 1300 °C in controlled environments. Elastic moduli of different materials were obtained using high temperature RUS and were statistically analyzed and systematically compared to the values obtained using other high temperature techniques. This system was used for the remainder of the study.

The elastic properties of polycrystalline Yttria-stabilized Zirconia (YSZ), Scandia-Ceria-Stabilized Zirconia (SCZ) and Gadolinia Stabilized Zirconia (GSZ) were analyzed using Resonant Ultrasound Spectroscopy (RUS) in air, from room temperature up to 1000 °C. In all samples, the both Young's and shear moduli were found to decrease significantly, i.e. for up to ~50%, in the 250 °C to 600 °C. In the same temperature range, two major frequency dependent attenuation (Q^{-1}) peaks are observed

that can be attributed to the anelastic relaxation of oxygen vacancy – cation complexes. Assuming single Debye relaxation model, activation energies for the anelastic relaxation were calculated and a linear trend of increasing activation energy with increasing ionic radii mismatch was observed. The effect of dopant cation (Gd^{3+}, La^{3+}, Sm^{3+}, and Y^{3+}) on elastic properties and anelastic relaxation of doped ceria. For comparison, elastic properties of pure stoichiometric ceria (CeO_2) and reduced ceria ($CeO_{2-\delta}$) were also examined. It was found that although the elastic moduli decrease monotonically with temperature, Q^{-1} shows a frequency dependent maximum at different temperatures ranging from 100 °C to 300 °C for differently doped ceria. Unlike the doped zirconias, only a slight trend was observed in the activation energy for anelastic relaxation due to the more complex defect clusters that can form in doped ceria.

The mechanical damping peaks produced by RUS of 8 mol% yttria stabilized zirconia (8YSZ) were further studied to understand the number of relaxation mechanisms occurring within the material. The previous assumption of two Debye peaks did not match the data when the relaxation curves were reconstructed. It was found that a six peak model minimized the RMS error between the reconstructed curve and the experimental data. In addition, 8YSZ was studied under electric fields of 0 V/mm, 50 V/mm, 100 V/mm and 150 V/mm. It was observed that the elastic moduli become stiffer as a result of the applied electric field. The mechanical damping curves change slightly as a result of some defect clusters becoming frozen in place while others are more likely to move.

DEDICATION

To my parents, thank you for all your support.

CONTRIBUTORS AND FUNDING SOURCES

This work was supported by a dissertation committee consisting of Dr. Miladin Radovic and Dr. Raymundo Arroyave and Dr. Tahir Cagin of the Department of Materials Science and Engineering and Professor Hong Liang of the Department of Mechanical Engineering.

The DMA data analyzed in Section 3 was provided by Dr. Peipei Gao who also performed part of the analysis. All other work conducted for the dissertation was completed by the student independently.

Graduate study was supported by a U.S. National Science Foundation (CAREER Award: DMR-1057155), which provided the funding for the research.

NOMENCLATURE

1NN	Nearest neighbor
2NN	Next nearest neighbor
8YSZ	8 mol% Yttria Stabilized Zirconia
10GDC	10 mol% Gadolinia Doped Ceria
10YSZ	10 mol% Yttria Stabilized Zirconia
20GDC	20 mol% Gadolinia Doped Ceria
Al_2O_3	Aluminum oxide (Alumina)
CeO_2	Cerium oxide (Ceria)
CaSZ	Calcia stabilized zirconia
DMA	Dynamic Mechanical Analysis
E	Elastic modulus
E/E_{RT}	Normalized elastic modulus
EXAFS	Extended X-ray absorption fine structure
f	Frequency
FWHM	Full width at half maximum
G	Shear modulus
Gd_2O_3	Gadolinum oxide (Gadolinia)
GSZ	Gadolinia stabilized zirconia
H_a	Association enthalpy
HT-RUS	High temperature Resonant Ultrasound Spectroscopy

IR	Infrared
LDC	Lanthana doped ceria
NDC	Neodymia doped ceria
NDT	Non-destructive technique
NMR	Nuclear magnetic resonance
PZT	Lead zirconate titanate
Q^{-1}	Mechanical damping or attenuation
r_c	Critical ionic radius
r_d	Dopant radius
RMS	Root mean square error
RUS	Resonant Ultrasound Spectroscopy
ScDC	Scandia doped ceria
SCZ	10 mol% Scandia, 1 mol% Ceria Stabilized Zirconia
SDC	Samaria doped ceria
SOFC	Solid oxide fuel cell
SSI	Solid state ionics
SSZ	Scandia stabilized zirconia
Y_2O_3	Yttrium oxide (yttria)
YSZ	Yttria stabilized zirconia
ZrO_2	Zirconium oxide (zirconia)
Δ	Relaxation strength
τ	Relaxation Time

TABLE OF CONTENTS

Page

LIST OF FIGURES

Page

LIST OF TABLES

Page

1. INTRODUCTION

1.1 Background

1.1.1. Doped Zirconias and Cerias

Solid State Ionic (SSI) materials are key materials for devices where high ionic diffusivity and conductivity is crucial for their proper operation[1-8]. Nowadays, SSIs are widely used in Solid Oxide Fuel Cells (SOFCs), gas sensors, batteries and gas separation membranes[2, 4, 5, 9]. The most common SSI materials for these applications are doped zirconia or ceria based materials, with yttria-stabilized zirconia (YSZ) being the benchmark one[2, 4, 10-12]. High ionic diffusivity and conductivity in these materials can be achieved in one of two ways: (1) doping with aliovalent dopants that introduces oxygen vacancies in the host material while maintaining charge neutrality or (2) changing the stoichiometry of the material through reduction or oxidation[5].

Zirconium Oxide, ZrO_2, is a polymorphic material with three main crystal structures at different temperatures. At room temperature, ZrO_2 has a monoclinic structure with C_{2h}^5 symmetry and a centrosymmetric space group $P2_1/c$. At approximately 1400 K, it transforms to tetragonal structure with D_{4h}^{15} symmetry and centrosymmetric space group $P4_2/nmc$. Then, at 2650 K it transforms into the cubic fluorite phase with O_h^5 symmetry and centrosymmetric space group $Fm3m$ [13]. If some of the tetragonal structure is present at room temperatures, such as in tetragonal or partially stabilized zirconia, it results in shape memory effect or significant transformation toughening[14-16]. Due to the large volume expansion ZrO_2 undergoes

during heating because of those phase transformations, it is important to stabilize its high temperature cubic phases down to the room temperature. This can be done with the addition of aliovalent dopants, such as scandia[17], calcia[18, 19], samaria[17], gadolinia, ytterbia[17], magnesia[20, 21], and yttria[1, 17, 22]. The most commonly, ZrO_2 are doped with more than 8 mol% yttrium oxide (Y_2O_3) to stabilize cubic structure [22-25]. Y_2O_3 is cubic with a body centered space group $T_h^7\left(Ia\bar{3}\right)$[13]. In the stabilized fluorite phase, the zirconium, Zr^{4+}, or yttrium, Y^{3+}, ions site on the FCC lattice sites while the oxygen ions or oxygen vacancies occupies tetragonal sites[26].

More importantly, stabilization of the cubic fluorite phase with aliovalent cations also introduces oxygen vacancies that can be exploited for use in SSIs where the oxygen vacancies act as charger carriers through the material. While the addition of aliovalent dopants increases the ionic conductivity due to increased number of oxygen vacancies, there is a maximum amount of dopant that results in a maximum ionic conductivity for a particular doped system. For example, **Figure 1.1a** shows the effect of increasing the amount of yttria on the ionic conductivity of zirconia at 800 °C with the clear maxima in ionic conductivity at approximately 8-10 mol% Y_2O_3. This drop in ionic conductivity at higher doping concentrations is related to complex defect (oxygen vacancies and dopant cations) ordering, vacancy clustering and/or electrostatic interactions[10]. **Figure 1.1b** shows the effect of dopant type on the ionic conductivity at 800 ºC for three of the more common dopants. There is a clear trend that the ionic conductivity decreases as the dopant ion gets larger.

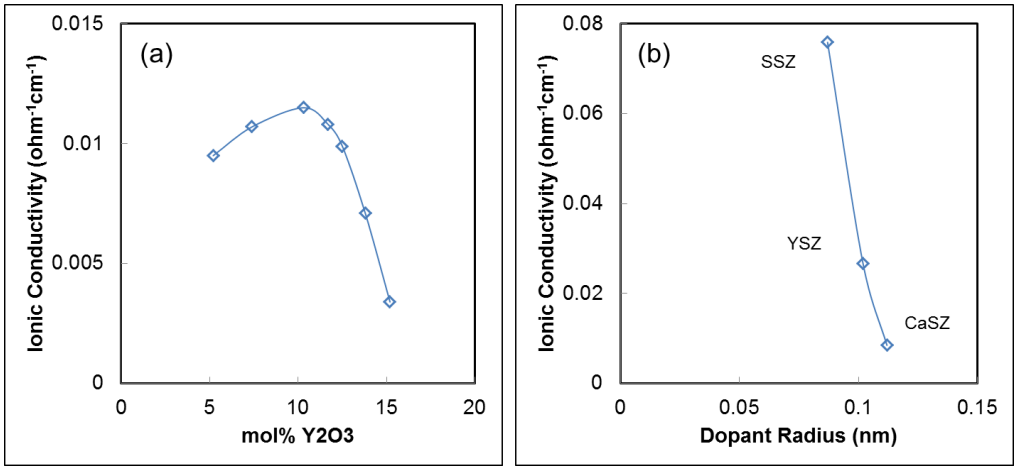

Figure 1.1. (a) Effect of Y2O3 dopant concertation on ionic conductivity of ZrO2 at 800 °C and (b) change of ionic conductivity of zirconia with different types of dopants at 800 °C where SSZ, YSZ, and CaSZ are scandia, yttria and calcia respectively, doped zirconias.

Similar to zirconia, cerium oxide, CeO_2, can be doped with different dopants, such as samaria[27-30], scandia[31], gadolinia[32-35], yttria[2, 36-39], lanthana[34, 40, 41] ytterbia[34], and neodymia[34] to increase the ionic conductivity by adding oxygen vacancies into the crystal lattice[42]. Unlike zirconia, ceria has cubic fluorite (Fm3m) from room temperature to melting temperature so there is a far greater range of aliovalent dopants and dopant concentrations that can be used[43] to increase concentration of oxygen vacancies and thus ionic conductivity in doped cerias. **Figure 1.2b** shows the effect of changing the dopant type on the ionic conductivity of ceria at 800 °C. Here four dopant with different the ionic radii is used to illustrate the effect of the dopant size on the ionic conductivity. In **Figure 1.2b**, the ionic conductivity again increases with increasing dopant radius, and after that decreases again. To understand effect of the dopant size on

ionic conductivity, one has to understand effect of the doping on elastic strain in introduced in the host lattice by doping with aliovalent cations with different size.

The addition of different sized dopants introduces elastic strain into the crystal lattice by causing distortions in the lattice. It has been previously shown that doping cations that produce smaller lattice distortions tend to produce high conductivities because due to the effect of dopant-vacancy associations[44, 45]. Gerhardt-Anderson et al.[44] show that the association enthalpy between dopant and oxygen vacancy is much stronger when there is a larger mismatch between dopant ionic radius and host radius. A model developed by Kim[46] predicts the elastic strain as a function of ionic radii difference between the host and dopant atom be developing a model to determine the critical radius size, r_c, for a trivalently doped cation in a MO_2 host. For ceria the critical ionic radius was determined to be 1.038 Å[43, 47]. Previous work has shown that Gd^{3+} has the closest ionic radius to r_c and the highest ionic conductivity[2, 32, 48]. Similar work has been done for trivalently doped zirconia, and the critical ionic radius has been determined to be 0.0948 Å[46]. **Figure 1.2** illustrates how the ionic conductivity is maximized when the difference between the dopant ionic radius (r_d) and the critical ionic radius (r_c) is minimized. It can clearly be seen in **Figure 1.2** that small difference in ionic radii of the host and dopant in GDC and SDC results in the highest ionic conductivity, when compared to other doped cerias and zirconias.

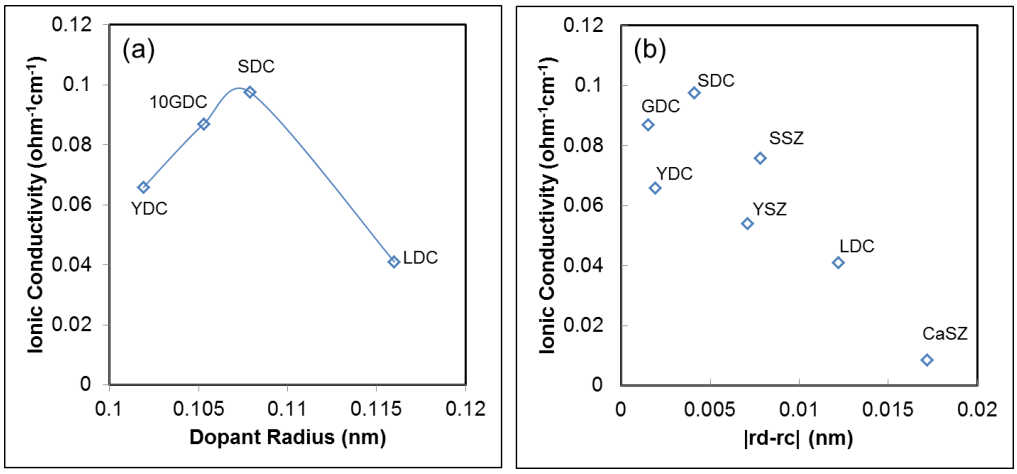

Figure 1.2. (a) The change of ionic conductivity of zirconia with different types of dopants at 800 °C where YDC, 10GDC, SDC and LDC are yttria, 10 mol% gadolinia, scandia, and lanthana respectively, doped cerias and (b) ionic conductivity as a function of the difference between the critical ionic radius and the dopant ionic radius at 800 °C

In addition, unlike doped zirconia, doped ceria is prone to easy reduction. As oxygen leaves ceria in in reducing environments forming oxygen vacancy, it is thermodynamically favorable for Ce^{4+} reduces to Ce^{3+} [49]. This reduction in valency is accompanied by a large increase in ionic radius from 0.97 pm to 1.143 pm which can cause micro-cracks in the material[50]. Using the Kroger-Vink notation, the reduction of ceria can be written as:

$$2Ce_{Ce}^{x} + O_{O}^{x} \leftrightarrow V_{O}^{\bullet\bullet} + 2Ce_{Ce}^{'} + 1/2\,O_{2}(g) \quad [51] \qquad \textbf{(1.1)}$$

In addition to the size change, CeO_2 starts becoming more electrically conductive when it is reduced[6]. However, this reduction results significant volumetric changes (up to 4%) that in turn might lead to large stresses and microcracking of ceria during reduction-oxidation cycle[50, 52-54]. the later can be especially problematic for applications like

SOFCs where the anodic side of the cell is exposed to low oxygen partial pressures. As a way to combat this problem, either a thin layer of 8YSZ is coated on the ceria or a mixture of 8YSZ or 3YSZ is made with the doped ceria[6].

1.1.2. Defect Complexes

Aliovalent dopants increase the number of oxygen vacancies which act as charge carriers in the material, thus enhancing oxygen diffusivity and ionic conductivity. The oxygen vacancies are formed to maintain charge neutrality in the material as shown here in the Kroger-Vink nomenclature[55]:

$$R_2O_3 \xrightarrow{MO_2} 2R_M^{'} + V_O^{\bullet\bullet} + 3O_O^x \qquad \textbf{(1.2)}$$

where R represents the doping aliovalent cation, typically a rare-earth element and M represents the host cation. Oxygen vacancies can place themselves on different sites in oxygen sublattice, having dopants in nearest (1NN) or next nearest (2NN) positions, as it is discussed in more details in the subsequent sections.

Initial models for atomic placement have suggested that the oxygen vacancies introduced by doping tend to sit in the site with the dopant ion as the nearest, **Figure 1.3**. This model is based on electrostatic attraction between oppositely charged dopant ion and the oxygen vacancy and the defect symmetry the oxygen vacancy introduces[56]. According to Wachtman's model[57], the oxygen vacancy occupies one of the eight nearest neighbors surrounding the dopant ion, **Figure 1.3**. The insertion of the trivalent dopant and the subsequent oxygen vacancy cause local elastic distortions and disrupts the symmetry of the host cell. Nowick et al.[58, 59] showed in numerous studies that that

the defect symmetry of this defect cluster is trigonal doped in cubic ceria and zirconia, thus lowering local symmetry of the otherwise centrosymmetric fluorite structure.

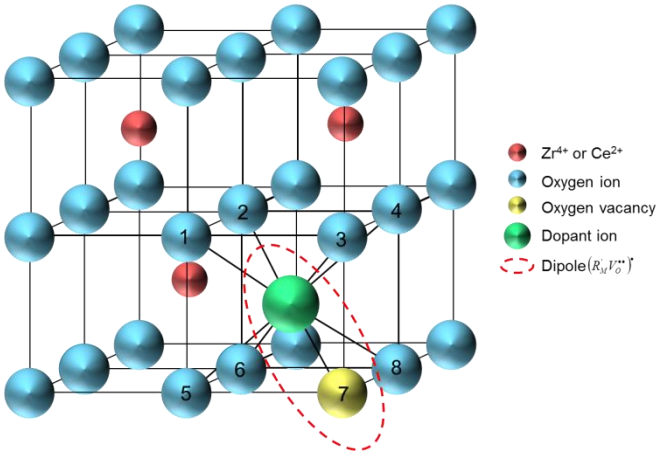

Figure 1.3. Fluorite structure after adding a dopant to the ceria or zirconia host lattice, showing oxygen vacancy in the nearest neighbor position (1NN)

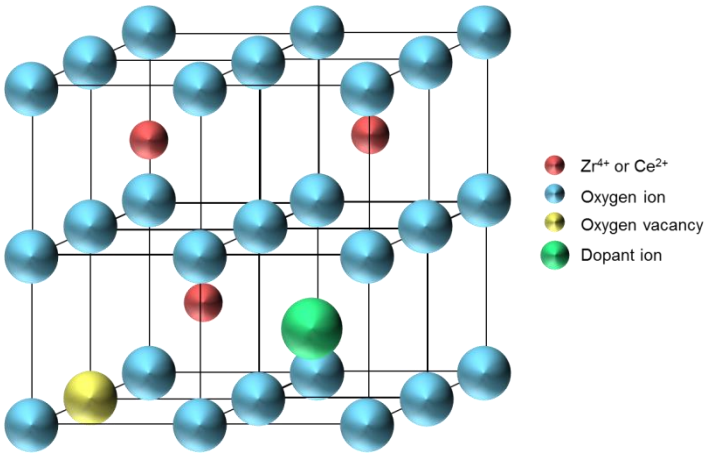

Figure 1.4. Fluorite structure after adding a dopant to the ceria or zirconia host lattice, showing oxygen vacancy in the next nearest neighbor position (2NN)

According to several recent computation studies, the Y^{3+} ions preferentially occupies site second (or next) nearest neighbors (2NN) site relative to the oxygen vacancies[60, 61]. Extended X-Ray Absorption Fine Structure (EXAFS)[62-64], neutron diffraction[65] and Nuclear magnetic resonance (NMR)[66] studies have shown that the Y^{3+} ions sit on 2NN sites to the oxygen vacancy while the Zr^{4+} ions sit at nearest neighbor (1NN) sites to the oxygen vacancy, as it is illustrated in **Figure 1.4**. Additionally, the computational studies show that the oxygen vacancies prefer the third nearest neighbor (3NN) position to each other along the <111> direction[61, 67]. There are two prevailing theories that explain 2NN configuration. Work published by Bogicevic and Wolverton[68] suggests that the elastic interaction between the dopant ion and oxygen vacancy is repulsive, causing the dopant ion and vacancy to sit in the second nearest neighbor position relative to the dopant. The other explanation is 2NN configuration in doped ceria and zirconia leads to more stable eightfold O^{2-} coordination of the Y^{3+} similar to its coordination in Y_2O_3 and sevenfold O^{2-} coordination around the Zr^{4+} ion that is NN to a vacancy similar to its coordination in the preferred low temperature monoclinic phase[13, 69].

Additional studies on stabilized zirconia show a trend in the type of dopants on the structure of the vacancy-dopant clusters. Trivalent metal dopants typically have a smaller radius than the Zr^{4+} ions and favor NN positions around the oxygen vacancies and do not necessarily stabilize the cubic phase at low temperatures due to its sevenfold coordination. However, larger dopants prefer the 2NN site and stabilize the cubic phase at lower temperatures due to their eightfold coordination[69]. According to those studies,

the point at which tendency of dopant ions to occupy NN position changes to 2NN positions is at approximately the radius dopant being equal to that of the Zr^{4+} ion[69].

Significantly smaller number of studies examined vacancy clustering and ordering in doped ceria. Ahn et al[42] studied position of oxygen vacancies in gadolinia-doped ceria using DFT with exchange-correlation energy function treated by Perdew–Burke–Ernzerhof (PBE) analysis within the generalized gradient approximation (GGA). They concluded that it was energetically more favorable for the vacancy and dopant ion to be in first nearest neighbor (1NN) positions under every strain condition. Nakayama et al.[70] performed a first principles DFT study and concluded that the smaller dopant ions sit NN to the oxygen vacancies while larger dopant ions sit 2NN to the oxygen vacancies and the crossover point is at approximately the ionic radius of Gd^{3+}. Experimental results from Kossey et al.[71] show through EXAFS studies of thin films that his may not be the case and the oxygen vacancy sits NN to ceria ions instead. Inaba et al.[72] performed molecular dynamics simulations that agreed with the EXAFS results showing that the oxygen vacancy prefers to be NN to ceria at low temperatures. However, at high temperature, it has a tendency to form Gd-Gd pairs within the system and be nearest neighbor to an oxygen vacancy especially[72].

1.1.3. Relaxation of Defect Complexes

Anelastic relaxation is a time-depended response of a material when it is exposed to the external stress field. In this case for ceria and zirconia materials, anelastic relaxation is proposed to be result of the stress induced reorientation of point defects

introduced into the material by doping. As mentioned in the previous section, the addition of dopants into a CeO_2 or ZrO_2 lattice also introduces oxygen vacancies to maintain charge neutrality. According to the model by Nowick, et.al[58, 59], at low temperatures, these oxygen vacancies are thought to be trapped by the dopants whose radii are different from host or dopant cations. In dilute solutions simple oxygen vacancy-dopant complexes form $\left(R_{Zr}^{'}V_O^{\bullet\bullet}\right)^{\bullet}$ as illustrated in **Figure 1.3**.

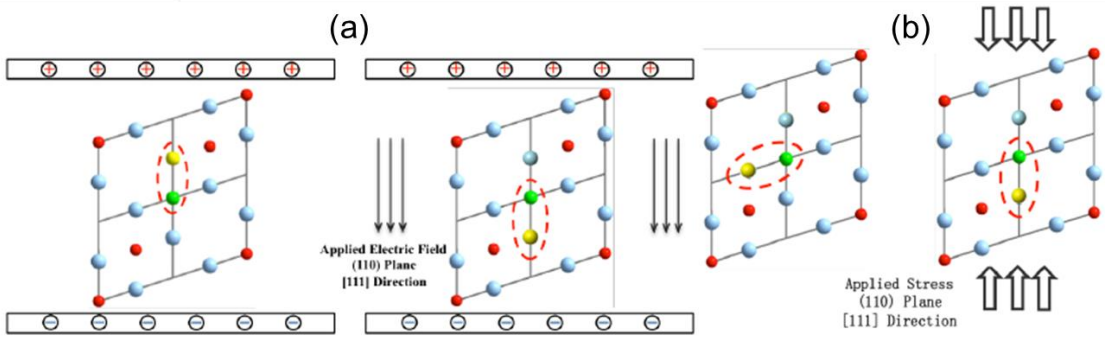

Figure 1.5. Reorientation of oxygen vacancy under (a) an electric field and (b) under an applied stress for the cluster presented in Figure 1.2.

These complexes are also electric dipoles that are associated with the partial separation of effective charges [73]. When an alternating electric field is applied, the electric dipoles will reorient by the oxygen vacancy "hopping" around the dopant ion in what is a thermally activated, reversible, time, temperature and frequency dependent reorientation process, illustrated in **Figure 1.5a**. This process was first proposed by Breckenridge et al.[74] in 1948 and a significant amount of work has been done to study it

in doped zirconia and ceria since then[75-78]. As the amount of dopant is increased, more complex oxygen vacancy-dopant complexes, such as $\left(2R_{Zr}^{'}V_{O}^{\bullet\bullet}\right)^{x}$ or more complex clusters, can form[31, 79].

However, it has been also been hypothesized that external stress can reorient the oxygen vacancy-defect complexes as well. In this case, under a zero stress or electric field condition, the vacancy has an equal probability of occupying any one position around host or dopant. However, once a stress field is applied, the hopping of the oxygen vacancy around the cation becomes preferential in one direction, as it is illustrated in **Figure 1.5b**. Therefore, this anelastic relaxation under alternating stresses is an analog to dielectric relaxation under an electric field.

The insertion of the trivalent dopant and the subsequent oxygen vacancy cause local elastic distortions, it also disrupts the symmetry of the host cell. Nowick et al.[58, 59] have done numerous studies to show that the defect symmetry is trigonal for defects in cubic ceria and zirconia, thus lowering symmetry of the otherwise centrosymmetric fluorite structure.

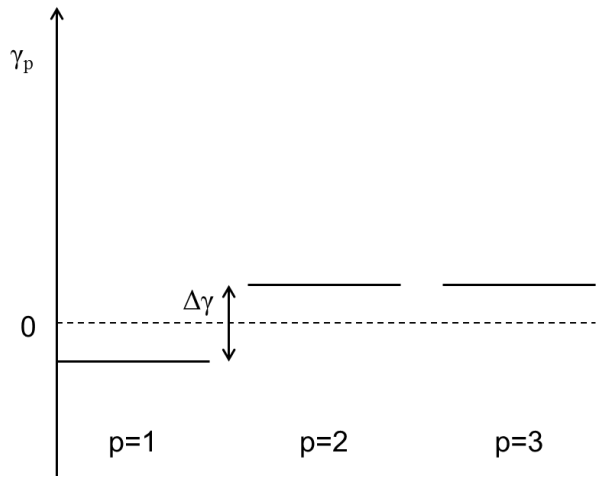

Figure 1.6. Free energy level splitting under a stress field, zero line indicates where levels would be under no external field

One of the conditions for anelastic relaxation is that the symmetry that results from the defect is lower than the symmetry of a perfect crystal[80]. Since trigonal symmetry is lower than cubic symmetry, anelastic relaxation occurs in this system. To characterize anelastic behavior in a homogeneous stress field, like the ones produced in this study, one only needs to know the symmetry of the system[80]. However, unlike the electric dipole which can be characterized by a vector, the elastic dipole is characterized by a second-rank tensor, λ[80]. The λ-tensor that characterizes the elastic dipole is related to the strain produced by point defects, as a result it is symmetric and results in three mutually perpendicular axes that can be used to characterize the relaxation strength and relaxation time in the material[80]. When small stresses are added to the system, the strain is equal to the elastic strain plus anelastic strain, $\varepsilon = \varepsilon^{el} + \varepsilon^{an}$ causing the λ-tensor to lose its symmetry. This in turn causes a change in the free energy levels,

$\gamma_p = -v_o \cdot \lambda^{(p)} \cdot \sigma$ of atomic sites which makes some site more favorable for the defect to "hop" into, **Figure 1.6**. Further derivations by Nowick et al.[80, 81], not included here, have been done to fully characterize the relaxation strength and relaxation time of trigonal defects in cubic crystals. The relaxation strengths depend on the orientation of the defect symmetry in the crystal and the strength of the Young's modulus relaxation increases as the strength of the shear modulus relaxation decreases. In addition, the relaxation time depends on the reorientation frequency and can be calculated by $\tau^{-1} = 4\nu$[81]. From the equation, it can be seen that the relaxation time does not depend on the stress levels or a splitting of energy levels, only on reorientation frequency[81].

This study uses mechanical spectroscopy to understand anelastic relaxation or internal friction in doped cerias and zirconias. Mechanical spectroscopy can be defined as an "absorption spectroscopic technique" where a mechanical oscillating stress with frequency f interacts with a solid and the mechanical energy absorbed by that solid is measured[81]. This will provide information about the microsturcture of the solid as well as the mechanisms controlling the mobility of the point defects in the solid.

Typical mechanical specectroscopy experiments, like those done by Weller et al.[76], Gao et al.[82] and Lakki et al. [83] result in two internal friction peaks due to the defect motions in the material. **Figure 1.7** shows two internal friction curves at 0.1 and 50 Hz measured Gao et al.[82] using DMA up to 600 °C. Two peaks can be clearly observed that shift to higher temperature with increasing frequency. These two peaks which relate to the defect motion under a stress field and are typically described by a Debye peak. The Debye peak can be calculated by

$$Q^{-1} = \Delta \frac{\omega\tau}{1+\omega^2\tau^2} \quad \textbf{(1.3)}$$

where Δ is the relaxation strength, ω is the frequency and τ is the relaxation time.

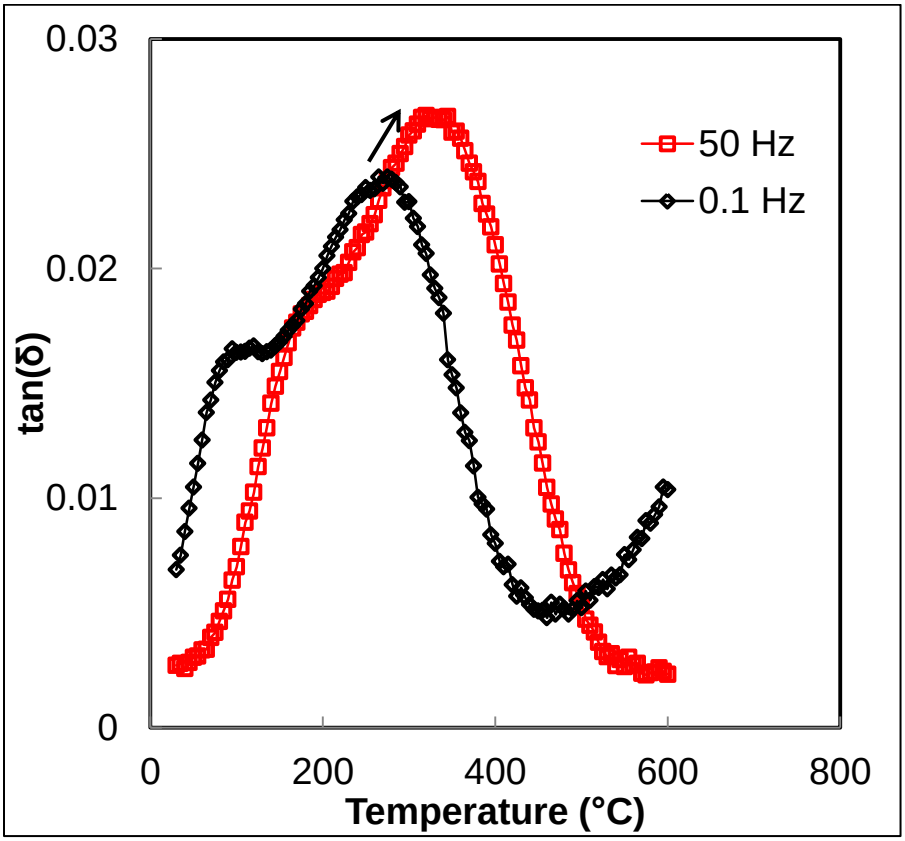

Figure 1.7. Typical mechanical loss spectra for doped ceria and zirconia showing two internal friction peaks at two different frequencies. The frequency shift to higher temperatures indicates that this process is frequency dependent. Reproduced from DMA data by Gao et al.[82]

This can be used to study anelastic relaxation by understanding the underlying atomic motions with and without a stress field. Anelastic relaxation is a thermally activated process and an be explained using an Arrhenius relationship:

$$\tau = \tau_O \exp\left(\Delta G_O \big/ kT\right) \quad \textbf{(1.4)}$$

where τ is the relaxation time, k is Boltzmann constant, T is temperature in Kelvin and ΔG_O is the energy to overcome the barrier at equilibrium. In a zero stress state, defects are in an equilibrium position corresponding to a local energy minimum with an energy barrier of ΔG_O, **Figure 1.8a.** Once a stress field is applied, one position becomes more favorable for the defects to sit in and will move to that position resulting in an anelastic deformation strain, ε^{an}. The result of applying a stress will also unbalance the energy diagram in one direction, **Figure 1.8b.** The effective energy barrier reduces to:

$$\Delta G = \Delta G_O - bA\sigma^* \quad \textbf{(1.5)}$$

where A is the activation area, and σ* is the difference between the applied stress and the internal stress.

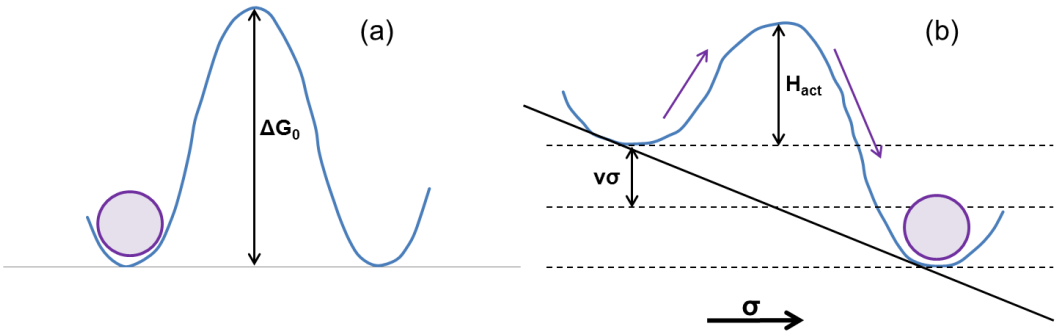

Figure 1.8. Thermally activated jumps across an energy barrier under (a) no stress field and (b) an external stress field[81]

From thermodynamics, $\Delta G = \Delta H - T\Delta S$, in this case, one can assume the entropy is small and neglect the term which results in:

$$H_{act} = \Delta H_O - bA\sigma * \quad \textbf{(1.6)}$$

where H_{act} is the activation enthalpy of the system. The relaxation time of the stressed system can finally be expressed as

$$\tau = \tau_O \exp\left(H_{act}/kT\right). \quad \textbf{(1.7)}$$

When modeling anelastic or dielectric relaxation peaks using single Debye relaxation model, one typically assumes that the number of possible relaxation mechanisms is directly related to the number of relaxation peaks observed[58]. When using the nearest neighbor model championed by Wachtman[57] and Nowick[59], one peak would be clearly due to $\left(R_{Zr}^{'}V_O^{\bullet\bullet}\right)^{\bullet}$ defect complexes and the second peak would be due to either more complex defect complexes or local ordering of oxygen vacancies, as it was previously suggested in the case of doped ceria and zirconia.

1.1.4. Elastic and Mechanical Properties of Doped Zirconia and Ceria

A large amount of work has been done on studying the transport properties of point defects in materials doped zirconia and ceria systems, especially above critical temperatures (usually referred as order-disorder temperature) when oxygen vacancy – dopant clusters dissociate resulting in "free" oxygen vacancies and high ionic conductivity; however less work has been done on how point defects affect mechanical properties in general, and elastic properties, in particular, especially below critical temperatures in these materials. The mechanical properties are extremely important for the structural stability, reliability and durability of the SOFC and other electrochemical devices in which SSI are crucial materials[84, 85]. Some studies on zirconia materials, for example, Kushi et al.[86] showed a large drop in elastic modulus (an "elastic anomaly") that occurs in the same temperature range, around 600 °C where the mechanical damping peaks relating to anelastic relaxation. They suggested the reason for this was a phase transformation in both YSZ and SCZ, however, Gao et al.[82] showed that there was only a phase transformation in SCZ and not in YSZ. Another study by Radovic et al.[87] showed that the fracture toughness of YSZ also showed a non-linear change with temperature, again having a minimum value around 600 °C, which is expected in the brittle materials in which fracture toughens can be related directly to the change of the elastic moduli with the temperature. The "elastic anomaly" in YSZ is shown in **Figure 1.9** where the elastic moduli, fracture toughness, and strength all show a significant drop around 600 °C before increasing again. DMA results by Gao et al.[82] show that the calculated mechanical loss coefficient (dissipated elastic energy / stored elastic energy)

at the temperature where elastic modulus show minima is comparable to polymer materials while still maintaining a relatively high elastic modulus. This can be seen in the Ashby plot in **Figure 1.10** where the position of YSZ as high temperature is marked.

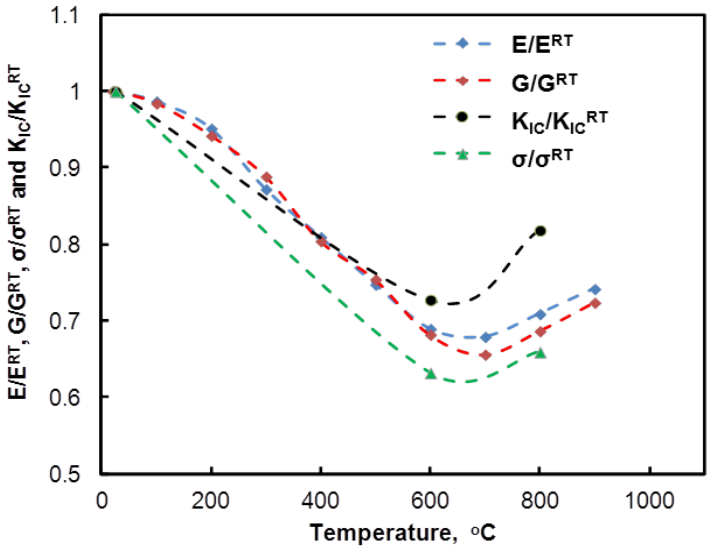

Figure 1.9. Mechanical properties of YSZ as a function of temperature, the "elastic anomaly" is clearly seen around 600 °C where there is a large drop in the mechanical properties

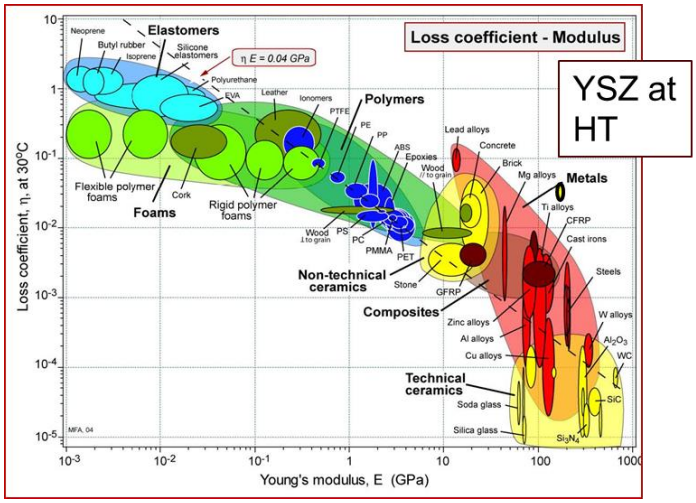

Figure 1.10. Ashby plot of Young's modulus and the loss coefficient, YSZ at high temperatures is comparable in strength to other ceramics and in mechanical loss to polymers.

1.2 Problem Statement

Due to their high operating temperature, the materials used as electrolytes in SOFC must have long term stability in reducing and oxidizing atmospheres, thermal cycling capabilities, compatibility with the anode and cathode materials and good mechanical properties[88-90]. Typical SSI are aliovalently doped cerias (CeO_2) or zirconias (ZrO_2), with gadolinia doped ceria (GDC) and yttria stabilized zirconia (YSZ) being the most popular choices[10, 49, 91].

During operation, these doped oxides are exposed to high temperatures, mechanical stresses, electric field and low oxygen partial pressures[12, 89, 90, 92]. Combined all these external factors influence the behavior and diffusion of the oxygen vacancies, and thus not only the conductivity of the SSI but also its mechanical properties[31, 75, 82, 93-

[96]. A large number of studies have focused on the transport properties of these materials and characterized how the oxygen vacancies move under these different external fields. However, less work has been done to understand the mechanical properties, especially in stabilized zirconias that exhibit a large decrease in elastic moduli at around 600 ^{o}C[82, 86, 97].

This work looks at how temperature, loading frequency and composition of doped oxides with fluorite structure influence their elastic properties and mechanical damping using Resonant Ultrasound Spectroscopy (RUS). In addition, this work is devoted to understanding how the dopant ion radius will affect the activation energy of vacancy hopping during anelastic realxation. It is believed that the activation energy will depend on the dopant ion radius similarly to how the ionic conductivity depends on the dopant ion radius. As the difference between the dopant ion radius and the critical ionic radius of the host lattice increase it is assumed the activation energy will also increase.

1.3 Research Objective

The proposed work will investigate the fundamental aspects of the elastic and anelastic behavior as a result of relaxation in doped oxides as a function of dopant size and concentration. To achieve this objective, the following must be completed:

- **Develop of High Temperature Resonant Ultrasound Spectroscopy (RUS) System** - *for carrying out mechanical spectroscopy studies at high frequencies (over 200 Hz)*

- **Fabricate of Doped Cerias and Zirconias samples** with fully stabilized fluorite structure and aliovalent (+3) dopants of different sizes
- **Measure of Elastic Moduli and Mechanical Damping** – using RUS technique in the wide range of temperatures for different samples
- **Determine Activation Energies for anelastic relaxation** from RUS measurements and compare to that determined using other low frequency mechanical spectroscopy methods.
- **Determine of Relationship between Activation Energies for Anelastic Relaxation and Dopant Size** – from the results of mechanical spectroscopy.
- **Evaluate Effects of Applied Electric Field or Reduction** on anelastic relaxation of selected SSI.
- **Determine the number of relaxation mechanisms and their most likely cause** in yttria-stabilized zirconia using RUS and DMA results

1.4 Dissertation Organization

This dissertation is organized into seven sections: Section 2 details the development of a high temperature Resonant Ultrasound Spectroscopy (RUS) setup in an environmental chamber; in Section 3 the elastic moduli and the mechanical damping of doped zirconias were studied using RUS; Section 4 further explores doped cerias using RUS and how different dopants effect the activation energy of anelastic relaxation; Section 5 explores the idea of multiple relaxation mechanisms in YSZ and how the analysis realization with multiple relaxation mechanisms observed in RUS; in Section 6

the effects of an electric field on YSZ samples were observed to discover the coupling between anelastic and dielectric relaxation; and finally Section 7 gives a summary of the major findings and offers suggestions for future work.

2. RESONANT ULTRASOUND SPECTROSCOPY FOR DETERMINING ELASTIC PROPERTIES OF SOLIDS AT HIGH TEMPERATURES

2.1 Summary

Here we report on the development of a simple and inexpensive experimental technique that can simultaneously provide more than two elastic constants for solids of lower symmetry and has the potential of being used at elevated temperatures, Resonant Ultrasound Spectroscopy (RUS). RUS is a relatively novel, highly accurate technique in determining the elastic moduli of a material from the single resonant spectra of a freely suspended solid. The goal of this project was to develop RUS for measuring moduli of solids from room temperature up to 1300 °C in controlled environments. Elastic moduli of different materials were obtained using high temperature RUS and were statistically analyzed and systematically compared to the values obtained using other high temperature techniques.

2.2 Introduction

Elastic constants are considered to be some of the most fundamental properties of any solid. They relate the stress and strain tensors in the constitutive equations for a linear elastic solid according to: $\sigma_{ij} = C_{ijkm}\ \varepsilon_{km}$, where σ_{ij} and ε_{km} are the stress and strain tensors, respectively and C_{ijkm} are 81 elastic constants[98, 99]. A symmetry and the fact that the strain energy density must be positive further reduces the number of independent elastic constants to 21, which is the maximum number of elastic constants for crystals with the lowest point group symmetry, i.e. triclinic. In the case of an

isotropic linear elastic solid (such as non-textured polycrystalline material), the number of independent elastic constants can be further reduced to only two independent constants, namely Young's modulus, E, and Shear modulus, G. The elastic constants are also of fundamental importance as they are the second derivatives of the free energy with respect to strain and are directly related to the atomic bonding of the material[100-103]. In addition, they are connected to thermal properties of solids through the harmonic vibrational theory (i.e. Debye theory)[100, 102]. Therefore, elastic constants can be used in combination with specific heat and thermal expansion measurements to determine the fundamental equation of state and various thermodynamic functions of solid materials. While the elastic constants represent primarily equilibrium thermodynamic properties, the internal friction or mechanical damping is a direct manifestation of irreversible processes related to energy absorption by various physical processes[80, 81, 104] due to anelastic processes such as thermoelastic relaxation, movement of point defects (e.g. interstitial hydrogen[105, 106]), as well as movement of linear (e.g. dislocations[107]) or planar defects (e.g. domain walls[108]).

Considering the fundamental importance of elastic properties of materials, it is not surprising that a great number of static or dynamic experimental techniques have been developed to determine them[109]. Among them, acoustic and ultrasonic methods as non-destructive techniques (NDT) that provide highly accurate characterization of a material's elastic properties has been widely used for decades, and especially valued for their ability to test a material without damaging it or altering its physical properties in any way[110, 111]. In sub-resonant ultrasonic or sonic methods, sonic or ultrasonic waves

propagate through the material, and their elastic interactions with the material affect their velocity and attenuation which in general yield information about the elastic constants and energy absorption of the material respectively[100]. Although those techniques are quite powerful, they suffer from certain limitations[99, 101, 112], chief among them are requirements for relative large samples and a number of independent measurements, often on separate samples to fully characterize the elastic properties of a material. Several acoustic methods, such as the pulse echo continuous wave method, also require that the materials are highly symmetric and can occasionally experience problems with bonding the sample to the transducers[100]. Last but not least, measurements of elastic constants become even more difficult --- if not impossible --- at extremely low and high temperatures.

On the other hand, the resonant methods rely on measuring mechanical resonance frequencies of a freely suspended solid object. Resonant Ultrasound Spectroscopy (RUS) is an inexpensive and elegant resonant experimental technique for determining the full set of material elastic constants of solid samples has gained a lot of attention over the last few decades[100, 102, 103, 113-115]. Unlike many other techniques, RUS allows simultaneous measurement of more than one elastic constant using only one sample that can be as small as 1 mm^3. In the same time, it can be used to measure ultrasonic attenuation (Q^{-1}) as a direct manifestation of irreversible energy absorption by various physical processes in the solid. Importantly, RUS provides highly reproducible and repeatable results when compared to other conventional techniques[113].

RUS is based on measuring the mechanical resonance spectrum for a sample of known geometry, dimensions and mass. It is well known that the resonant frequencies of a freely suspended solid object are special solutions of the equations of motion, which depend on density, geometry and elastic moduli and the object shape. These solutions determine all possible frequencies at which such an object would "ring" if struck. In the tripod RUS configuration, a transmitting transducer is used to generate an elastic wave of constant amplitude and varying frequency, while the other two transducers detect the sample's response, **Figure 2.1a**. Another common RUS configuration is the tip-to-tip setup, **Figure 2.1b**, where the sample is carefully clamped and held between two transducers, one transmitting and one receiving. This configuration, in addition to being difficult to setup, also applies a small load on the sample which can have an adverse effect on the results[100, 114]. The spectrum obtained from receiving transducers cannot be de-convoluted directly to deduce elastic constants. Instead, an approximate spectrum is first calculated from the known sample dimensions, density and a set of "guessed" elastic constants, which can be obtained, for example, from *ab initio* calculations[101]. A multidimensional algorithm is then used to obtain the material's elastic constants through an iterative process that minimizes root-mean-square (RMS) error between the measured and calculated resonant peaks[99, 116]. An example of a typical RUS spectra and its calculated peaks (grey +) is shown in **Figure 2.2**. Although many different shapes can be used for RUS, typically one uses a rectangular parallelepiped[117, 118], cylinder[119], or sphere[120] since these shapes decrease the amount of computation necessary to determine elastic constants. In addition to the elastic moduli, the internal friction, Q^{-1},

can be determined from the RUS spectra assuming: $Q^{-1}_k = \Delta\omega_k/\omega_{ko}$ where ω_{ko} is the frequency associated to with kth eigenmode, and $\Delta\omega_k$ is the full width at half maximum, FWHM, of that mode[102].

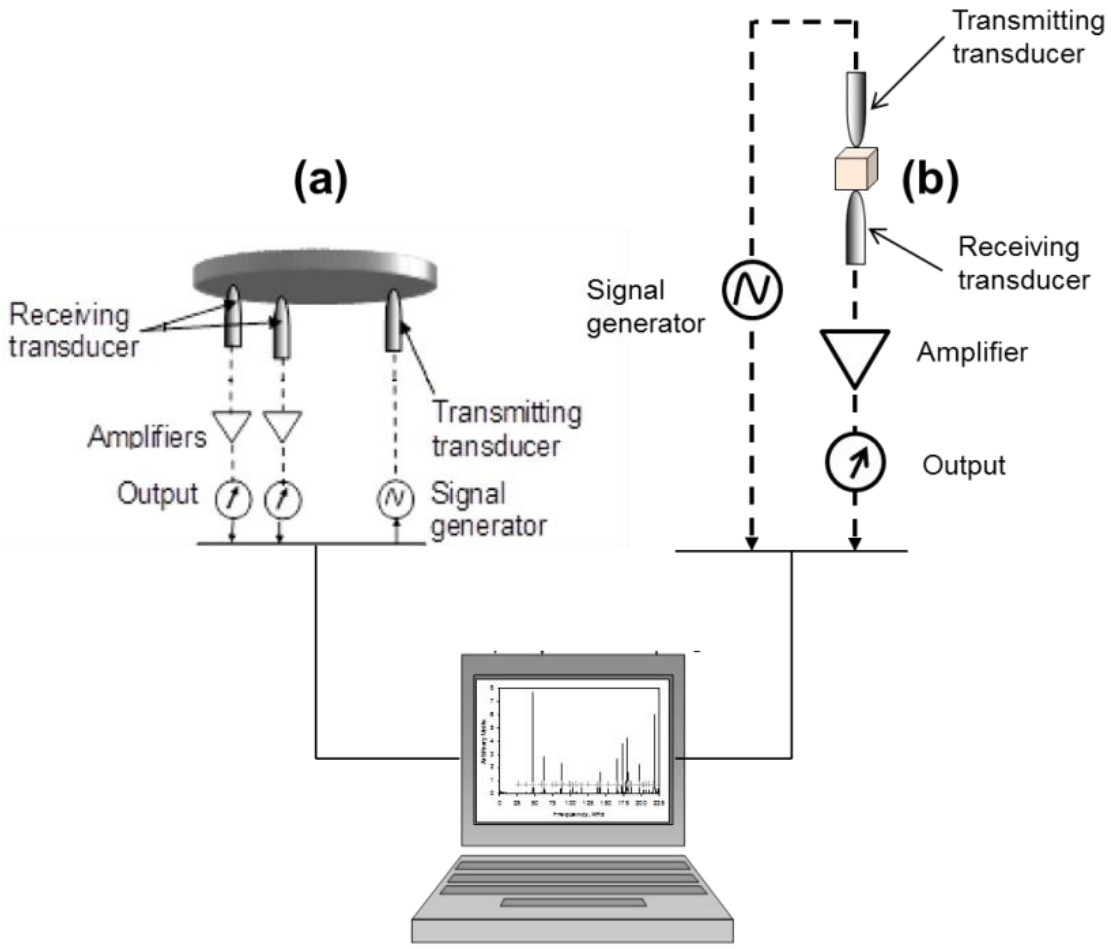

Figure 2.1. Schematic of experimental RUS (a) tripod setup and (b) tip-to-tip setup

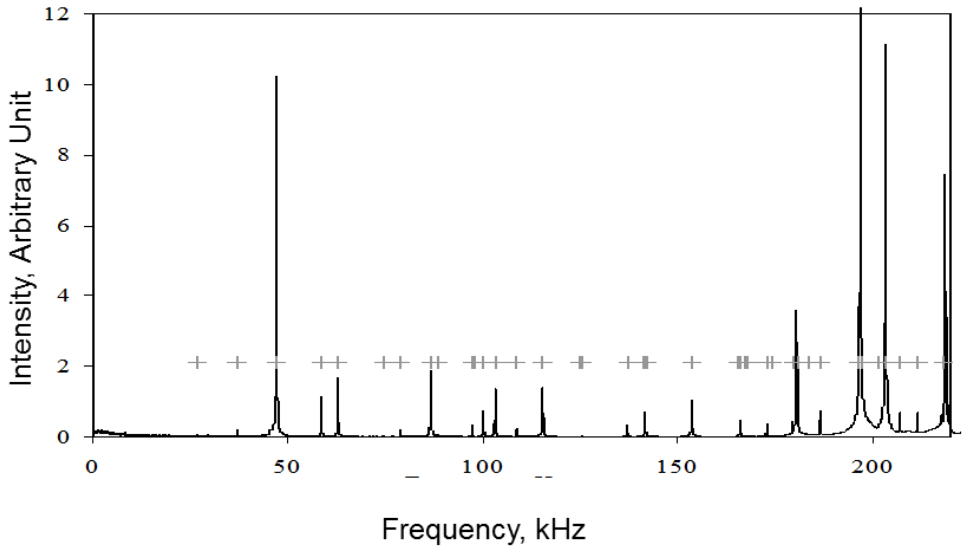

Figure 2.2. Typical RUS spectra obtained for borosilicate glass. Gray crosses indicate the peak frequencies obtained by fitting the measured spectrum.

RUS equipment, such Quasar RUSpec System (Magnaflux, Glenview, IL) used in this study, are commercially available nowadays only for the measurements at room temperature. A couple of RUS instruments have been developed for measurements at cryogenic temperatures[121-124]. However, regardless of the fact that RUS shows great potentials for measuring elastic constants of the solids at high temperatures when compared to other more conventional methods --- primarily because it requires only one small sample to obtain a full set of elastic constants --- its use has been mostly limited to temperatures below ~727 ºC[101, 125-128]. The main problem with using RUS at high temperatures is that the piezoelectric barium titanate or lead zirconate titanate transducers (both transmitting and receiving) must be kept well below their Curie temperatures[129-131], .e. below ~50ºC to obtain a good quality signal. To overcome this

problem, a long buffer rods (or extension rods) has been used in the past to transmit the ultrasonic signal between the sample located in the furnace, and the transducers located outside of it. For example, Goto and Anderson[132] developed RUS apparatus for testing small single crystal rectangular parallelepipeds up to 1500 ^{o}C, using high temperature piezoelectric transducers ($LiNbO_3$) and long buffer rods to prevent the transducers from heating up. However, their system used a tip-to-tip setup, which severely limits the capabilities of the system to the very small samples. More importantly, the forces exerted on the samples during clamping it into tip-to-tip configuration affect the measurement results. Furthermore, thermal expansion of the setup at higher temperatures can exerted additional forces on the samples. Herein, we report on development and testing of high temperature RUS (HT-RUS) setup for measurements using more robust and reliable tripod configuration to temperatures up to 1300 ºC, in the controlled environment.

2.3 Experimental Methods

2.3.1. A New Apparatus for HT- RUS

A tripod setup was selected for HT-RUS apparatus developed in this study since it allows an easy placement of the sample on transducers and measurements using larger samples when compared to edge-to-edge setup. More importantly, no stresses are exerted on the sample during measurements in the tripod set up. Commercially available RUS transducers (MagnaFlux, Glenview, IL) with the gold coated lead zirconate titanate (PZT) were used in this study. To transmit the ultrasonic signal to and from the sample

located in the furnace (**Figure 2.3**) to transducers located outside of the furnace, a 152.4 mm long single crystal sapphire (Kyocera, Kyoto, Japan) extension rods with 1 mm diameter and rounded tips where glued to the transducer using a low viscosity cyanoacrylate adhesive Loctite® 406 Instant Adhesive. Low viscosity glue allows application of very thin layer of adhesive between buffer rods and transducers, and thus good transition of the ultrasonic waves through it.

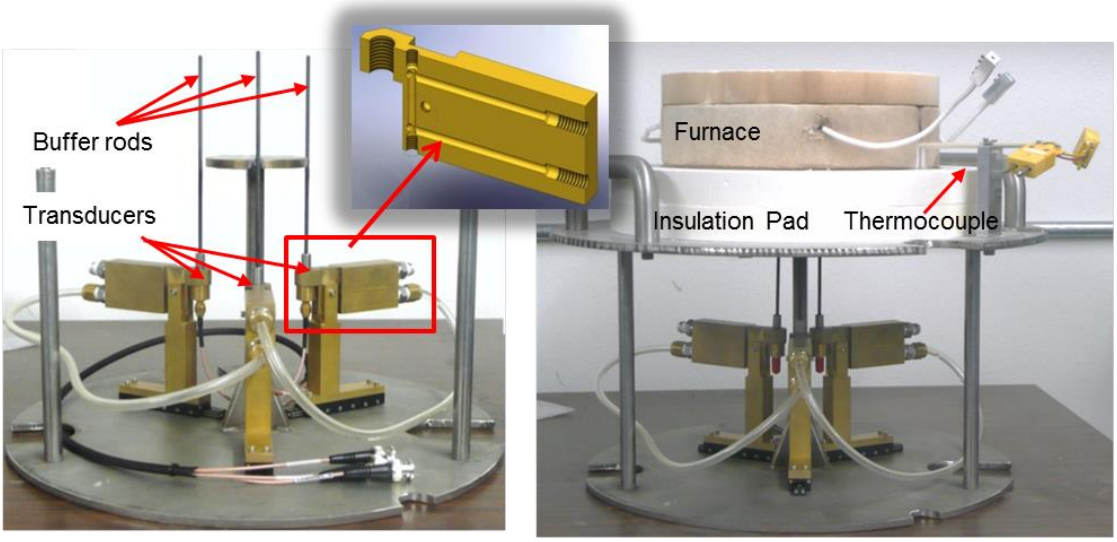

Figure 2.3. Left: HT RUS tripod setup with transducers, transducer stands, cooling jackets, and buffer rods. Right: tripod sent up with the furnace and insulation pad. The inset shows the cross section of the cooling jacket.

Application of relatively short buffer rods allows RUS measurements only to the very limited temperatures. Although sapphire (Al_2O_3) has relatively low thermal conductivity (8-15 W/m·K), a heat transfer thorough the buffer rods results in heating of

transducers to temperature exceeding 50 ºC when temperature of the sample in the furnace reaches only ~700 ºC. To further prevent overheating of the transducers, special cooling jackets for the transducers were developed. The transducer cooling jackets were machined from brass and include cooling channels, as it is shown in the inset in **Figure 2.3**. They hold transducers with buffer rods and sit on sliding holders that allow adjustment of the transducer's position to accommodate samples of the different sizes. The rods are separated by a center support rod that holds additional insulation pad to further protect the transducers, **Figure 2.3** right. A 360 W Fibercraft™ cylindrical furnace (Thermcraft, Winston Salem, NC) with a thermocouple is place on the top of insulation pad (**Figure 2.3** right) surrounding the tips of the buffer rods. A thermocouple and heater are connected to a programmable controller (TSCI Corp, Tomball, TX).

Infrared (IR) images of the setup were taken during heating the furnace in the HT-RUS set up shown in **Figure 2.3,** while running cooling water with temperature of 5 °C at 5 L/min rate through the cooling jackets. IR images of the setup during RUS measurements at 800 °C in **Figure 2.4** shows ~250 °C, while the temperature of transducers remains below 18 ºC.

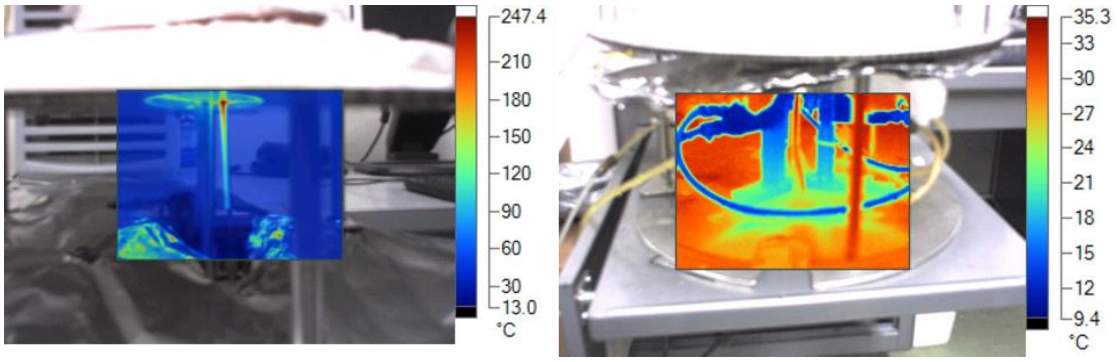

Figure 2.4. Infrared images the transducer assemblies during operation at 800 °C

The entire setup can be placed in a specially designed vacuum chamber (not shown here) for measurements in the controlled atmosphere. The latter is especially important for measuring elastic constants of the materials that oxidize in ambient air at elevated temperatures. The vacuum chamber has wall-trough electrical connectors for transducers, heater and thermocouple, as well as inlets and outlets for cooling fluid to be fed to the cooling jackets. In addition, it has connectors for a vacuum pump and an inlet that can be connected to different gas canisters to change the atmosphere within the chamber.

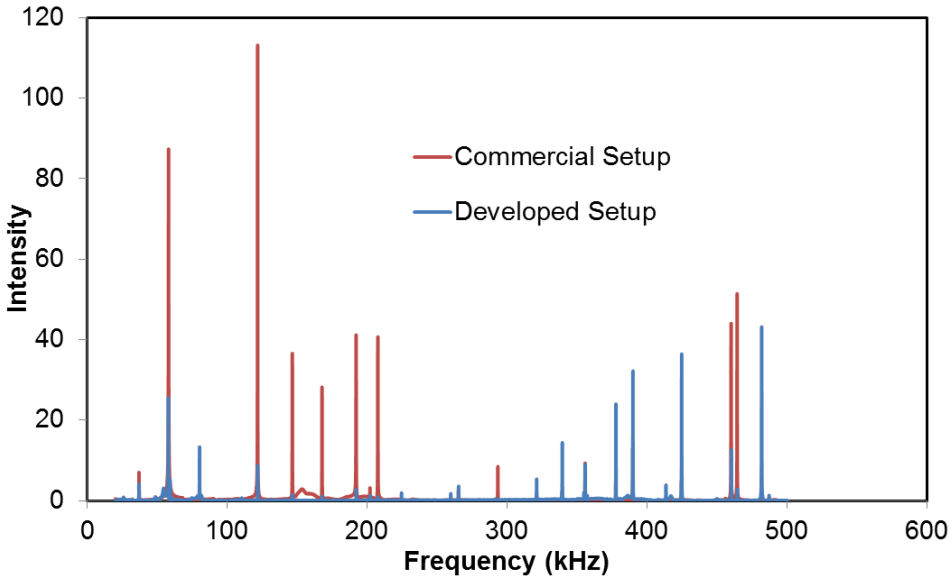

Figure 2.5. Resonant spectra of Al2O3 obtained using commercial (red) and developed (blue) tripod setups.

2.3.2. Comparison of Resonant Spectra from HT-RUS and Commercial Apparatus

The HT-RUS setup was first tested by comparing the resonant spectra obtained using the developed and commercial tripod setup (Magnaflux, Glenview, IL). Both setups were connected to the Quasar RUSpec (Magnaflux, Glenview, IL) signal processing system. Alumina discs (Zircar Ceramics Inc., NY) 20 mm in diameter and 4 mm thick were used as a standard material in this exercise. **Figure 2.5** shows resonant spectra of the same alumina sample obtained by using both tripod setups at the room temperature. In general, resonant peaks obtained using the developed setup with buffer rods (blue in **Figure 2.5**) show a lower overall intensity when compared to those obtained using commercial setup (red in **Figure 2.5**) due to some dissipation of signal occurring within the sapphire extension rods. However, more importantly the

frequencies of the resonant peaks in the 20-500 KHz range obtained using two different setup are almost the same and show differences smaller than 1 KHz between frequencies obtained in two different setups. To farther test reproducibility of the results, five frequency scans were carried out using the same alumna sample in each setup, and the standard deviations of resonant peaks frequencies were determined from all 5 measurements and plotted in **Figure 2.6**. **Figure 2.6** clearly shows a good reproducibility of the results obtained using developed HT-RUS tripod setup, because the standard deviation for resonant frequencies from multiple measurements in HT-RUS setup is comparable, and at some frequencies even lower, than that obtained using commercial tripod setup.

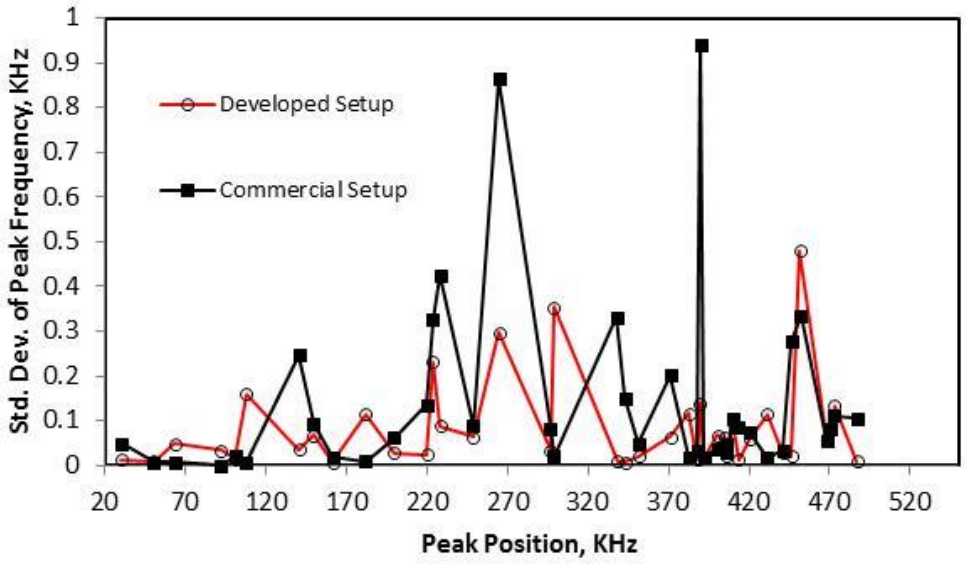

Figure 2.6. A comparison on the standard deviations of resonant peak frequency obtained from 5 measurements using developed HT-RUS (red) and commercial (black) tripod setups.

2.4 Experimental Results

The developed HT-RUS apparatus has been used to determine elastic constants (Young's and shear moduli) of different materials at high temperatures, in different testing environments. In all cases, the commercial software Quasar RuSpec (Magnaflux Quasar Systems, Albuquerque, NM) was used to calculate elastic constants from 20-40 resonant frequencies for samples with the known mass, geometry and dimensions. This software iteratively minimizes the root mean square error between analytically calculated and experimentally measured resonant frequencies of the specimen. An initial guessed values of C_{11} and C_{44} needs to be fed to this nonlinear regression fitting algorithm as the starting values. In the remainder of this section, we compare changes of elastic moduli with temperature obtained for different high-temperature materials using developed HT-RUS apparatus and other more conventional techniques or *ab initio* calculations.

2.4.1. Aluminum Oxide

Aluminum oxide (Al_2O_3) was the first material tested due to its high stiffness and linear elastic behavior. **Figure 2.7**, shows Young's and shear moduli at different temperatures obtained using developed HT-RUS (black) in comparison to the literature data. The red lines in **Figure 2.7** show RUS results published by Goto and Anderson[132, 133] while the green line represents data from Wachtman and Lam[134] obtained by impulse excitation technique. The difference in the magnitude of elastic moduli can be attributed to the different density of the samples used in different studies, since the porosity of the

samples have a large effect on elastic properties of ceramics[135, 136]. The samples tested by Goto and Anderson showed the highest values of elastic moduli, but they also had the highest density of 3.982 g/cm^3. The samples tested in this study had density of 3.888g/cm^3, and thus lower values of elastic moduli were measured in that case. Wachtman and Lam used samples with density of only 3.710 g/cm^3, and correspondingly they measured significantly lower moduli at all temperatures. Despite the differences in porosity, elastic moduli for all alumina samples change with temperature following the same trend, and they in all cases drop for 23% from room temperature to 1000 °C.

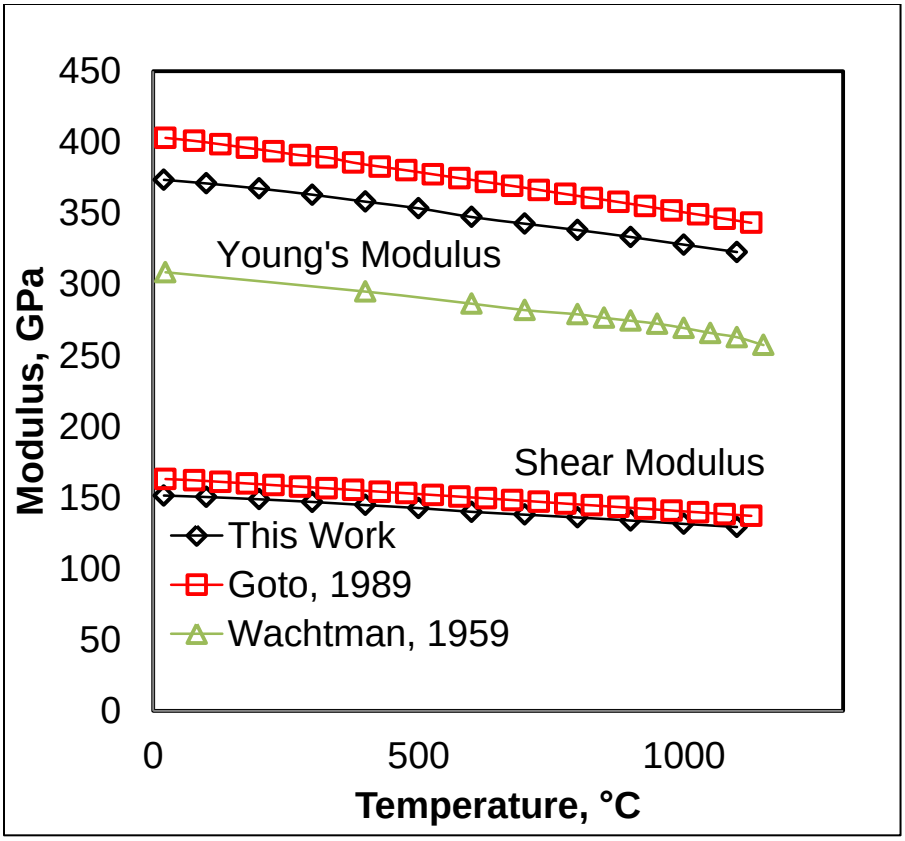

Figure 2.7. Young's modulus of Al_2O_3 samples: black –results obtained using HT-RUS in this study, red from Goto and Anderson[133] and green from Wachtman and Lam[134].

2.4.2. Doped Cerium and Zirconium Oxide

Doped oxides, such as those typically used as a solid oxide fuel cell electrolyte materials were also tested using the developed HT-RUS apparatus. The change of the elastic moduli of gadolinia doped ceria ($Ce_{0.8}Gd_{0.2}O_2$) with temperature determined using developed HT-RUS are plotted in **Figure 2.8**, together with the results obtained using molecular dynamics simulations by modeling a three-body interaction of interionic potentials[137, 138]. Note here that 20 mm dia. x 2 mm thick $Ce_{0.8}Gd_{0.2}O_2$ discs with relative

density of 98% were processed by cold isostatic pressing and subsequent pressures sintering of the commercial $Ce_{0.8}Gd_{0.2}O_2$ powders (Fuel Cell Materials, Lewis Center, OH) at 1500 ºC for 2 hours in ambient air. Here again, the magnitude of the elastic moduli obtained using HT-RUS slightly below those predicted by molecular dynamics calculations, due to lower relative density of the real samples. However, the changes of elastic moduli with temperature show the same trend in both cases.

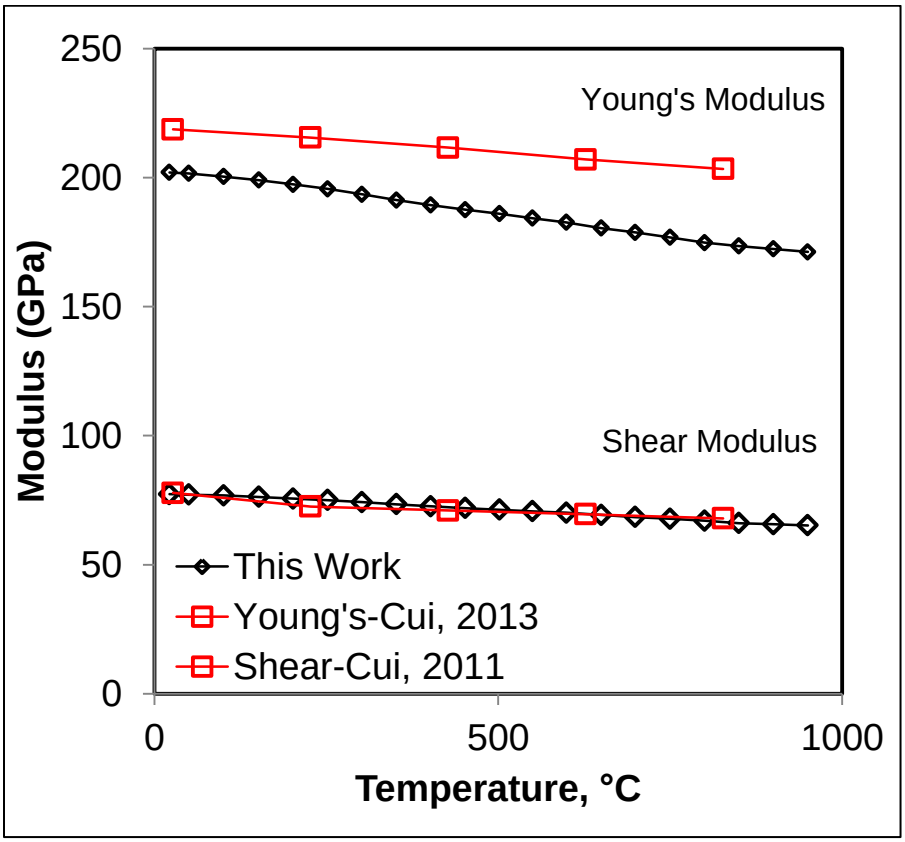

Figure 2.8. The normalized modulus for three samples of $Ce_{0.8}Gd_{0.2}O_2$, black – data obtained from our RUS setup, red – data obtained from Sun, et al.[139] by molecular dynamics simulation and green – data obtained from Cui, et al.[138] by molecular dynamics simulation.

The second doped oxide tested in this study was 8 mol% yttria-stabilized zirconia with the composition of ($Y_{0.08}Zr_{0.92}O_2$) (8YSZ). This material was chosen due to its unusual frequency dependent elastic behavior at high temperatures[82, 140], i.e. significant drop of elastic moduli in ~200-500 ºC temperature ranges due to anelastic relaxation of defect complexes. **Figure 2.9** shows elastic moduli of 8YSZ obtained using the developed HT-RUS setup (black) in comparison with data collected by Kushi et al.[86] using cantilever resonance technique and by Giraud et al.[97] using impulse excitation techniques. Results in **Figure 2.9** shows an excellent agreement between results obtained in this study and previously published data, only below ~150 ºC and above ~ 600 ºC. The discrepancy between results obtained by HT-RUS and other methods in 150-600 ºC temperature range can be attributed to the frequency dependent elastic behavior of YSZ. As it is explained in more details in the literature[140, 141], the large drop in elastic moduli of 8YSZ moves towards higher temperatures as testing frequency increases. Therefore, minimum values of elastic moduli were obtained in this study at around 600 ºC using ultrasonic frequency range (20-400 KHz), while previous results using lower sonic frequencies (< 20 KHz) shows minimum values at around 400 ºC.

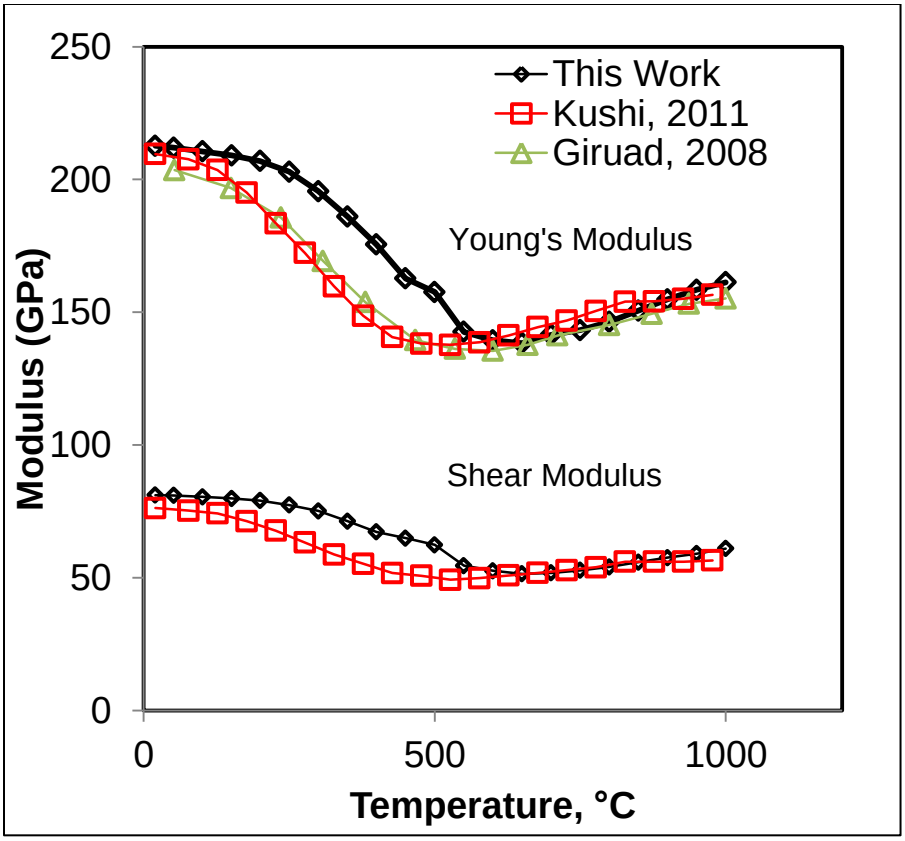

Figure 2.9. The Young's and shear modulus for 8YSZ: black – data obtained using developed HT-RUS setup, red – data obtained by Kushi, et al.[86] using cantilever resonance methods, and green – data obtained by Giraud, et al.[97] using impulse excitation method.

2.5 Conclusions

Herein we report on development of a high temperature tripod setup for resonant ultrasound spectroscopy (RUS) measurements up to 1300 °C that is capable of working in different environments. Specially designed buffer rods and transducer cooling jackets allows testing at temperatures of 1300 ºC, while keeping temperature of PZT transducers below their operational temperature limit of 50 °C. The design of the tripod

stage allows housing of the samples of specimen size and shape. The resonant spectra measured using developed tripod setup for high temperature RUS are in excellent agreement with those produced using commercial setups for room temperature measurements. In addition, Young's and shear moduli of different materials were measured at different temperatures for the variety of materials (Al_2O_3, $Ce_{0.8}Gd_{0.2}O_2$, and $Y_{0.08}Zr_{0.92}O_2$), and found to be in the good agreement with previously published experimental and/or modeling results. Newly developed tripod set up for high temperature RUS, can be used to determine a set of elastic constants in 25-1300 ºC temperature range easily and inexpensively, but with high accuracy, using only one sample of the materials.

3. STUDY OF ANELASTIC RELAXATION IN STABILIZED ZIRCONIAS BY RESONANT ULTRASOUND SPECTROSCOPY

3.1 Summary

In this study, the elastic properties of polycrystalline Yttria-stabilized Zirconia (YSZ), Scandia-Ceria-Stabilized Zirconia (SCZ) and Gadolinia Stabilized Zirconia (GSZ) were analyzed using Resonant Ultrasound Spectroscopy (RUS) in air, from room temperature up to 1000 °C, using frequencies ranging from 20 to 500 kHz. In all samples, the both Young's and shear moduli were found to decrease significantly, i.e. for up to ~50%, in the 250 °C to 600 °C. In the same temperature range, two major frequency dependent attenuation (Q^{-1}) peaks are observed that can be attributed to the anelastic relaxation of oxygen vacancy – cation complexes. Assuming single Debye relaxation model, activation energies for the anelastic relaxation where found to be in the 0.97-1.2 eV for the first relaxation peak (Peak 1) and 1.7-2.4 eV for the second one (Peak 2), depending on the type of dopant. Those results are in good agreement with previous mechanical spectroscopy studies carried out at significantly lower frequencies of up to 3 kHz. In the case of SCZ, additional relaxation peak was observed that can be attributed to the cubic to rhombohedral phase transition. Results of this study show that RUS can be used to analyze anelastic relaxation due to vacancies hopping at high frequencies.

3.2 Introduction

Fully stabilized zirconia ceramics have been widely used in solid state electrochemical devices, such as Solid oxide Fuel Cells (SOFCs), gas separation membranes, and sensors, because of their high oxygen diffusivity and ionic conductivity [9, 11]. Doping zirconia (ZrO_2) with aliovalent cations, such as Y^{3+}, Sc^{3+}, Gd^{3+}, etc, not only stabilizes its high temperature cubic (fluorite) structure down to the room temperature, but also introduced one mole of oxygen vacancies per two moles of dopant[142, 143]. The latter increases the number of charge carriers in the zirconia, and thus its conductivity at higher temperatures, usually above 600 °C, when oxygen vacancies become readily mobile[144-148]. However, the ionic conductivity of doped zirconia is found to be a strong function of the type of dopant (i.e. size of dopant) and its amount, having maximum values when the size of the dopant is close to that of Zr^{4+}[145].

Multiple studies have focused on the chemical stability, transport and electrochemical properties of stabilized zirconias[5, 9, 145, 149] at high temperatures, i.e. above ~600 °C, when oxygen ions dissociate from the dopant ions and freely migrate increasing the ionic conductivity of the material at high temperatures. However, at temperatures below 600 °C, the oxygen ions are thought to be trapped in defect complexes as it minimizes strain energy of the system and due to electrostatic forces between oppositely charged vacancy and dopant[145, 150]. Previous models place the oxygen vacancy in one of the eight first nearest neighbor positions (1NN) surrounding the dopant ion, which causes a simple oxygen vacancy-cation pair $\left(R_{Zr}^{'}V_O^{\bullet\bullet}\right)^{\bullet}$ complex to

form, where *R* is a doping cation. At higher concentrations of dopant, more complex complexes such as $\left(2R_{Zr}^{'}V_O^{\bullet\bullet}\right)$ can also form[151, 152].

Under a stress field an anelastic relaxation oxygen vacancy-cation occurs and oxygen vacancy can hop around the dopant ion to minimize lattice stress. This anelastic relaxation has been previously observed using different mechanical spectroscopy methods[76, 153]. Typically, two major relaxation peaks has been observed in mechanical spectroscopy results for doped zirconia carried out in low frequency range, i.e. from 10^{-4} Hz to 3 kHz[82, 83 83]. The first peak one was attributed to the reorientation of the simple vacancy-cation pairs, while the second one was associated with relaxation of more complex defect complexes or local ordering of oxygen vacancies[82, 151, 152]. Weller et al.[76, 83, 151, 152, 154], Lakki et al.[83], and Gao et al.[82] studied anelastic relaxation of yttria stabilized zirconia using different low frequency methods: torsional pendulum, flexural oscillations, forced vibration inverted torsional pendulum, and dynamic mechanical analysis, and found that the first relaxation peak in 20-200 °C range has an activation energy of 1.2-1.4 eV for 8YSZ and 1-1.3 eV for 10 YSZ[83, 154, 155]. The consistency of these results obtained using different methods, added to the fact that the peaks shifts are frequency dependent, suggests that the peak is due to anelastic relaxation of the elastic dipoles. However, the nature of the second major relaxation peak is still elusive. Weller first showed that the activation energy of the relaxation mechanism responsible for second relaxation peak observed in 200-450 °C temperature range changes from 2.2 eV for single crystal 8YSZ to 2.7 eV for polycrystalline 8YSZ, and proposed that this peak can be attributed to the relaxation of more complex vacancy-cation complexes. Aging

experiments by Kondoh et al.[79, 156] and Gao et al.[82] show a decrease in the intensity of in the second damping peak with an activation energy of approximately 2.7 eV after aging and concluded that complex ordering of the oxygen vacancies in zirconia stabilized with yttria affect this relaxation peak. Only a few mechanical spectroscopy studies have been carried out on Sc_2O_3-doped ZrO_2 suggesting different mechanisms for the observed internal friction peaks. Kushi et al.[86] attributed the damping peaks to phase transformations in SCZ, while Weller et al.[157] and Gao et al.[82] attribute some of the observed damping peaks to anelastic relaxation and some to phase transformations. Note here that scandia-doped zirconia has a well-documented cubic to rhombohedral, and back to cubic phase transition in 300 - 500 °C temperature range[157-159]. In addition, Gao et al.[82] showed large drops in Young's modulus with temperature correspond to observed maxima in internal friction, and also that Young's modulus is frequency dependent at the temperatures where high internal friction was observed.

All of the previous experiments were done at relatively low frequencies, below 3 kHz[82, 83, 154, 155]. Recent studies have started using resonant ultrasound spectroscopy (RUS) which can be useful tool to study anelastic relaxations at very high frequencies, i.e. above 20 kHz. RUS is a relatively novel, highly accurate, dynamic technique for characterizing the full set of elastic constants using only one small sample[101, 103, 112, 115, 116, 160]. Unlike many other techniques, RUS allows simultaneous measurement of more than one elastic constant as well as the determination of ultrasonic attenuation (Q^{-1}) as a direct manifestation of irreversible energy absorption by various physical processes in the solid such as defect motion [100] and phase transitions [161]. RUS is a very sensitive

technique to the study of defect motion in the high frequency range due to low levels of dissipation at the resonant modes[100, 111]. This sensitivity can be exploited for a variety of different studies, including monitoring hydrogen versus deuterium motion where hydrogen was seen to move faster through crystals[105, 162, 163]. Zhang, et al. used RUS to study the relaxation mechanisms related to minute changes is elastic strain in $LaCoO_3$ and $SrZr_{1-x}Ti_xO_3$[128, 164]. In the case of $LaCoO_3$, the changes in elastic strain were related to anelastic relaxation of twin boundaries in the system and changes in the spin state. In $SrZr_{1-x}Ti_xO_3$, phase transitions coincide with an increase in mechanical loss, Q^{-1}, with the maximum occurring at the transition point.

In this study RUS is used to observe the changes in elastic moduli and internal friction (Q^{-1}) of 8 mol% and 10 mol% Yttria stabilized Zirconia (8YSZ and 10 YSZ, respectively), 10 mol% Scandia and 1 mol% Ceria stabilized zirconia (SCZ), and 10 mol% Gadolinia Stabilized Zirconia (GSZ) from room temperature to 1000 °C, in the ambient air. The tripod RUS setup used in this study provides a stress free boundary condition which eliminates all potential stress effects on the results[165]. The changes in Q^{-1} with temperature and frequency ranging from 20 to 500 kHz, are used to characterize anelastic relaxation in stabilized zirconias, and determine activation energies for those relaxation processes.

3.3 Materials and Methods

All samples in this study were processed from commercially available powers: (a) 8YSZ ($Y_{0.08}Zr_{0.92}O_{1.96}$) samples from 8 mol% Yttria stabilized Zirconia powder

(TOSOH Corp., Japan); (b) 10YSZ ($Y_{0.10}Zr_{0.90}O_{1.95}$) samples from 10 mol% Yttria stabilized Zirconia powder (TOSOH Corp., Japan); (c) GSZ ($Gc_{0.10}Zr_{0.90}O_{1.95}$) samples from the mixture of Gd_2O_3 (Alfa Aesar , USA) and ZrO_2 (Alfa Aesar , USA) powders; and (d) SCZ ($Sc_{0.10}Ce_{0.01}Zr_{0.89}O_{1.95}$) from 10 mol% Scandia, 1 mol% Ceria stabilized 89 mol% Zirconia powders (Daiichi Kigenso Kagaku Kogyo Co. Ltd., Japan). Samples were uniaxially cold pressed at 20 MPa for 10 seconds into 25 x 8 mm^3 cylindrical green samples. The green samples were then sintered at 1500 °C for 2 hours in air using heating and cooling rates of 5 °C/min. Samples were then cut into 14 x 11 x 2 mm rectangular parallelepiped for Reasoned Ultrasound Spectroscopy (RUS). The relative density of each sample was measured to be above 98% using the Archimedes principle according to the modified standard procedure C20-00[166], described in more detail elsewhere [167, 168].

Each sample was initially tested at room temperature using the commercially available Quasar RUS system (Magnaflux, Glenview, IL) with PZT transducers to ensure that each sample is defect free and provide a good RUS signal. Samples were then placed on a custom built high temperature tripod stage for testing[165] in ambient air, from room temperature up to 1000 °C. The high temperature setup uses three 6 inch single crystal alumina rods glued to PZT transducers: one of them transmits ultrasonic waves at sweeping frequency and constant amplitude to the sample, and two of them monitor the signal from the sample. Each sample was tested from 20 kHz to 500 kHz according to the following temperature pattern: every 50 °C up to 200 °C, then every 20 °C up to 700 °C, and finally every 50 °C up to 1000 °C. RUSpec Software (Magnaflux,

Glenview, IL) was used to determine elastic constants at each temperature from the collected resonant spectra using procedure describe in more details elsewhere[111, 113, 169] . Since all samples examined in this study had polycrystalline structure with random orientation of the grains (no texture), they were treated as isotropic elastic solids, and only two elastic constants, namely Young's (E) and shear (G) moduli were calculated. The attenuation or mechanical damping was determined by measuring the full width at half maximum (FWHM) of selected peaks at every temperature, as described elsewhere[104, 170], using Fityk software[171] with Pearson 7 peaks models.

The mechanical damping during anelastic relaxation represents the dissipated energy caused by the movement of defects during mechanical excitation[80 104, 163, 172]. The activation energy for the defect motion can be calculated using a single Debye relaxation model as

$$f = f_0 \exp\left(\frac{-H_r}{kT}\right) \quad \textbf{(3.1)}$$

where H_r is the activation energy for the relaxation process[81], k is Boltzmann constant, T is the temperature in Kelvin and f_0 is attempt frequency. The attenuation peaks of several frequencies need to be measured as a function of temperature to calculate the activation energy, and it can be calculated as a slop of an Arrhenius plot (lnf vs 1/T).

3.4 Results and Discussion

3.4.1. Resonant Ultrasound Spectroscopy of YSZ

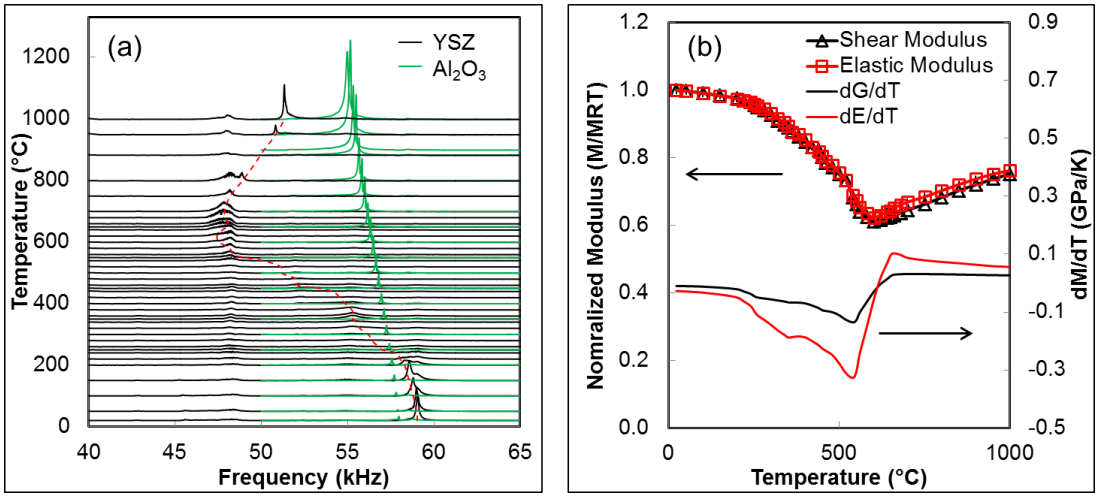

Figure 3.1. (a) Resonant spectra of in 40-65 kHz range for 8YSZ and alumina (Al_2O_3) at different of temperatures. Position of resonate peak for 8YSZ shows a large shift to the indicating significant drop in the elastic moduli. (b) Shear and Young's Modulus of 8YSZ and their derivatives with respect to temperature determined using Resonant Ultrasound Spectroscopy. Both moduli show a decrease of about 40% at 600 °C.

When compared to other typical oxides, such as alumina (Al_2O_3), resonant spectra of 8YSZ obtained using RUS show some unique features. As it is illustrated on the example of the resonant peak at around 57 Hz in **Figure 3.1a**, resonant peaks shift significantly towards lower frequencies with temperature increasing from 200 °C to 600 °C, and after that they again move towards higher frequencies with increasing temperature. Note, that resonant peak for alumina in **Figure 3.1a** monotonically shifts

towards lower frequencies with increasing temperature. As a results of such a pronounced change in position of resonant peaks for 8YSZ in 200-600 °C temperature range, significant drop in both Young's and shear moduli can be observed in that temperature range, **Figure 3.1b**. First derivatives of the elastic moduli with respect to temperature (dE/dT and dE/dG) suggest that actually the first initial drop in the elastic modulus occurs from about 200 °C to 400 °C, followed by the then second larger drop from 400 °C to 600 °C, after which the elastic modulus starts to increase slightly again. Note here that Young's and shear moduli of 220 GPa and 80 GPa, measured by RUS in this study at room temperature are in good agreement with previously published results for 8YSZ[87, 159, 173]. However, previous results obtained using dynamic methods at lower frequencies, show that significant drop in elastic moduli occurs at much lower temperature than reported here. For example, Gao et al.[82] showed that elastic modulus determined using DMA in 0.01 – 100 Hz frequency range, had minimum value at around 400 °C, and that it moved towards higher temperatures with increasing frequencies. Thus, it is not surprising that minimum modulus was observed in this study at around 600 °C because RUS tests were carried out at significantly higher frequencies.

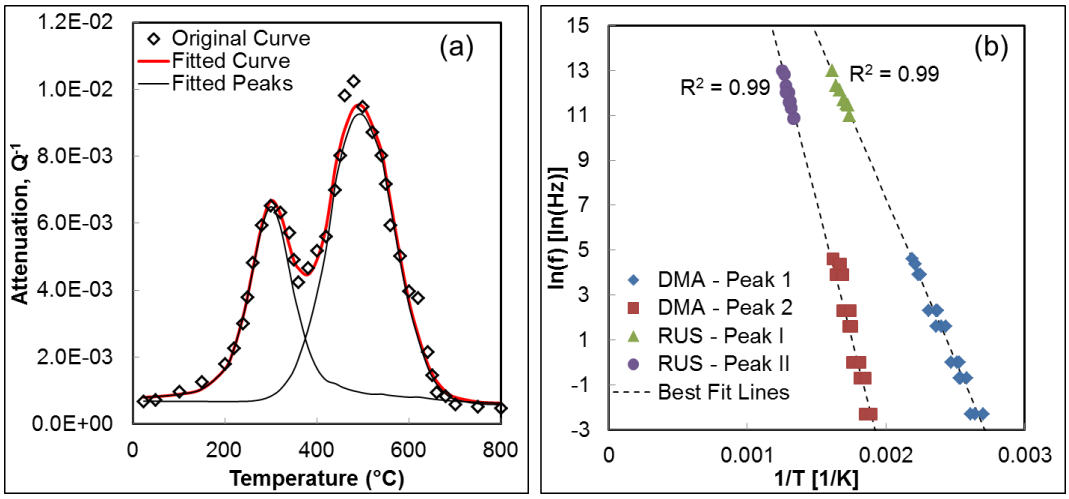

Figure 3.2. (a) The attenuation of 100 kHz resonant peak as a function of temperature for 8YSZ has two obvious major peaks similar to those reported using other techniques[82 83, 154]. (b) Arrhenius plot (ln*f* vs. 1/T) obtained from RUS and DMA[82] studies of 8YSZ. Dashed lines are the best fitting lines for both set of data.

Figure 3.1a also shows that resonant peaks of 8YSZ become significantly smaller and broader in 200-600 °C temperature range, suggesting very high attenuation. Following the method described earlier, attenuations for six resonant peaks at each temperature was determined from the full with at the half maxima of each resonant peak. **Figure 3.2a** shows selected but typical Q^{-1} vs. temperature plot (relaxation spectrum) for the resonant peak at around 100 kHz. As in the previous studies that used sub-resonance mechanical spectroscopy methods[82, 83, 154], a two major relaxation peaks can be observed for 8YSZ. Therefore, relaxation spectra at each temperature where deconvoluted using XPSPEAK4.1 (The Chinese University of Hong Kong, Hong Kong) assuming two major relaxation peaks (black lines in **Figure 3.2a**), that are further denoted as Peak I and Peak II. **Figure 3.2b** shows Arrhenius plot of ln*f*, where *f* is a frequency of the resonant peak,

vs. 1/T, where T is temperature of the maximum attenuation determined from deconvoluted relaxation spectra for each frequency, such that in **Figure 3.2a**. For comparison, data obtained by Gao et al. [82] using DMA at much lower frequencies are also shown on the same Arrhenius plot (**Figure 3.2b**). **Figure 3.2** shows that the first major mechanical damping peak (Peak I) appears in the 200-400 °C temperature range, the same range as the first drop in elastic moduli shown in **Figure 3.1b**. Similarly, the second major peak (Peak II) lies in the 400- 700 °C temperature range, in which the second drop in elastic modulus can be observed in **Figure 3.1b**. Note here that results in **Figure 3.2b** clearly show that both relaxation peaks I and II appear at much higher temperatures in RUS results, when compared to DMA results. However, is can be seen in the same plot, both RUS and DMA results follow the same trend suggesting that the same relaxation mechanisms are operative in both testing conditions having the same activation energies and relaxation times.

Results in **Figure 3.2b** can be further used to determine activation energies of the relaxation mechanism responsible for the Peaks I and II from the slopes of ln$f$ vs. 1/T lines, assuming that each of them can be model using single Debye relaxation model described earlier (**Eq. 3.1**). The values for the activation energies determined for Peak I and II in this study are shown in **Table 3.1** together with the data from the previous DMA[82], together with R^2 values for linear fitting of the results in **Figure 3.2b**. First, **Table 3.1** shows that the values for the activation energies obtained from the RUS and DMA results are in good agreement. Second, when two sets of data were combined and fitted assuming liner relationship (dashed lines in **Figure 3.2b**) for relaxation peaks I and

II over the entire frequency range of 10 orders of magnitude, high values of R^2 are obtained (**Figure 3.2b**). This suggest that the same relaxation mechanisms are responsible for appearance of both relaxation peaks within the frequency range of 10 orders of magnitude, i.e. that relaxation of the vacancy-cation clusters is responsible for relaxation peak I while relaxation of more complex defect clusters or vacancy ordering is responsible for relaxation peak II, as it is proposed based on the results of subresonant mechanical spectroscopy[82, 83, 152, 154].

Table 3.1. Activation energies for relaxation peaks I and II determined from RUS and DMA results[82].

	Peak I		Peak II	
	Activation Energy (eV)	R^2	Activation Energy (eV)	R^2
DMA	1.25 ± 0.074	0.98	2.57 ± 0.011	0.96
RUS	1.21 ± 0.008	0.96	2.18 ± 0.011	0.95

RUS results obtained using 10YSZ shows qualitatively similar results as in the case of 8YSZ, i.e. shear and Young's moduli of 10 YSZ and their derivatives with temperature show an initial decrease to approximately 80% of the room temperature values in the 200-400 °C temperature range **Figure 3.3(a)**. However, the second drop in elastic moduli in the 400-700 °C range is significantly smaller in 10YSZ when compared to 8YSZ. This is in good agreement with previous results[82, 154] that showed smaller values of Q^{-1} for 10YSZ than those for 8YSZ in this temperature range. The later can be explained by the fact that larger number of oxygen vacancies in 10YSZ tends to cluster

in more complex complexes, while the smaller number of them can relax by oxygen vacancy hopping, leading to the smaller decrease in the real part of the elastic modulus. Relaxation spectra of 10YSZ (**Figure 3.3b**) were also deconvoluted into two major relaxation peaks as in the case of 8YSZ, and Arrhenius plots for both major peaks I and II are plotted in **Figure 3.3c**. Activation energies for relaxation peaks I and II were determined from Arrhenius plots in **Figure 3.3c**, and listed in **Table 3.2** together with those obtained in the previous DMA study[82]. Once again, **Figure 3.3c** and **Table 3.1** shows that results obtained using two different techniques in the wide frequency range are in the good agreement. More importantly, results in **Table 3.2** show that activation energies of 1.18 eV and 2.2 eV for relaxation peaks I and II, respectively, observed in 10YSZ are very close to those determined for 8YSZ.

Table 3.2. Activation energies for relaxation peaks I and II observed in 10YSZ using RUS together with data preciously obtained using DMA[82].

	Peak I		Peak II	
	Activation Energy (eV)	R^2	Activation Energy (eV)	R^2
DMA	1.44 ± 0.049	0.99	2.61 ± .113	0.97
RUS	1.18 ± 0.005	0.94	2.20 ± 0.042	0.95

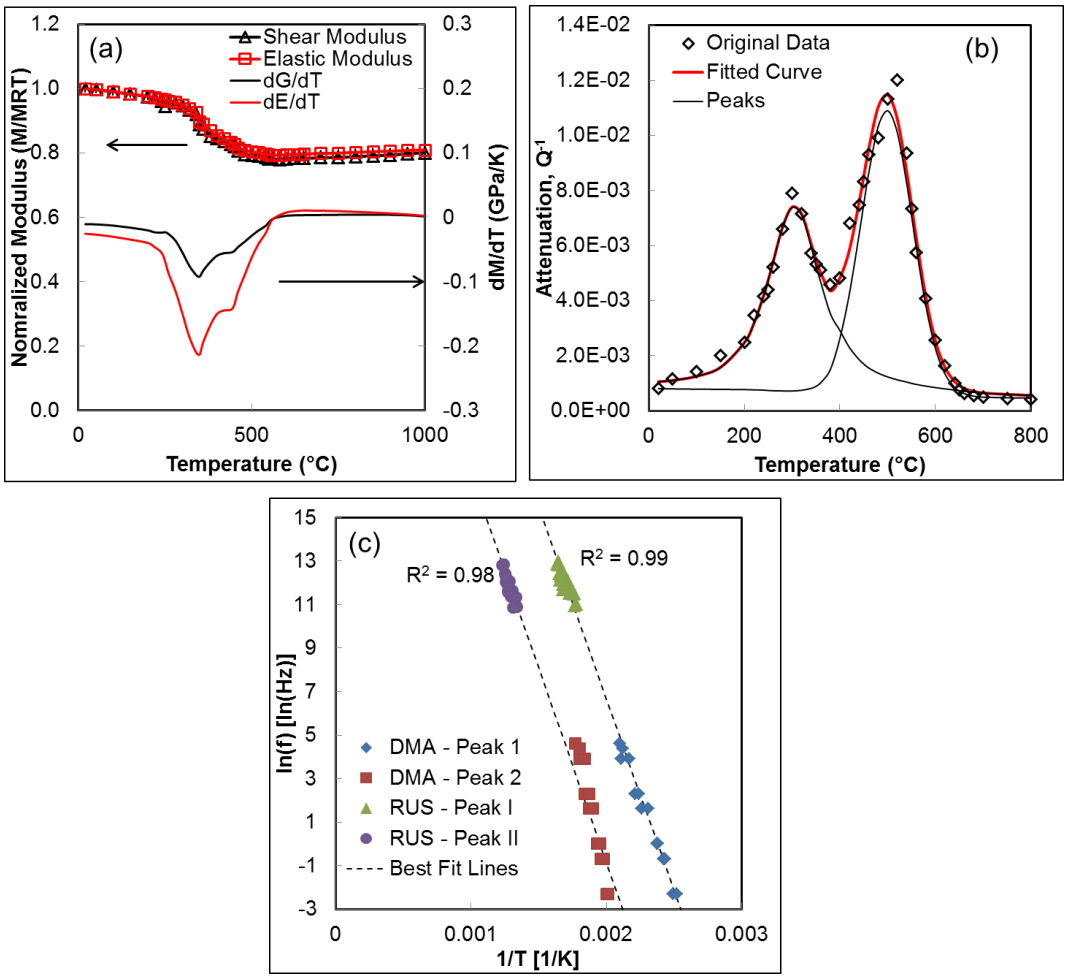

Figure 3.3. (a) Young's and shear Moduli and their derivatives with respect to temperature for 10YSZ determined using Resonant Ultrasound Spectroscopy at various temperatures. (b) Attenuation of 100 kHz resonant peak as a function of temperature for 10YSZ. (c) Arrhenius plot of 10YSZ data for both attenuation peaks determined by RUS and DMA[82] with best fit lines through the two damping peaks.

3.4.2. Resonant Ultrasound Spectroscopy of GSZ

The elastic moduli of GSZ are plotted in **Figure 3.4a**, which show a large drop at around 400 °C and a slightly smaller drop at 600 °C before the moduli values levels off at about 80% of the room temperature value. The mechanical damping again shows two

major relaxation peaks as it is illustrated in **Figure 3.4b** for the 100 kHz resonance peak. Similar to YSZ, the first peak is likely due to anelastic relaxation of the vacancy-dopant dipole $\left(R_{Zr}^{'}V_{O}^{\bullet\bullet}\right)^{\bullet}$ and the second peak is likely due to anelastic relaxation of more complex vacancy-dopant dipoles or local ordering of the oxygen vacancies. The activation energies for the two peaks were calculated to be 1.04 eV and 2.39 eV, similar to the values calculated for YSZ.

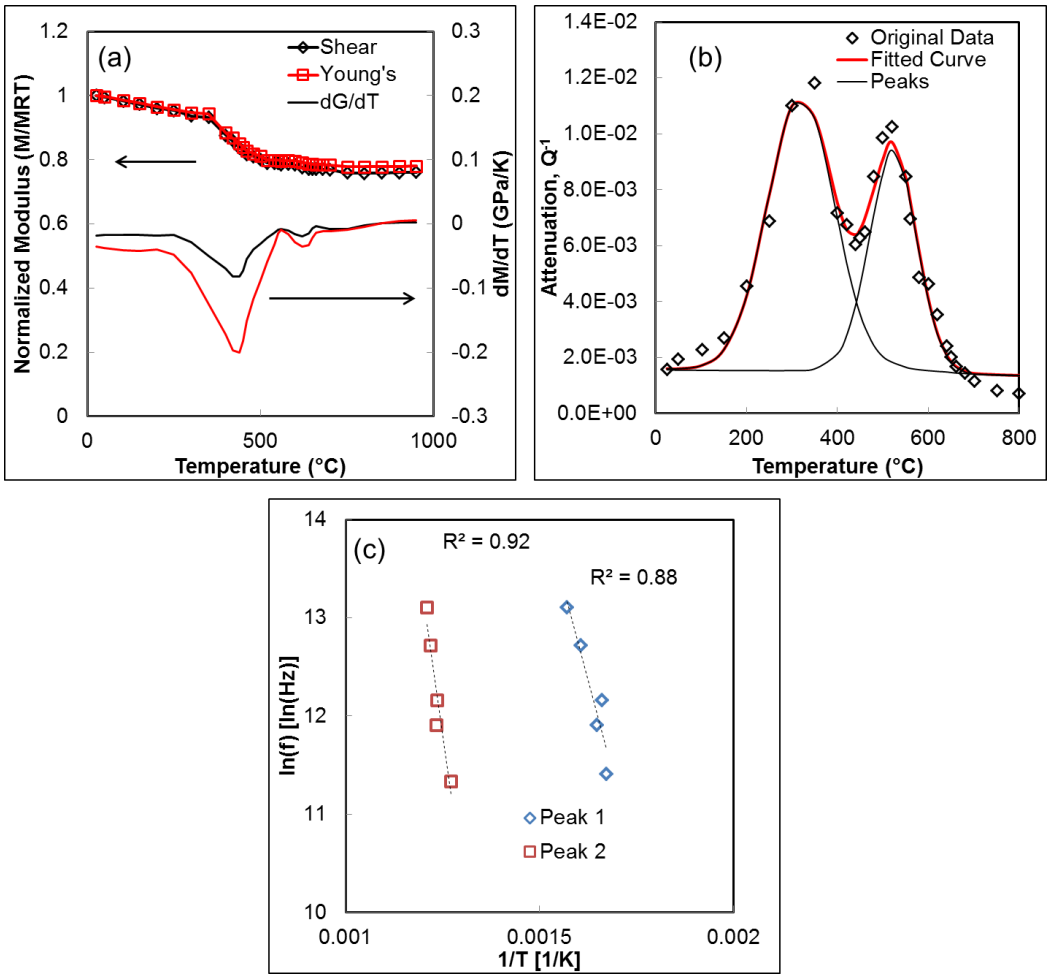

Figure 3.4. (a) Young's and shear moduli and their derivatives with respect to temperature for GSZ calculated using Resonant Ultrasound Spectroscopy. (b) Attenuation of 100 kHz resonant peak as a function of temperature for GSZ. (c) Arrhenius plot of 10YSZ data for both attenuation peaks determined by RUS with best fit lines through the two damping peaks.

Table 3.3. Activation energies for relaxation peaks I and II observed in GSZ using RUS

Peak 1		Peak 2	
Activation Energy (eV)	R^2	Activation Energy (eV)	R^2
1.04	0.85	2.39	0.92

3.4.3. Mechanical Damping of SCZ

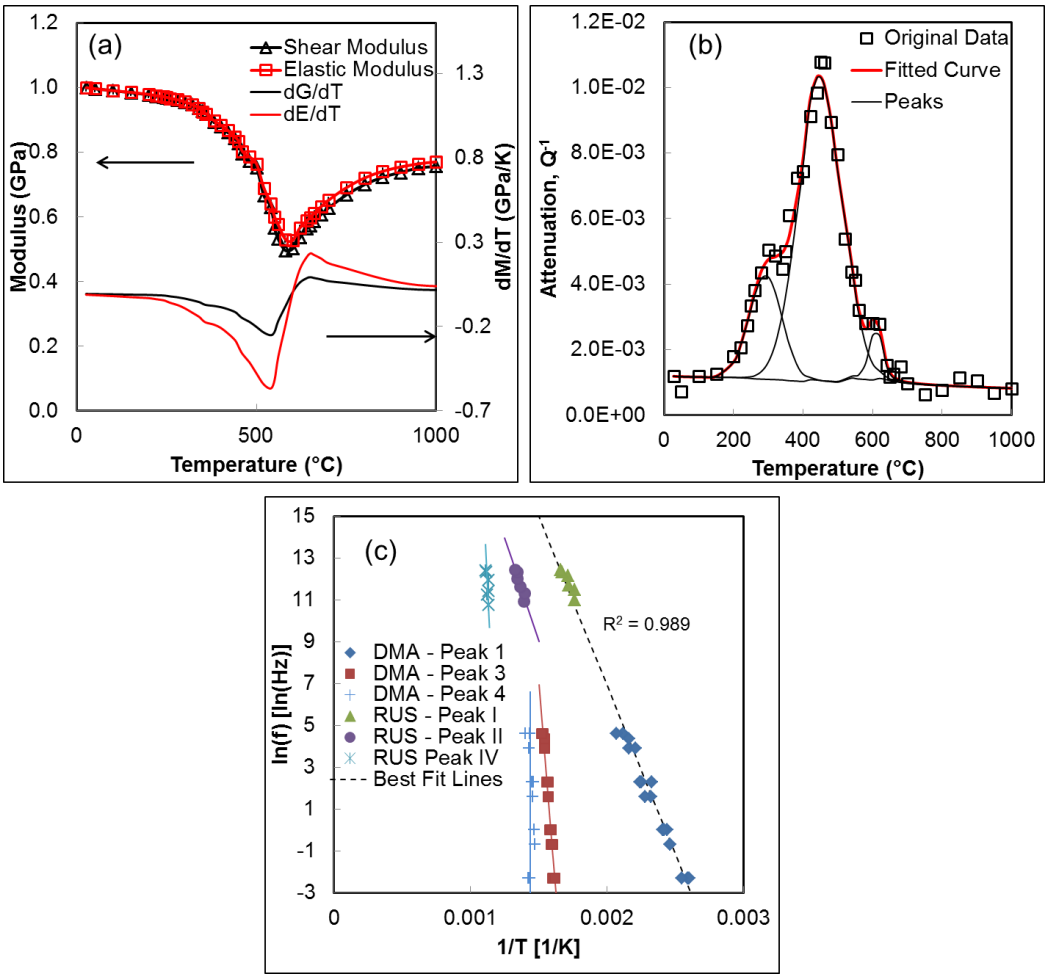

Figure 3.5. (a) Young's and shear Moduli and the derivative with respect to temperature for SCZ calculated using Resonant Ultrasound Spectroscopy. (b) Attenuation of 60 kHz resonant peak as a function of temperature for 8YSZ. (c) Arrhenius plots for SCZ comparing RUS and DMA data82. The first peak for both RUS and DMA (Peaks 1 and I) clearly show a similar trend indicating a similar mechanism. Arrhenius plots for the rest of the peaks determined from RUS and DMA results do not show the similar trends.

Table 3.4. Activation energies for different relaxation peaks observed in SCZ using RUS and DMA[82].

	Peak I		Peak II		Peak 3	
	Activation Energy (eV)	R^2	Activation Energy (eV)	R^2	Activation Energy (eV)	R^2
DMA	1.24 ± 0.04	0.975			6.76 ± 0.725	0.965
RUS	1.02 ± 0.079	0.848	1.51 ± 0.264	0.887		

The change of elastic moduli and the moduli derivatives as a function of temperature are plotted in **Figure 3.5a** as a function of temperature for SCZ. As in the case of YSZ and GSZ, both E and G of SCZ also show significant drop to ~50% of their room temperature values at around 600 °C. Before that, a smaller drop can be also observed at around 300 °C from dE/dT and dG/dT vs. T plots in **Figure 3.5a**. **Figure 3.5b** shows the attenuation or mechanical damping curve of SCZ that was obtained from the FWHM of the second resonant peak at 60 kHz at room temperature. In this case, relaxation spectra have to be deconvoluted assuming three mechanical relaxation peaks, because besides Peaks I and II, another smaller peak denoted as Peak IV can be observed on the right shoulder of the Peak II. Note here that three relaxation peaks, labeled as Peak 1, 3, and 4 were also observed in relaxation spectra of SCZ obtained using DMA in previous study[82].

Arrhenius plots (ln*f* vs. 1/T) for relaxation Peaks I, II and IV deconvoluted from RUS relaxation spectra (such that illustrated in **Figure 3.5b**) are plotted in **Figure 3.5c**, together with previous results from the DMA study[82]. Assuming single Debye relaxation mechanism for each deconvoluted relaxation peak, activation energies were calculated

from Arrhenius plots in **Figure 3.5c** and their values are provided in **Table 3.4.** Activation energies for Peak I in **Table 3.4** obtained in this study are, but little bit lower than those in obtained by DMA, as in the case of 8YSZ and 10YSZ. However, when Arrhenius plots for Peaks I and 1 observed in RUS and DMA results, respectively, are fitted together a straight line (dashed line in **Figure 3.5b**), they provide a good fitting with R^2=0.989, suggesting the a the same relaxation mechanisms is responsible for the observed relaxation peak in the entire frequency range. More importantly, activation energies of Peak 1 and I obtained using DMA and RUS, respectively, are lower for SCZ than for those 8YSZ and 10YSZ. The later can be attributed to the smaller ionic radius of eight-fold coordinated Sc^{3+} (87 pm) ion when compared to Y^{3+} (101.9 pm) dopant, as it is disused in more details elsewhere. All this suggest that this peak can be attributed to the anelastic relaxation of the dopant-vacancy dipole $\left(R_{Zr}^{'}V_O^{\bullet\bullet}\right)^{\bullet}$, as suggested earlier[82, 83, 154].

Ln*f* vs. 1/T plots for the remaining RUS peaks do not clearly align with any of the DMA peaks, **Figure 3.5c**. As it is discussed in previous study[82], activation energy of Peak 2 could not be determined accurately from deconvoluted relaxations spectra obtained by DMA, because that relaxation peak was covered by the much larger Peak 3 of caused by stress induced cubic to rhombohedral phase transformation in 300-400 °C temperature range. The fact that the activation energy of 1.7 eV for Peak II determined from RUS results is much smaller than that of 6.5-8 eV for Peak 3 calculated from DMA (**Table 3.4**), but close to that determined in 8YSZ, 10YSZ and GSC for Peak II, suggest that that relaxation peak is not caused by stress induced phase transformation, but rather

by relaxation of more complex defect clusters or local ordering of the oxygen vacancies. The Peak 3 observed in DMA and associated with stress induced cubic to rhombohedral transformation is missing from the RUS relaxations spectra. The most likely reason for this is that phase transformation cannot occur in RUS conditions because significantly lower strains and stresses are imposed on the sample in RUS when compared to DMA. Even if this phase transformation occurs in RUS condition, the volume of the transformed phase most likely very small, and thus Peak III in relaxation spectra is weak and covered by much stronger Peak II. For example, studies by Zhang et al.[128, 164] also observed that applied stress can change the behavior of the mechanical damping peaks in $LaCoO_3$ and $SrZr_{1-x}Ti_xO_3$ resulting in different trends.

The Peak IV observed in RUS relaxation spectra results could be due to rhombohedral to cubic phase transformation and thus it can correspond to the Peak 4 observed in DMA. Results of fitting Ln*f* vs. 1/T data independently for both Peak IV and Peak 4 from RUS and DMA, using straight lines (**Figure 3.5c**) suggest that both peaks are frequency independent. This is in good agreement with previous founding that Peak 4 is caused by frequency independent rhombohedral to cubic phase transformation[82, 157]. However, while Peak 4 shows up at ~450 in DMA results °C[82, 157], it appears at much higher temperature ~600 °C in relaxation spectra obtained from RUS. Therefore, the nature of that relaxation peak remains still elusive, and more work is needed to understand the underlying mechanisms behind that relaxation peak.

3.4.4. Effect of the Dopant Size on the Activation Energy for Relaxation Peaks I and II

Figure 3.6 shows the relationship between the activation energies and the difference between the dopant ionic radius and the ionic radius of Zr^{4+} (0.084 nm). The activation energies from the DMA results[82], are consistently slightly larger than the values calculated the RUS results likely due to the larger strains on the sample. More importantly, as the difference in ionic radii increases, the activation energy also increases, shown by the dashed lines in **Figure 3.6.** Studies[44, 46] have shown that reducing the difference between the ionic radii of the dopant and host ion decreases the lattice strain and increases the ionic conductivity in the materials. This same trend can be applied here, where the close the dopant ion radius is to Zr^{4+} the lower the activation energy and the easier for oxygen ions to hop around dopant.

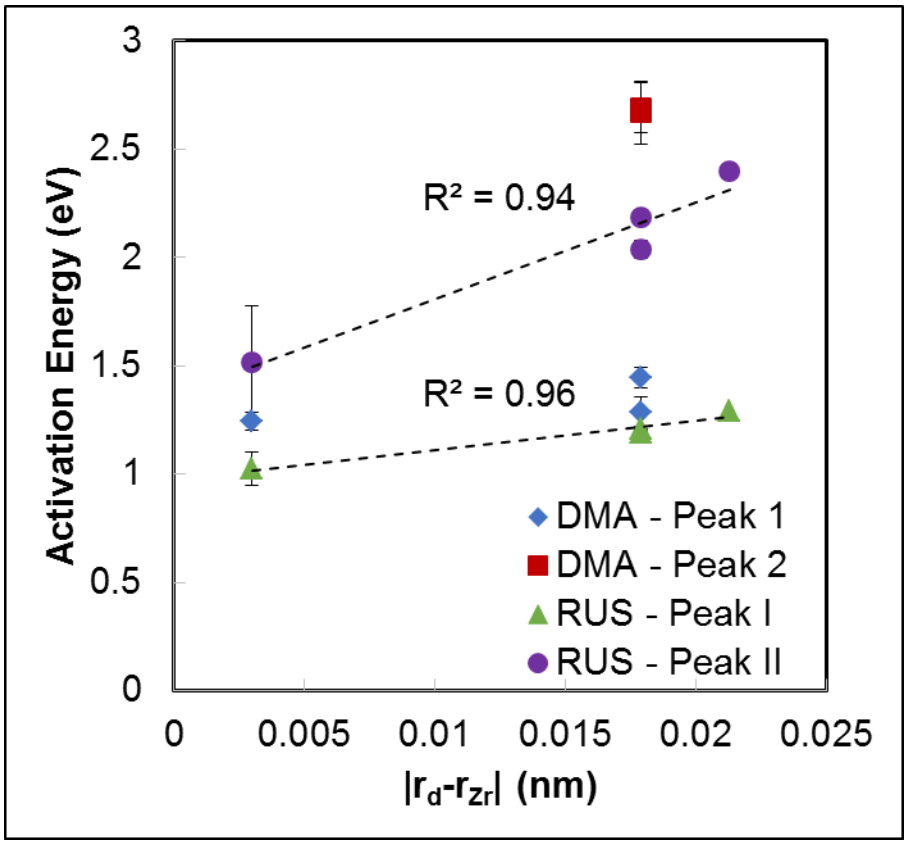

Figure 3.6. The activation energy values for each sample are plotted vs. the difference between the dopant radius and the radius of Zr4+.

3.5 Conclusion

Resonant Ultrasound Spectroscopy (RUS) study of 8mol% and 10mol% Yttria-stabilized Zirconia (8YSZ and 10YSZ), 10mol% Scandia – 1mol% Ceria stabilized Zirconia (SCZ), and 10 mol% Gadalinina stabilized Zirconia (GSZ) from room temperature up to 1000 °C, in 20-500 kHz frequency range are presented in this study. The large decrease in Young's and shear modulus corresponds to an increase in

mechanical damping that can be explained by anelastic relaxation mechanisms and local order of oxygen vacancies.

The mechanical damping peaks in both YSZ samples were deconvoluted into two frequency dependent peaks. The activation energies for the first mechanical damping peak were calculated to be 1.20 eV and 1.19 eV for 8YSZ and 10YSZ respectively. The second damping peak occurs at higher temperatures with activation energies of 2.18 eV and 2.04 eV for 8YSZ and 10YSZ, respectively. The activation energies for the first relaxation peak are similar, but slightly lower than the determined activation energy for anelastic or dielectric relaxation of $\left(Y_{Zr}^{'}V_{O}^{\bullet\bullet}\right)^{\bullet}$ dipoles using other experimental methods. The mechanism responsible for the second damping peak is still not fully understood, though it is theorized to be the result of local ordering of oxygen vacancies or anelastic relaxation of more complex $\left(2Y_{Zr}^{'}V_{O}^{\bullet\bullet}\right)^{x}$ dipoles.

Similar to YSZ, the mechanical damping peaks for GSZ were deconvoluted into two major peaks and the activation energies were found to be 1.45 eV and 2.39 eV. The mechanisms responsible for the first damping peak is likely due to the reorientation of $\left(Gd_{Zr}^{'}V_{O}^{\bullet\bullet}\right)^{\bullet}$ dipoles due to anelastic relaxation while the mechanism for the second damping peak is likely due to more complex dipoles or local ordering of oxygen vacancies.

The anelastic relaxation of SCZ is more complex than that of YSZ and GSZ. In this case, they were deconvoluted into three different mechanical damping peaks. The first damping peak has an activation energy of 1.02 eV and is attributed to anelastic

relaxation of $\left(Sc_{Zr}^{'}V_{O}^{\bullet\bullet}\right)^{\bullet}$ dipoles similar to YSZ. The second damping peak was also occurred similarly to the second damping peak in YSZ and has an activation energy of 1.51 eV. The mechanism behind the peak is thought to be related to local ordering of oxygen vacancies or more anelastic relaxation of more complex dipoles. This peak has been typically overshadowed by stress induced phase transformation peaks in other methods and has not been clearly observed before now. The final damping peak is frequency independent and occurs in a temperature range where the cubic to rhombohedral phase transition occurs.

The calculated activation energies from RUS for all samples were compared to the difference between the dopant ionic radius and the host Zr^{4+} ionic radius. A linear trend was observed corresponding to lower activation energies for dopants with a closer ionic radius to Zr^{4+} which minimizes the strain in the lattice.

The mechanical behavior of stabilized zirconias makes them suitable for a wide range of solid state ionic applications at high temperature. The large mechanical damping seen in these materials at high temperature is comparable to some polymer materials making them suitable to endure large internal stresses during heating and cooling cycles.

4. ELASTIC PROPERTIES AND ANELASTIC RELAXATION OF PURE AND GD3+, LA3+, SM3+ AND Y3+ DOPED CERIAS WITH TEMPERATURE AS DETERMINED BY RESONANT ULTRASOUND SPECTROSCOPY

4.1 Summary

In this paper, we report on the effect of the type of doping cation (Gd^{3+}, La^{3+}, Sm^{3+}, and Y^{3+}) on elastic properties and anelastic relaxation of doped ceria. For comparison, elastic properties of pure stoichiometric ceria (CeO_2) and reduced ceria ($CeO_{2-\delta}$) were also examined. Young's and shear moduli of pure and doped cerias were determined using Resonant Ultrasound Spectroscopy (RUS) in the 25 – 1000 °C temperature range. In addition, the ultrasonic attenuation (mechanical loss or internal friction, Q^{-1}) was determined as the full width at the half maximum of the resonant peaks at different frequencies and temperatures. It was found that although the elastic moduli decrease monotonically with temperature, Q^{-1} shows a frequency dependent maximum at different temperatures ranging from 100 °C to 300 °C for differently doped ceria. This phenomenon is discussed in more detail in the paper in the light of the anelastic relaxation of oxygen vacancy-dopant associates by oxygen vacancy hopping.

4.2 Introduction

Traditionally, fully stabilized doped zirconias have been widely used as solid state ionics (SSIs) in electrochemical devices, such as Solid Oxide Fuel Cells (SOFCs), sensors, gas separation membranes, etc.[5, 148, 174] because of their high oxygen diffusivity and ionic conductivity, low electronic conductivity and phase stability at high

temperature. However, good transport properties can be achieved in those materials only at relatively high temperatures (above ~800 ºC)[10, 90-92]. Reducing the operating temperature of solid state electrolyte would greatly reduce operating costs and extend the lifetime of the SOFCs and other solid state electrochemical devices[175]. Doped cerias have been consider in recent years as potential materials for SOFC electrolyte materials due to their high ionic conductivity in the intermediate temperature range for SOFC operation[33, 175-177]. They have been also used in oxygen sensors and gas separation membranes, among other applications[178-180]. High ionic conductivity is a result of doping cerium oxide with aliovalent dopants creating oxygen vacancies in the material according to the following defect reaction expressed using the Kroger-Vink nomenclature[55]:

$$R_2O_3 \xrightarrow{CeO_2} 2R'_{Ce} + V_O^{\bullet\bullet} + 3O_O^x \qquad \textbf{(4.1)}$$

where R is a rare-earth dopant. A large amount of work has been done on studying the point defects and transport properties in these materials. Eguchi et al.[27] studied the effects of dopant ion radius on ionic conductivity of doped ceria and found that the maximum ionic conductivity occurs at dopant ionic radius r_d = 1.09 Å, corresponding to the radius of Sm^{3+}. Anderson and Nowick[44] observed a trend in which high activation energies for ionic conductivity resulted when the ionic radius between the host ceria ion and the dopant ion was larger. Kilner et al.[181] postulated that the ionic conductivity in all oxides with fluorite structure, including ceria, is maximized when the addition of a dopant and the resulting oxygen vacancies cause the least amount of elastic strain on the crystal lattice[182]. Kim[46] developed a model for prediction the elastic lattice strains in

oxides with fluoride structure as a function of differences between ionic radii of the host and dopant atom and found that 1.038 Å a critical dopant radius, r_c, for a trivalent dopant in ceria. The critical ionic radius is the radius at which no expansion or contraction of the lattice will occur in the host fluorite lattice as a result of adding dopant ions. Other models have predicted different values for critical ionic radius of dopant, ranging from 1.010 – 1.038 Å[43, 47]. Previous work has shown that Gd^{3+} has the closest ionic radius to r_c and is among the highest ionic conductivity[2, 32, 48]. The critical ionic radius also effects the position of dopant ions relative to oxygen vacancies in the crystal structure, which affects the relaxation processes in these materials.

Anderson and Nowick[73] demonstrated for the first time anelastic relaxation in yttria doped ceria (YDC). They carried out mechanical spectroscopy of YDC using flexural vibrations at 8 kHz, and showed two internal friction peaks and different temperatures, that were related to relaxation of $\left(Y_{Ce}^{'}O_O^x\right)^{\bullet}$ and $\left(2Y_{Ce}^{'}O_O^x\right)$ defect clusters by oxygen vacancy hoping. This process is a time-dependent response under the external stress field that arises from the reorientation of point defects within doped cerias[59, 80]. Wachtman[57] proposed the commonly held model that the oxygen vacancy sits in one of the eight nearest neighbor positions around the dopant ion doped oxides with fluorite structure, **Figure 4.1**, and that it can hop around dopant under an external field. The oxygen vacancy and dopant clusters (such as $\left(R_{Ce}^{'}O_O^x\right)^{\bullet}$ and $\left(2R_{Ce}^{'}O_O^x\right)$) form both elastic and electric dipole, which in turn gives rise to anelastic relaxation under a stress field and dielectric relaxation under an electric field[58, 59, 80, 183]. The later was experimentally

observed in numerous mechanical and dielectric spectroscopy studies[31, 36, 58, 73, 183-190] on ceria oxides doped with different cations. As a result of reorientation of those electo-elastic dipoles, doped carries also show a giant electrostriction under electric field[191].

In reducing environments, it is thermodynamically favorable for Ce^{4+} reduces to Ce^{3+} [49]. This reduction in valency is accompanied by a large increase in ionic radius from 0.97 pm to 1.143 pm which can cause micro-cracks in the material and lead to failure in the SOFC due to large volume changes[43, 192]. Using the Kroger-Vink notation, the reduction of ceria can be written as

$$2Ce_{Ce}^{x} + O_{O}^{x} \leftrightarrow V_{O}^{\bullet\bullet} + 2Ce_{Ce}^{'} + 1/2\,O_2(g) \quad [51] \qquad \textbf{(4.2)}$$

It has been well documented that reduced ceria ($CeO_{2-\delta}$) keeps its fluorite structure at non-stoichiometry's up to $\delta = 0.22$[54] and that the reduced Ce^{3+} ion pairs with oxygen vacancies to form point defect complexes such as $\left(Ce_{Ce}^{'}V_{o}^{\bullet\bullet}\right)^{\bullet}$ [193] which are similar to those seen as doped cerias. Therefore reduced can also result in anelastic and dielectric relaxation in reduced ceria, like in the case of doped ones.

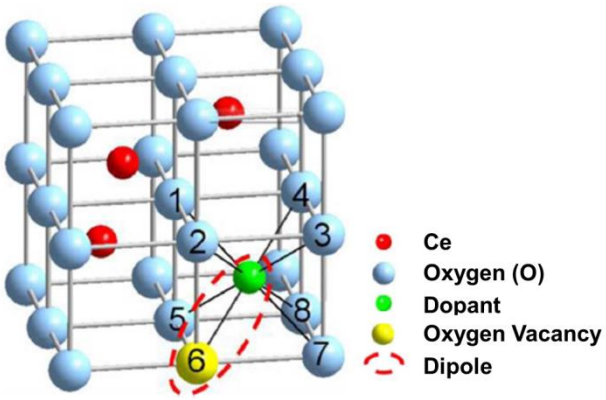

Figure 4.1. Defect structure after adding aliovalent dopant to ceria. The resulting dipole causes anelastic and dielectric relaxation under both elastic and electric fields.

Anelastic relaxation in doped ceria was typically studied at low frequencies that are several of orders of magnitude lower than natural relaxation frequencies of oxygen vacancy hopping in doped cerias, using a flexural resonant vibrations[31, 73]. However, a recent study by Bolon et al.[141] showed that anelastic relaxation in another doped oxide with fluorite structure, namely fully stabilized zirconias can be studied by Resonant Ultrasound Spectroscopy (RUS) and much higher frequencies (> 20 kHz). Resonant Ultrasound Spectroscopy (RUS) is a relatively novel and highly accurate technique for characterizing the elastic properties of a solid that is becoming increasingly popular[103, 112, 115, 116, 160, 194]. In RUS, the elastic constants of the solid are determined using a nonlinear inversion iterative algorithm from the measured natural resonance frequencies, and for known shape and mass, of the sample. While the elastic constants represent primarily equilibrium thermodynamics, the attenuation or damping is a manifestation of

irreversible processes due to energy absorption by various physical entities[100, 114]. The attenuation or damping of a RUS resonance peak is defined as the full width half maximum of the particular resonant peak. RUS is a very sensitive technique to study defect motion in the high frequency range[100]. For example, Foster and Leisure, et. al.[162], used RUS to study hydrogen and deuterium motion in $TaV_2D_{0.17}$ and $TaV_2H_{0.18}$, and found large attenuation peaks in both materials. From those results they concluded that hydrogen faster moves through the g-sites forming linked hexagons in these materials.

In this study, RUS is used to characterize pure ceria and five different doped cerias including 10 mol% and 20 mol% gadonlina doped ceria (10GDC and 20 GDC respectively), samaria doped ceria (SDC), lanthana doped ceria (LDC), and yttria doped ceria (YDC). The mechanical damping with temperature and frequency will be used to characterize the anelastic relaxation behavior with respect to the dopant radius of doped ceria.

4.3 Experimental Methods

All samples in this study were processed using commercially available powders: (a) pure ceria samples from CeO_2 powders (Alfa Aesar, MA), (b) 10GDC ($Gd_{0.1}Ce_{0.9}O_{1.95}$) samples from 10 mol% gadolinia-doped ceria powders (Fuel Cell Materials, OH); (c) 20GDC ($Gd_{0.2}Ce_{0.8}O_{1.9}$) from 20 mol% gadolinia-doped ceria powders (Fuel Cell Materials, OH); (d) SDC ($Sm_{0.2}Ce_{0.8}O_{1.9}$) from 20 mol% samaria-doped ceria powder (Fuel Cell Materials, OH); (e) YDC from the mixture of CeO_2 and La_2O_3 (Alfa Aesar, MA) to yield composition of $La_{0.2}Ce_{0.8}O_{1.9}$; and (f) LDC from the

mixture of CeO_2 and Y_2O_3 powders (Alfa Aesar, MA) to yield composition of $Y_{0.2}Ce_{0.8}O_{1.9}$. The powders were cold pressed to 1 MPa in a 1 inch cylinder die; the pure ceria samples were then isostatically compressed in a Cold Isostatic Press (AIP, OH) to 275 MPa for 15 minutes. The green samples were then sintered at 1500 °C for 2 hours using heating rate of 5 ºC/min. Samples of each material were cut into parallelepipeds of with dimensions 1.5 cm x 1.25 cm x 0.2 cm. Relative densities of all samples were found to be at least 97% using the Archimedes' method according to the modified standard procedure C20-00[166], described in more detail elsewhere [167, 168].

Reduced ceria samples $CeO_{2-\delta}$ were produced by sintering CeO_2 powders at 1500 °C for 2 hours using heating rate of 5 ºC/min, and followed by fast cooling. After that, samples were tested using RUS and subsequently annealed at 800 °C in air for 50 hours to reach equilibrium stoichiometry, and tested again in RUS. For the weight difference of the samples before and after annealing, the δ in $CeO_{2-\delta}$ was estimated to be around 0.013.

Samples were initially tested at room temperature using a commercially available Quasar RUSpec System (Magnaflux, Glenview, IL) to ensure no microcracking occurred during processing. Samples were then tested in a custom built high temperature and environmental RUS chamber[165] up to 1000 ºC in air. Measurements were taken from 20 kHz to 500 kHz at every 20 °C up to 400 °C, and every 50 °C from 400 °C up to 1000 °C. Elastic properties were determined form the collected resonant spectra using RuSpec RI4000 software (Magnaflux, Glenview, IL). The attenuation of multiple resonant peaks was determined by calculating the full width at half maximum (FWHM) at each

temperature. The attenuation vs. temperature plots for resonant peaks at different frequencies were then deconvoluted assuming a two relaxation peaks model described previously by Nowick[59] and Wachtman[57]. The internal friction (Q^{-1}) is directly related to the attenuation of those resonant peaks which represents the dissipated energy during mechanical excitation by the ultrasonic vibrations[80]. An Arrhenius relationship can be used to describe the frequency and temperature dependent relaxation processes as a result of the defect motion, assuming single Debye relaxation model:

$$f = f_o \exp\left(\frac{-E_A}{kT}\right) \qquad \textbf{(4.3)}$$

where f is testing frequency, T is temperature at which maximum Q^{-1} is observed at the particular frequency in relaxation spectra (Q^{-1} vs. T plot), E_A is the activation energy for the relaxation process, k is Boltzmann constant, T is temperature in Kelvin, f_o is the natural relaxation frequency[81]. The activation energy for each sample was calculated based on at least four different resonant peaks.

4.4 Results and Discussion

Both Young's (E) and shear (G) moduli were determined using RUS at different temperatures and their normalized values, i.e. E/E_{RT} and G/G_{RT} where E_{RT} and G_{RT} are Young's and shear moduli at room temperature, respectively, and plotted in **Figure 4.2 and Figure 4.3**. Both the normalized Young's (**Figure 4.2**) and shear (**Figure 4.3**) moduli appear to decrease monotonically with temperature to approximately 80% of the

room temperature value at 1000 ºC. The room temperature values for the Young's and shear modulus are given in **Table 4.1** along with their relative densities.

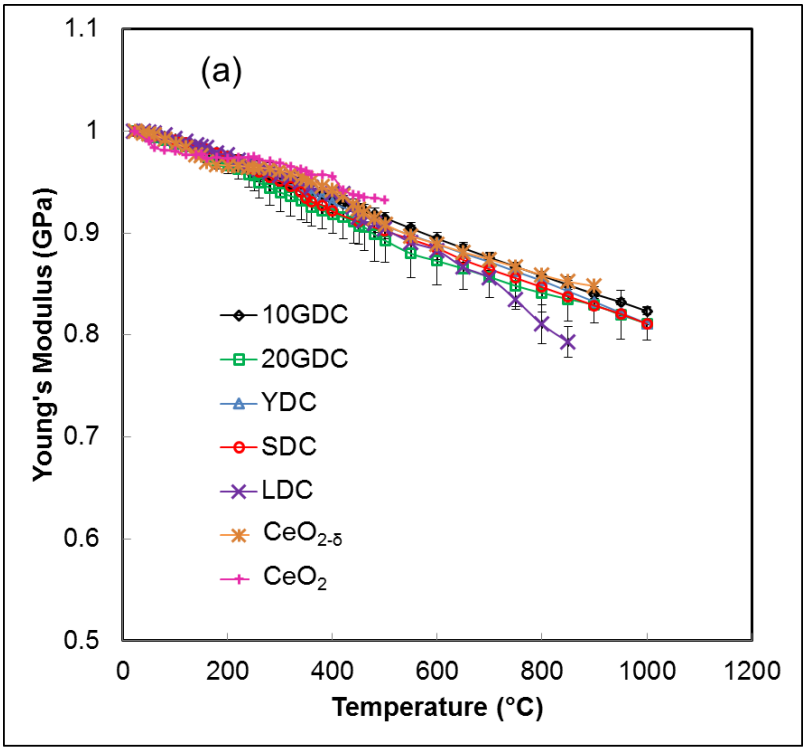

Figure 4.2. (a)Young's moduli (E) and (b) their derivatives (dE/dT) pure stoichiometric and nonstoichiometric ceria and for all doped ceria samples determined using RUS in 25-1000 °C temperature range

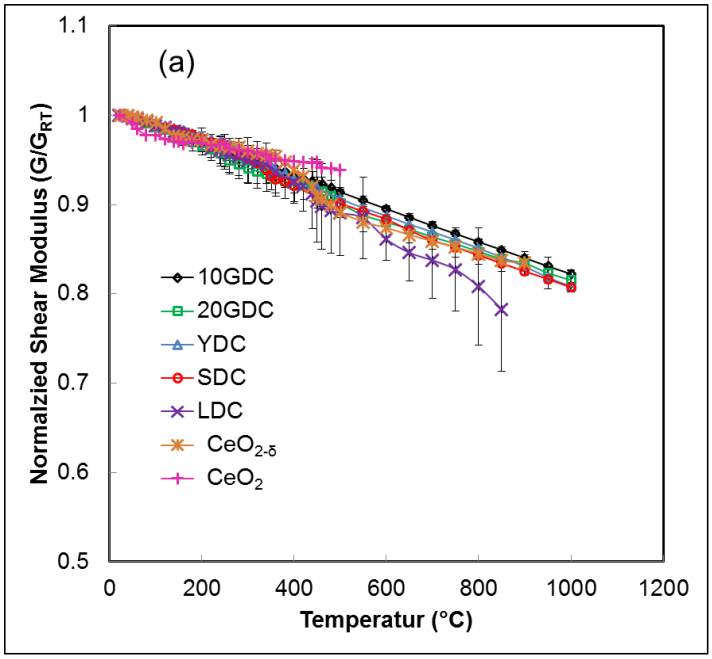

Figure 4.3. (a) Shear moduli (G) and their (b) derivatives (dG/dT) pure stoichiometric and nonstoichiometric ceria and for all doped ceria samples determined using RUS in 25-1000 ^{o}C temperature range.

Table 4.1. The room temperature Young's and Shear moduli for the pure stoichiometric and nonstoichiometric ceria and for all doped ceria samples determined using RUS with their relative densities.

	Ionic Radius of Dopant Ion (Å)[195]	Room Temperature Young's Modulus (GPa)	Room Temperature Shear Modulus (GPa)	Relative Density (%)
10GDC	Gd^{3+}: 1.053	203.29 ± 1.00	77.74 ± 0.24	97.95 ± 1.26
20GDC	Gd^{3+}: 1.053	198.40 ± 3.37	75.85 ± 1.33	98.01 ± 0.19
YDC	Y^{3+}: 1.019	203.37 ± 0.07	77.85 ± 0.08	99.08 ± 0.08
SDC	Sm^{3+}: 1.079	198.69 ± 0.18	75.99 ± 0.33	98.28 ± 1.33
LDC	La^{3+}: 1.160	186.79 ± 6.18	71.28 ± 2.57	97.99 ± 1.32
$CeO_{2-\delta}$	Ce^{3+}: 1.143	205.67	78.41	96.64
CeO_2		179.93	69.65	96.64

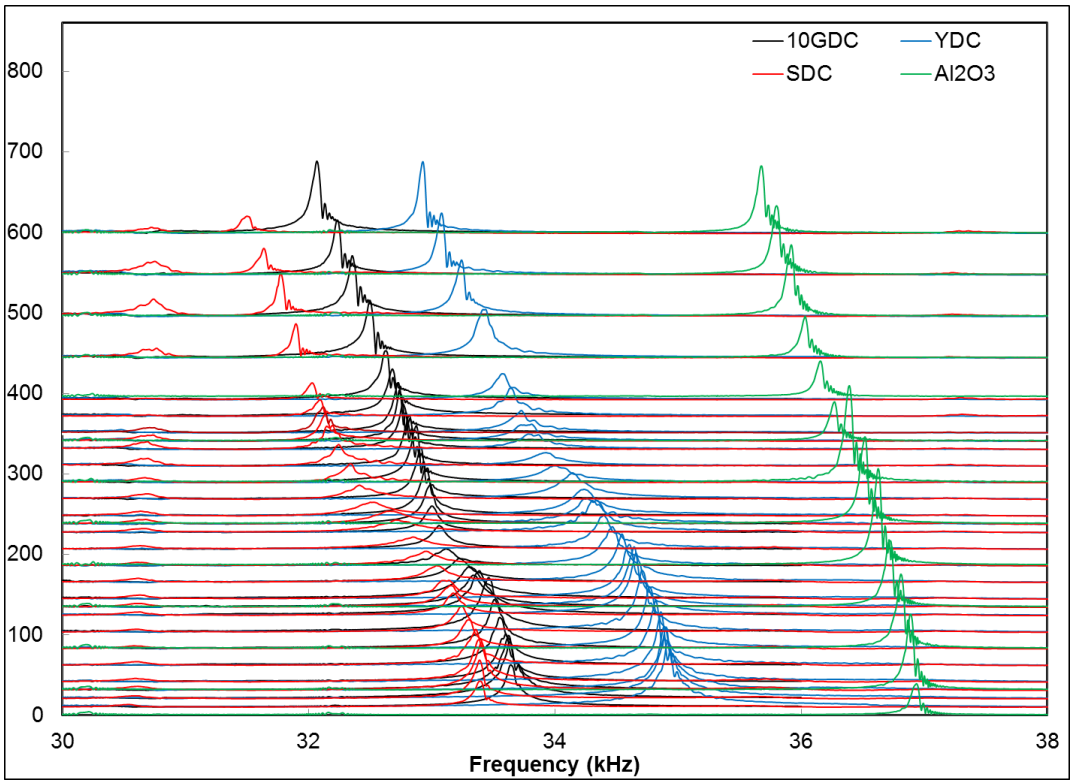

Figure 4.4. Typical, but selected part of resonant spectra obtained using RUS for 10GDC, SDC, and YDC and Al_2O_3.

A selected part of the resonant spectra obtained by RUS between 30 and 38 kHz for 10GDC, YDC, SDC are shown in **Figure 4.4,** together with the spectra of alumina (Al_2O_3) for comparison. The resonant peak for alumina does not broaden significantly with temperature up to 600 °C, and its intensity does not decrease abruptly in any temperature range, **Figure 4.4.** This is expected since no anelastic relaxation occurs in alumina in that temperature range. However, resonant spectra of 10GDC, SDC and YDC illustrated in **Figure 4.4** show a distinct broadening and drop in intensity of the resonant

peaks within different temperatures ranges for each doped ceria. For example, this broadening occurs in SDC over the largest temperature range from ~200 °C to ~350 °C, while in 10GDC and YDC it happens in ~150-250 °C and ~200-400 °C temperature range, respectively. The broadening of resonance peaks is indicative of high ultrasonic attenuation due to internal friction or mechanical damping (Q^{-1}). Note here that peak positions in **Figure 4.4** moves steadily to lower frequencies with increasing temperature, indicating monotonic decrease in elastic moduli as shown in **Figure 4.1.**

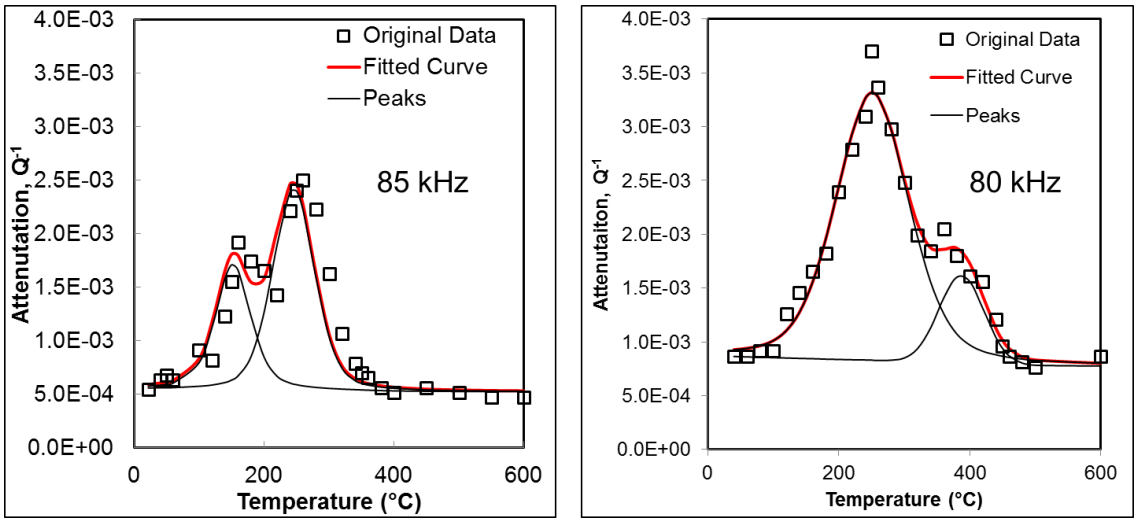

Figure 4.5. Attenuation of the of the resonant peaks at ~80 kHz as a function temperature for (a) 20GDC and (b) LDC are determined by from FWHM for each resonant peak at each temperature.

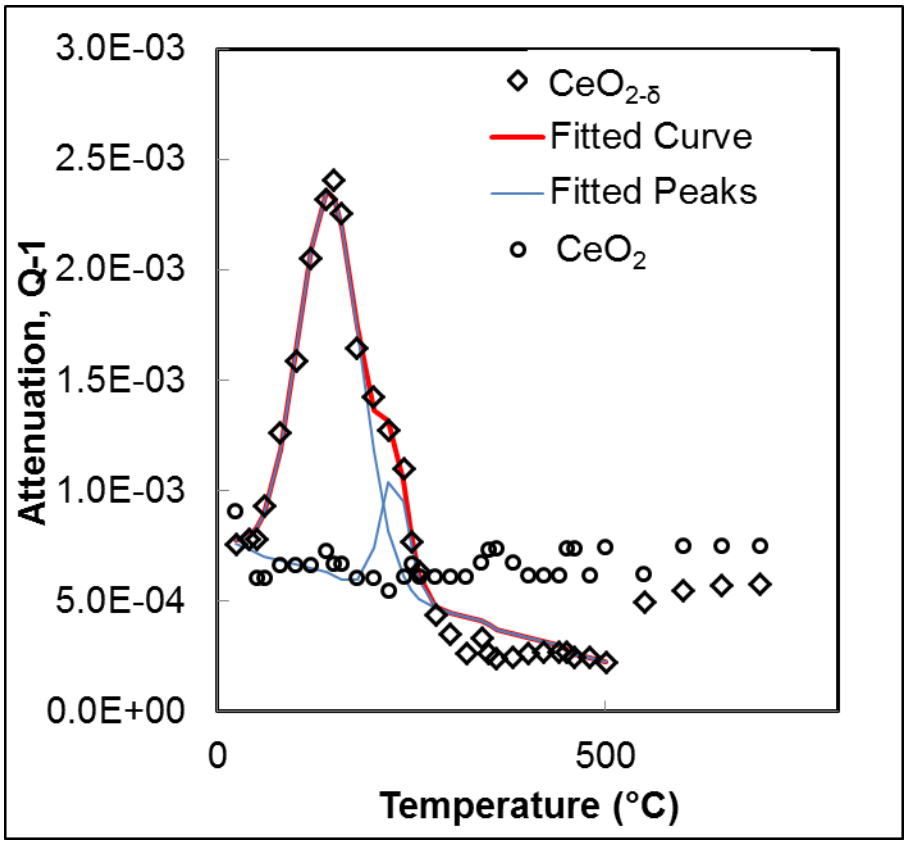

Figure 4.6. The attenuation of the resonant peak at around 180 kHz as a function of temperature for of reduced ceria (diamonds) show two relaxation peaks at low temperatures while the annealed samples (circles) shows no peaks are remains relatively constant over the entire temperature range.

Attenuation (Q^{-1}) for the resonant peaks at different frequencies were determined as a function of temperature from the FWHM of each resonant peak using procedure described in more details earlier. Selected but typical relaxation plots are presented in **Figure 4.5** for the resonant peak at ~80 kHz observed in RUS spectra of 20GDC and LDC. While both attenuation curves show two distinct relaxation peaks where Q^{-1} reaches local maxima, the size and location of the relaxation peaks are different for

samples with different dopants. Like the doped ceria samples, the reduced ceria sample also shows two attenuation peaks at low temperature, as it is illustrated in **Figure 4.6**. As a result of the Ce^{4+}reduction to Ce^{3+}, the Ce^{3+} ion acted like a dopant ion on the system creating an elastic and electric dipole in the material. After annealing, the attenuation of the sample was relatively constant across the entire temperature range indicating that no anelastic relaxation processes take place in the material.

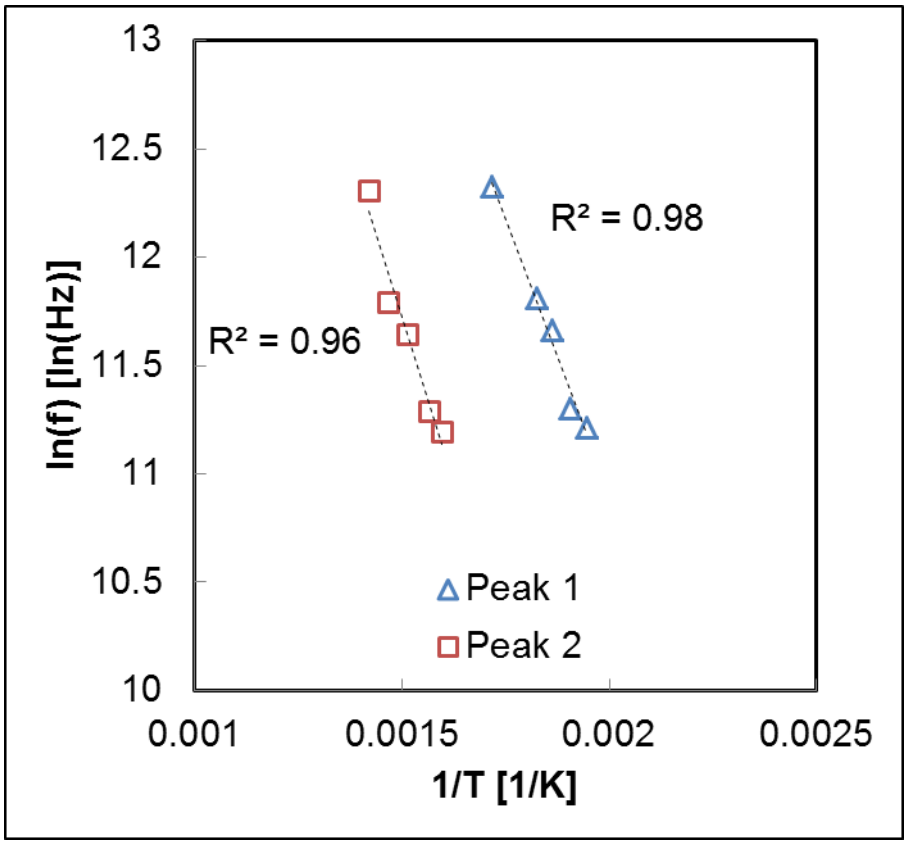

Figure 4.7. Arrhenius plot of LDC for both relaxation peaks observed.

Plots (not shown here) similar to those illustrated in **Figure 4.5 and Figure 4.6** are constructed for 5 resonant peaks at different frequencies, and deconvoluted using XPSPEAK4.1 (The Chinese University of Hong Kong, Hong Kong) assuming two major relaxation peaks (black lines in **Figure 4.5**), that are further denoted as Peak I and Peak II. Deconvolution was carried out for all samples except pure ceria where no relaxation peaks were observed. Then, Arrhenius type plots of ln*f* vs. 1/T such that shown in **Figure 4.7** for LDC sample are plotted, where *f* is a frequency of the resonant peak and T is temperature of the attenuation maxima for Peaks I and II determined from deconvoluted relaxation spectra at each resonant frequency. Those plots can be further used to determine activation energies of the relaxation mechanism responsible for the observed relaxation Peaks I and II from the slopes of ln*f* vs. 1/T lines, assuming that each of them can be model using single Debye relaxation model described earlier. For example, **Figure 4.7** shows Arrhenius plots for LDC sample. The values for the activation energies determined for Peak I and II in this study are shown in **Table 4.2.**

The activation energies for both major relaxation peaks also plotted as blue diamonds (peak 1) and red squares (peak 2) in **Figure 4.8** vs. the difference between the dopant radius and the host radius, and in **Figure 4.9** vs. the difference between the dopant radius and critical dopant radius of 1.038 Å[46]. These results were then compared to activation energies for anelastic relaxation in YDC[73, 188] and Scandia doped Ceria (ScDC)[31] determined using forced flexural vibration method. Since anelastic relaxation in ceria is believed to be caused by reorientation of defect complexes, that in the same time form not only elastic but also electric dipoles, activation energies for

anelastic relaxation are compared to those of dielectric relaxation [31, 36, 48, 184, 196-201] in **Figure 4.8 and Figure 4.9.** Results in **Figure 4.8 and Figure 4.9** suggest that activation energies for both anelastic and dielectric relaxations are in general increasing with increasing dopant radius. Increasing dopant radius causes larger elastic strains around dopant, and thus higher activation energies are required for reorientation of dipoles by oxygen vacancy hoping in vacancy-dopant complexes. At higher dopant radii (such as in case of La^{3+} and Ce^{3+}) activation energies for anelastic and dielectric relaxation decreases again with increasing dopant radius, most likely because of weaker electrostatic attraction between them.

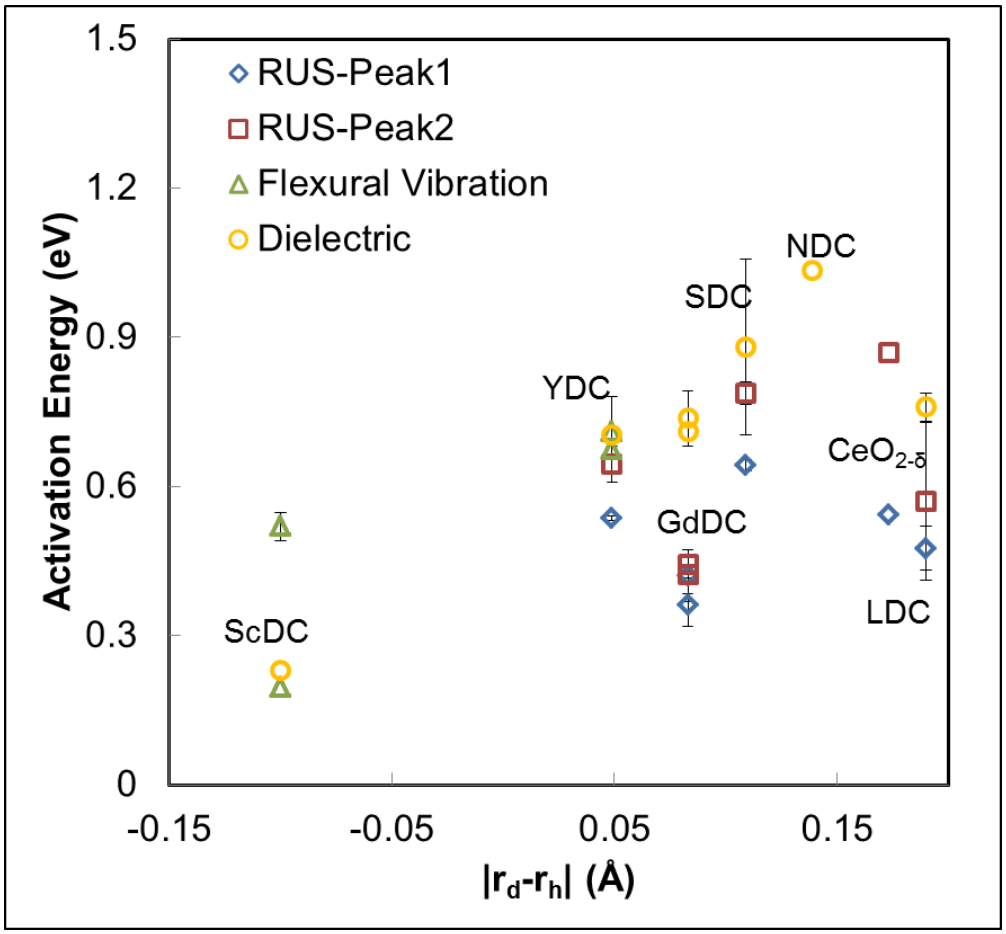

Figure 4.8. Activation energy vs. difference in dopant radius to host radius comparing RUS and data with those obtained using other mechanical spectroscopy methods such as forced flexural vibrations [31, 73] and dielectric relaxation [31, 36, 48, 184, 196-201].

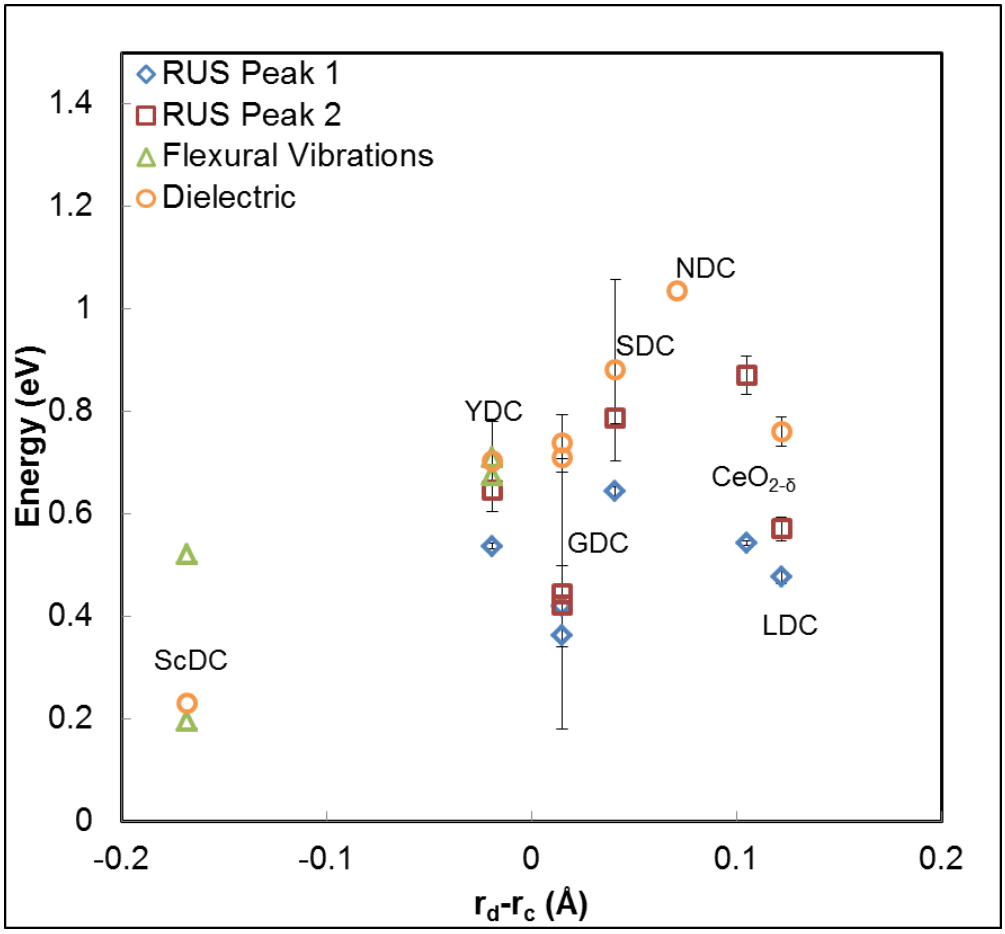

Figure 4.9. Activation energy vs. difference versus difference in dopant radius to critical ionic radius of 1.038 Å[46] comparing RUS with those obtained using other mechanical spectroscopy methods such as forced flexural vibrations [31, 73] and dielectric relaxations [31, 36, 48, 184, 196-201].

Table 4.2. Activation energy values for all samples calculated using RUS, and literature values for anelastic relaxation, and dielectric relaxation.

Material	RUS Peak 1 (eV)	RUS Peak 2 (eV)	Anelastic Lit (eV)	Dielectric Lit (eV)
SDC	0.64 ± 0.011	0.78 ± 0.022	----	0.88 ± 0.176[48]
YDC	0.53 ± 0.004	0.64 ± 0.036	0.68[73] 0.71	0.70 ± 0.077[36, 196-198]
10 GDC	0.42 ± 0.052	0.44 ± 0.028	----	0.74 ± 0.055[201]
20 GDC	0.36 ± 0.042	0.42 ± 0.037	----	0.71[201]
LDC	0.47 ± 0.044	0.57 ± 0.159	----	0.76 ± 0.028[48, 200]
NDC	----	----	----	1.04[196]
ScDC	----	----	0.195[31] 0.52 ± 0.028	0.23[31]
$CeO_{2-\delta}$	0.54	0.87	----	----

While these slight trends are observed when compared to the critical ionic radius for the host cations, more work needs to be done to determine the exact physical nature of this trend. Recent computation studies suggest that different defect clusters are forming based on the type and size of dopant in ceria. Andersson et al.[29] stated that the transition point between nearest neighbor and 2NN is with Promethium and the elements to the right on the periodic table favoring the 2NN position, and those to the left favoring the nearest neighbor position. However, they were only looking at the effects of electrostatics on the energies and not the lattice sizes. Nakayama and Martin[70] looked at various different rare-earth dopants in ceria and found that dopants larger than Gd^{3+} prefer to sit in the second nearest neighbor (2NN) distance while dopants that are smaller prefer the nearest neighbor position. This is slightly confirmed by studies done by Dholabhai et al. on SDC[202] and Praseodymium doped ceria (PDC)[203]. Additionally,

when looking at significantly smaller dopants like scandia, the tendency to form larger defect clusters is much higher than with larger dopants like Gd^{3+} or Y^{3+}. Experimental results from Kossey et al.[71] show through EXAFS studies of thin films that the oxygen vacancy sits NN to ceria ions instead. However, molecular dynamics calculations by Inaba et al.[72] show that at high temperatures, gadolinia prefers to form Gd-Gd pairs within the system as a nearest neighbor to an oxygen vacancy[72]. Conversely, studies by Ahn et al.[42] indicate that the Gd^{3+} ion prefers to sit nearest neighbor to the oxygen vacancy especially under compressive strains. The variety of positions of the dopant ion compared to the oxygen vacancies and the resulting defect clusters make it hard to directly compare only by one the differences in ionic radii of the materials.

4.5 Conclusion

Resonant ultrasound spectroscopy (RUS) study of pure and reduced ceria, 10 mol% and 20 mol% Gadolinia doped ceria (10GDC and 20GDC), 20 mol% samaria doped ceria (SDC), 20 mol% yttria doped ceria (YDC), and 20 mol% lanthana doped ceria (LDC) was carried out from room temperature to 1000 °C in the 20 to 500 kHz range is presented. The Young's and shear modulus show a consistent monotonic decrease across the entire temperature range for all samples.

The mechanical damping curves were deconstructed into two relaxation peaks for each doped ceria and reduced ceria and the activation energies were calculated. These energies were plotted against either the difference between the dopant radius and the ionic radius of Ce^{4+} or the dopant radius and the critical ionic radius to observe

trends. Both show an initial increase in activation energy with the difference in radii before the energy starts to decrease again. The mechanisms behind observed differences in activation energies for anelastic relaxation among ceria samples doped with aliovalent cations of different size can be most likely associated to the different structure of vacancy-dopant clusters.

5. MULTIPLE RELAXATION MECHANISMS IN 8YSZ

5.1 Summary

In this study, the mechanical damping peaks produced by Resonant Ultrasound Spectroscopy (RUS) of 8 mol% yttria stabilized zirconia (8YSZ) were further studied to understand the number of relaxation mechanisms occurring within the material. The previous assumption of two Debye peaks did not match the data when the relaxation curves were reconstructed. Models with more peaks were tested to determine the optimal number of peaks to fit the mechanical damping peaks. It was found that a six peak model minimizes the RMS error between the reconstructed curve and the experimental data.

5.2 Introduction

It has been shown in previous studies that yttria stabilized zirconia (YSZ), with cubic (fluorite) stricture shows two major anelastic relaxation peaks[141]. These peaks were originally attributed to be the reorientation dopant ion-vacancy complexes that form elastic dipoles[57, 59, 80, 183, 204], with oxygen vacancy having one or two dopant ions in the first nearest neighbor (1NN) position. However, recent computational studies have suggested that the oxygen vacancy prefers at a second nearest neighbor (2NN) position to the dopant cation while maximizing the space between other oxygen vacancies along the <111> direction due to local relaxations within the material[13, 61, 67, 68]. There are two prevailing theories that support this configuration. Bogicevic and Wolverton[68] report that the elastic interaction between the dopant ion and oxygen vacancy is repulsive

causing the dopant ion and vacancy to be 2NN configuration, rather than in 1NN. This also explains why the vacancies are preferentially 3NN to one another as the elastic interactions are attractive in that case. The other explanation is that oxygen vacancy in the 2NN configuration leads to eightfold coordination around the Y^{3+} ion that similar to its coordination in Y_2O_3 and sevenfold coordination around the Zr^{4+} ion similar to its coordination in the preferred low temperature monoclinic phase[13, 69]. The later has been also confirmed experimentally using Extended X-Ray Absorption Fine Structure (EXAFS)[63, 64], neutron diffraction[149], and Nuclear Magnetic Resonance (NMR)[66].

Stapper et al.,[13] modeled the relaxation effects of isolated defects and in a solid solution using *ab initio* density functional theory framework in the local density approximation (DFT-LDA). When an Y^{3+} ion is added as a 2NN to oxygen vacancy, the oxygen atoms surrounding oxygen vacancy move closer to the vacancy while the nearest zirconium atom and the other oxygen atoms move away in the <111> direction. When the Y^{3+} ion is 1NN to the oxygen vacancy, the Y^{3+} ion moves outward while the oxygen atoms closest to both the vacancy and Y^{3+} ion move less towards the oxygen vacancy than in the case when the Zr^{4+} ion is nearest neighbor to the oxygen vacancy. These models can be used to understand the relaxation motion within the solid solution.

These theoretical studies examined not only the various preferential locations of the oxygen vacancies relative to the dopant ion and other oxygen vacancies in unstressed structures, but the activation energy for the oxygen vacancy as it moves hoping in different configurations. The oxygen ion jumps between caters of two cation tetrahedrons, where it must pass between two cations, as illustrated in **Figure 5.1**. For

example, **Figure 5.1** shows two zirconia tetrahedrons in cubic zirconia, where (a) shows the position of the tetrahedron in the fluorite unit cell and (b) shows the reverse fluorite cell with an additional layer to complete the tetrahedron. In YSZ, there are basic configurations that can occur, depending on which site in the tetrahedral is occupied by dopants, as it is illustrated in **Figure 5.2.** The oxygen vacancy can (i) hop between two zirconia ions, (ii) hop between one zirconia and one dopant ion and (iii) hop between two dopant ions. Each of these types produces a range of activation energies since the surround ions have a large influence on the energy barrier for hopping. Pornprasertsuk, et. al.[205] calculated activation energies in the ground state for 42 different cases of cations' positions within the tetrahedrons. Summarized results of the activation energies from multiple studies[26, 205, 206] are given in **Table 5.1** separated by the type of barrier to oxygen ion must go through. The lowest energies are for the Zr-Zr barrier regardless of the position of the other atoms in the tetrahedron. The Zr-Y barrier had the next lowest activation energies and the Y-Y barrier has the highest activation energies.

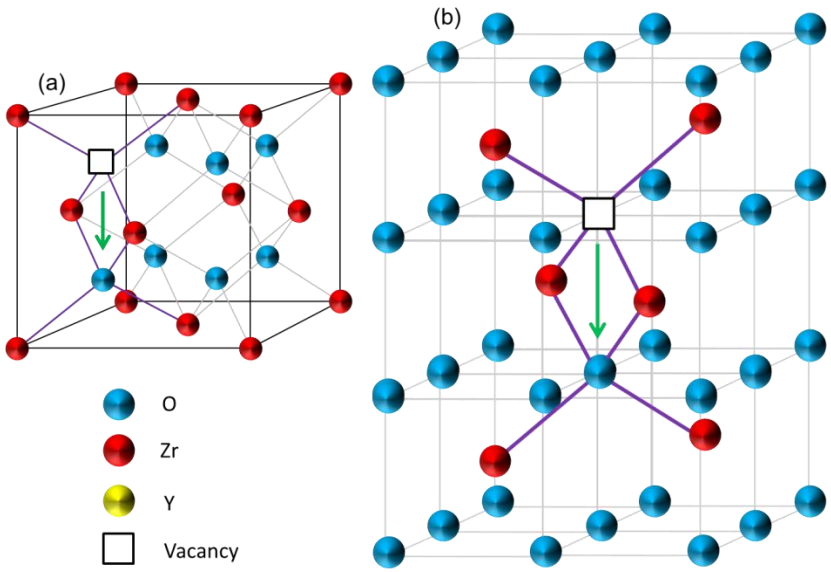

Figure 5.1. The position of the tetrahedrons in which hopping of oxygen ions occurs, highlighting in the (a) stabilized zirconia fluorite structure and (b) the reversed fluorite structure of stabilized zirconia.

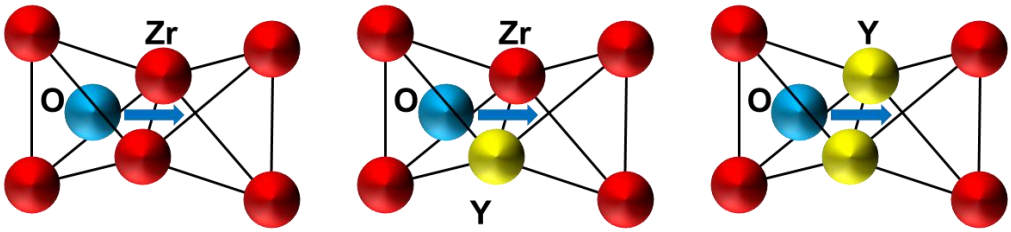

Figure 5.2. Different cases for of the oxygen ion hopping between Zr-Zr, a Zr-Y and a Y-Y cations[60]. The red circles are zirconium ions, blue spheres are oxygen ions and the yellow spheres are yttrium ions.

Table 5.1. Summary of activation energies for a different number of nearest (1NN) or next nearest neighbor (2NN) cations in the tetrahedron in which hopping occurs[26, 205, 206].

Barrier 1: Zr-Zr			
NN-NN	NN-2NN	2NN-NN	2NN-2NN
0.28-0.7 eV	0.2-0.23 eV	0.40-0.8 eV	0.3-0.67 eV
Barrier 2: Zr-Y			
NN-NN	NN-2NN	2NN-NN	2NN-2NN
0.79-1.09 eV	0.7-0.88 eV	0.71-0.94 eV	0.85-1.29 eV
Barrier 3: Y-Y			
NN-NN	NN-2NN	2NN-NN	2NN-2NN
	1.20 eV	1.40 eV	1.23-2.3 eV

The lowest energies Pornprasertsuk et al.[205], Kushima et al.[206]and Krishnamurthy et al.[26] observed were in cases when the oxygen vacancy was moving away from yttria in nearest neighbor positions. In addition to the nearest neighbors, the second and third nearest neighbors also have an effect on the energy barrier the atom most overcome to move. Kushima et al[61] modeled the contributions of the number of Y^{3+} ions in 2NN positions and where the nearest oxygen vacancy was located using density functional theory on a plane wave basis set. They found that the Zr-Zr barrier was the smallest with a maximum energy barrier of approximately 0.5 eV. They also found that the relative position of the nearest oxygen vacancies had more effect on the energy than the number of 2NN Y^{3+} ions. They concluded from the study that vacancy-vacancy interactions dominate the vacancy-cation interactions when determining energy barriers. However, this study did not include Y-Y energy barriers[61]. The high energy barrier associated with Y-Y barriers explains the decrease in ionic conductivity with increased

amount of Y doping because the more Y_2O_3 is used for doping, the more likely Y-Y pairs will form and "block" the oxygen vacancy motion[69, 207].

Relaxation processes in materials can be studied from the attenuation of resonance peaks produced by Resonant Ultrasound Spectroscopy, as it was described in more detail in the previous sections. The type of motion and the type of barrier crossed during the motion determine the relaxation process and its activation energy. Previously, it was assumed that only either the anelastic relaxation of the vacancy-dopant dipole $\left(R_{Zr}^{'}V_O^{\bullet\bullet}\right)^{\bullet}$ or more complex vacancy-dopant complexes $\left(2R_{Zr}^{'}V_O^{\bullet\bullet}\right)$ were responsible for the mechanical damping peaks observed. In that case, the calculated mechanical loss, Q^{-1} can be related directly to the motion of point defects within the material and can ideally be described as Debye peaks[56, 81]

$$Q^{-1} = \Delta \frac{\omega\tau}{1+\omega^2\tau^2} \qquad \textbf{(5.1)}$$

where Δ is the relaxation strength which is equivalent to $\Delta = 2Q_{\max}^{-1}$, ω is the frequency and τ is the relaxation time found from an Arrhenius relationship

$$\tau^{-1} = \tau_{\infty}^{-1} \exp\left(\frac{-E_A}{kT}\right) \qquad \textbf{(5.2)}$$

where E_A is the activation energy to cross the barrier, k is Boltzmann constant, and T is temperature in Kelvin. This study looks at 8 mol% and 10 mol% yttria stabilized zirconia (8YSZ and 10YSZ respectively) in detail to determine an approximate number of relaxation processes occurring in these materials assume all processes behave as Debye peaks.

5.3 Results and Discussion

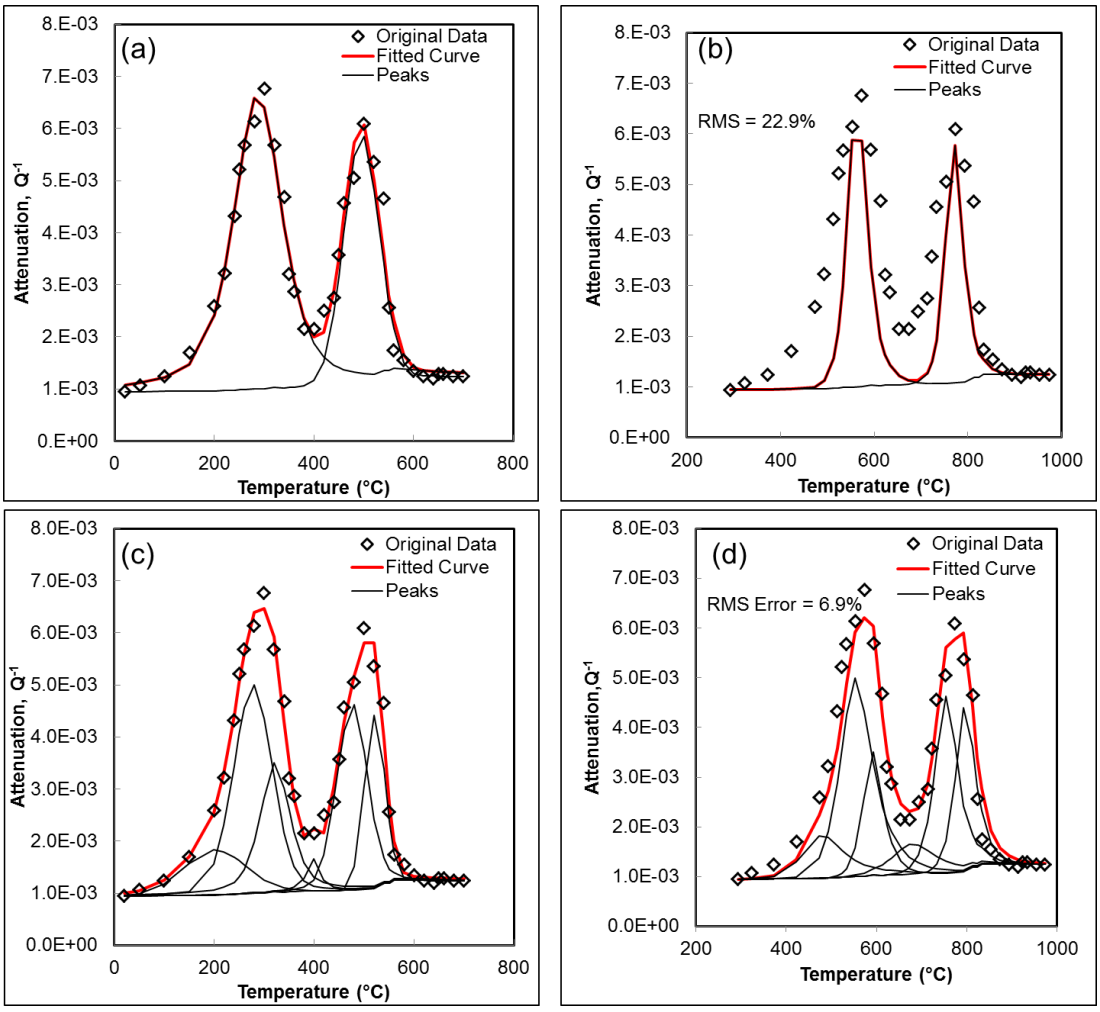

Figure 5.3. (a) The deconvolution of the 90 kHz resonant peak for 8YSZ as determined from RUS assuming only two relaxation peaks. (b) Calculated relaxations spectra using data from parameters from the deconvolution in (a) assuming only two single Debye peaks for giving a 22.9% error between measured and reconstructed relaxation spectra. (c) The deconvolution of the 90 kHz resonant peak for 8YSZ as determined from RUS with the best fit assuming six peaks. (d) The convolution assuming six single Debye peaks for the 90 kHz resonant peak of 8YSZ using the parameters from the deconvolution in (c), giving the error of 6.9% between measured and reconstructed relaxation spectra.

Figure 5.3a shows the attenuation or mechanical damping curve for 8YSZ that was obtained by calculating the full with at half max (FWHM) of the 90 kHz resonant peak fitted assuming a two peak model. However, upon using that model to fit the peaks assuming two single Debye relaxations as proposed by Weller et al. [76, 151, 152], it becomes clear that the model is not adequately describing all the relaxation processes in the material. **Figure 5.3b** shows the reconstructed relaxation spectra based on the parameters calculated from single Debye models, which give an RMS error of 22.9 % for the 90 kHz resonant peak and an average of 29.34 ± 8.48 % for the entire frequency range. It is clear from the **Figure 5.3b**, that measured relaxation peaks are much broader that reconstructed ones, suggesting a larger distribution of relaxation energies and times. The attenuation data were then deconvoluted with four, six, and ten peaks, and the average RMS error between reconstructed relaxation spectra and measured one in all cases are plotted in **Figure 5.4**. The 6 relaxation peak model was adopted for the rest of the fitting as it provides the smallest RMS. Note here that the minimum RMS could potentially be at 5, 7, or 8 peaks, but these conditions were not tried in this study and they will be considered in the future.

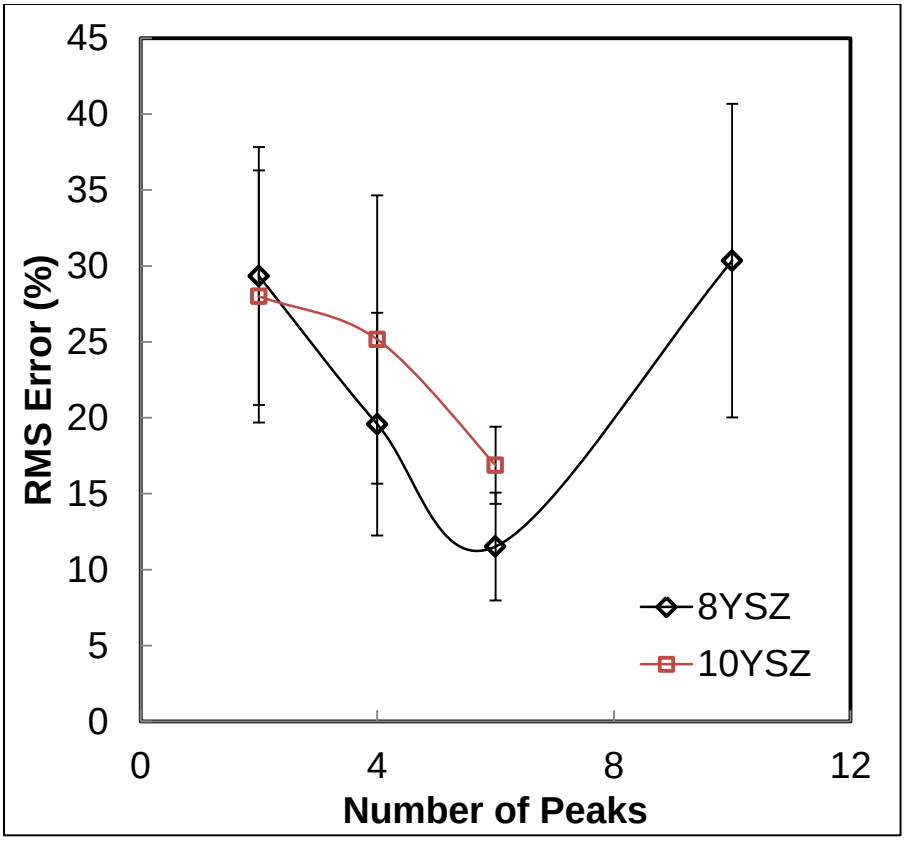

Figure 5.4. A graph of the RMS error between reconstructed relaxation spectra and measured assuming different numbers of single Debye relaxation peaks for 8YSZ and 10YSZ.

The activation energies for anelastic relaxations were calculated using the six peak model, i.e. assuming six different major relaxation mechanisms, for three separate samples and the results are summarized in **Table 5.2,** where the major peak corresponding to the two peak model discussed in more details in the previous sections are highlighted. The activation energies for these two peaks are in good agreement with the results from the two peak model, where the activations energies for Peak I and Peak II are 1.207 eV and 2.181 eV, respectively. Peaks 1, 2, and 4 in this model have lower

activation energies while Peak 6 has a larger activation energy. Comparing to the previous computation studies, Peak 1 is likely due to crossing a Zr-Zr barrier while Peaks 2, 3, and 4 are likely due to crossing a Zr-Y barrier and finally Peaks 5 and 6 are likely due to crossing a Y-Y barrier. Since these are thermally activated processes, it makes sense that the barrier requiring more energy to cross would occur at high temperatures. However, more work needs to be done to completely classify the mechanism responsible for the different peaks.

Table 5.2. The activation energies for the six relaxation processes for 8YSZ, the highlighted peaks correspond to the two major peaks seen in the two peak model.

Peak Position	200-225 °C	270-310 °C	300-330 °C	380-450 °C	470-500 °C	500-530 °C
Average	0.595	0.976	1.246	0.978	1.919	2.443
StDev	0.139	0.124	0.318	0.166	0.219	0.438
			Major Peak 1		Major Peak 2	

10YSZ was also deconvoluted into six major damping peaks similar to 8YSZ, the RMS error for these peaks was slightly higher than 8YSZ at 16.88 ± 2.54 %; however it still had a lower error than two, and four peaks models, shown in **Figure 5.4**. The activation energies for this case were calculated and shown in **Table 5.3.** Similar to the 8YSZ results, the two major peaks can clearly be observed (and are highlighted) with similar activation energies to those determined assuming only two peaks, i.e. 1.178 eV and 2.198 eV for Peak I and Peak II respectively. The remaining peaks show a slightly

different trend, where only Peak 1 and Peak 2 have lower activation energies, while Peak 4 has higher activation energy than Peak 3, and Peak 6 has he smaller activation energy then Peak 5. This is likely due to a higher number of dopants and vacancies in the material clustering.

Table 5.3. The activation energies for the six relaxation processes for 10YSZ, the highlighted peaks correspond to the two major peaks seen in the two peak model.

Peak Position	175-225 °C	250-320 °C	300-390 °C	390-470 °C	470-540 °C	500-610 °C
Average	0.707	1.355	1.602	1.734	2.172	2.051
StDev	0.047	0.371	0.053	0.433	0.246	0.048
			Major Peak 1		Major Peak 2	

5.4 Conclusions

Resonant Ultrasound Spectroscopy results were further studied to elucidate the number of relaxation processes in 8 mol% and 10 mol% yttria stabilized zirconia (8YSZ and 10YSZ, respectively). Four different numbers of peaks were compared and it was found that six relaxation peak model minimize the RMS error between reconstructed and measured relaxation spectra. Within the six peak model, the two major peaks corresponding to the previously assumed two peak model can clearly be observed and have similar activation. The remaining peaks sit on the shoulders of those two peaks and represent different relaxation mechanisms in the material. However, more work needs to be done to determine the specific relaxation process each peak corresponds to and if

there it there is a more ideal number of peaks that can be fit to the mechanical loss spectra.

6. STUDY OF THE EFFECT OF AN ELECTRIC FIELD ON THE ELASTIC PROPERTIES AND ANELASTIC RELAXATION IN YTTRIA STABILIZED ZIRCONIA BY RESONANT ULTRASOUND SPECTROSCOPY

6.1 Introduction

As it has been previously discussed yttrium stabilized zirconia (YSZ) with fully stabilized cubic (fluorite) structure is a common electrolyte material for Solid Oxide Fuel Cells (SOFCs) due to its high ionic but low electronic conductivity, and good stability at high temperatures[9, 11]. Doping with a trivalent dopant like Y^{3+}, introduces one oxygen vacancy per two dopants and stabilizes its high temperature cubic structure down to the room temperature. This study continues the in-depth examination of elastic properties of, and anelastic relaxation in 8 mol% yttria stabilized zirconia (8YSZ). Herein we investigate effect of the electric field on elastic constant and internal friction of 8YSZ at different temperatures. The latter is particularly important as the 8YSZ electrolyte material in SOFC is exposed to electric field of up to 100 V/mm during normal operation.

It has been well established by now that 8YSZ exhibits an anelastic and dielectric relaxation as a result of time dependent reorientation of point defect clusters such as $\left(Y_{Zr}^{'}V_{O}^{\bullet\bullet}\right)^{\bullet}, \left(2Y_{Zr}^{'}V_{O}^{\bullet\bullet}\right)$ or more complex clusters in response to a stress field and electric field, respectively. Both anelastic relaxation and dielectric relaxation share similarities and as thermally activated, time dependent processes they can be described Arrhenius relationship. Anelastic relaxation under a static field can be described using

$$\varepsilon(t)/\sigma = s + \delta s\left[1 - \exp\left(-t/\tau\right)\right] \qquad \textbf{(6.1)}$$

where *s* is the compliance, δs is the relaxation of compliance related to the thermodynamics of the process, σ is stress, and τ is relaxation time. However, under a dynamic field, the anelastic relaxation can be described through a Debye equation as:

$$Q^{-1} = \tan\delta = \Delta\left[\frac{\omega\tau}{1+\omega^2\tau^2}\right] \quad \textbf{(6.2)}$$

where Δ is the relaxation strength, ω is angular frequency, Q^{-1} is internal friction or mechanical damping, and δ mechanical loss. In the case of anelastic relaxation due to point defect hopping, relaxation strength ca be further expressed as[31]:

$$\Delta_{anel} = \frac{\alpha C_d v_0 (\delta\lambda)^2}{SkT} \quad \textbf{(6.3)}$$

where v_0 is the volume per molecule, C_d is the mole fraction of defects, α is a numerical factor of order, S is the average elastic compliance , δλ is the effective component of the elastic dipole tensor. If anelastic relaxation due to hopping of the point defects also causes dielectric relaxation due to the reorientation of electric dipoles, as in the case of vacancy hopping in 8YSZ, then dielectric relaxation strength, Δ_{diel}, can be described as:

$$\Delta_{diel} = \frac{C_d p^2}{3\varepsilon_0 \varepsilon v_0 kT} \quad \textbf{(6.4)}$$

where ε_0 is the permittivity of a vacuum, ε is the relative dielectric constant, and p is the dipole moment[31]. The differences between the two relaxation strengths highlight the differences between anelastic and dielectric relaxation. In order to interact with an electric or elastic field, the point defect must be an electric dipole described by a vector μ or an elastic dipole described by a second rank tensor λ respectively. As stated previously in Section 1, the addition of trivalent dopants results formation of oxygen

vacancies results in trigonal symmetry of the defect. For anelastic and dielectric relaxation to occur, the symmetry of the defect must be lower than the symmetry of the host crystal[80].

Relaxation results from the redistribution of defects among sites that are initially equivalent but become inequivalent under the application of an external field[59, 183]. For instance, assuming a dopant ion is nearest neighbor to the oxygen vacancy (according to Wachtman's model[57] and Weller et al.[76, 154] study), there are eight equivalent positions that the oxygen vacancy could occupy around the dopant ion, the positions are labeled in **Figure 1.3a**. Under the application of an external stresses or electric field, one of the positions will become more favorable for the vacancy, making the positions inequivalent. However, as recent studies have shown, this is not the mostly likely configuration since the oxygen vacancy prefers be in the second nearest neighbor (2NN) position relative to dopant as shown in **Figure 1.3b**[60, 61, 205]. However, the same principle will apply to this case as well, under no external field, the vacancy will sit in equivalent positions 2NN to the dopant ion until the external field is applied and one of those positions becomes more favorable.

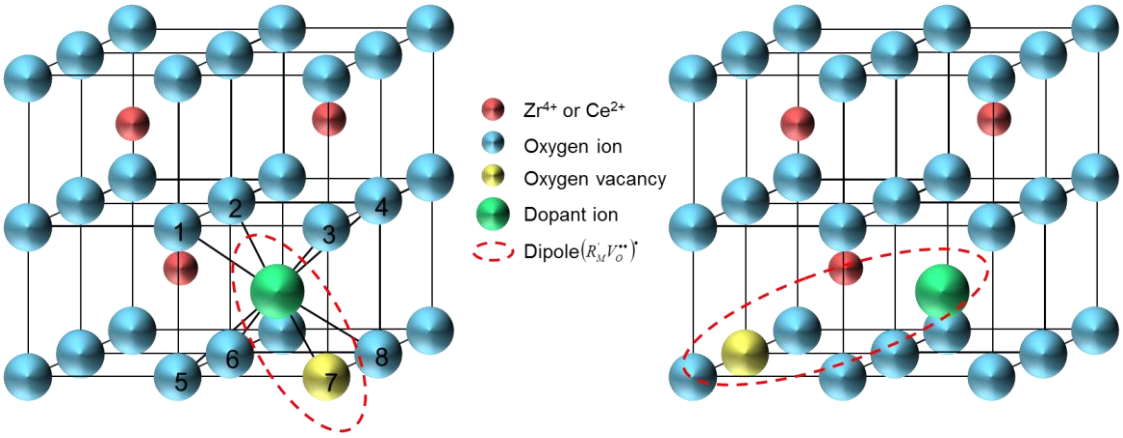

Figure 6.1. (a) Fluorite structure after adding a dopant to the zirconia host lattice, showing oxygen vacancy in the nearest neighbor position (1NN) with the equivalent positions for the oxygen vacancy to sit around the dopant ion labeled (b) Fluorite structure after adding a dopant to the ceria or zirconia host lattice, showing oxygen vacancy in the next nearest neighbor position (2NN)

Many studies have focused on characterizing either anelastic relaxation[31, 76, 82, 141, 154, 188, 208] or dielectric relaxation[30, 59, 75, 96, 183, 209-211] separately in different doped zirconia. The results for 8YSZ are compiled by a variety of techniques from low frequency[83] (10^{-4} Hz) to high frequency[141] (500 kHz) show very similar results for activation energy for both anelastic relaxation and dielectric relaxation to be 1.2 ± 0.2 eV. Furthermore, these studies have also shown that the relaxation time for anelastic relaxation is twice the relaxation time for dielectric relaxation[31, 198].

In this study, the internal friction peaks of 8YSZ were observed under an applied electric field. RUS has been described in more detail in previous sections and will again be used to determine the elastic constants and attenuation, Q^{-1}, of the samples. The changes in Q^{-1} with temperature and frequency ranging from 20 to 500 kHz under

various electric fields are used to characterize anelastic and dielectric relaxation coupling in stabilized zirconia.

6.2 Materials and Methods

The samples used in this study were processed from commercially available 8 mol% Yttria stabilized Zirconia (TOSOH Corp., Japan) powder. Samples were made by uniaxially cold pressing powders to 20 MPa for 10 seconds into 25 x 8 mm^3 cylindrical samples and were then sintered at 1500 °C for 2 hours with 5 °C/min heating and cooling rates. Samples were then cut into 14 x 11 x 2 mm rectangular parallelepipeds for RUS testing. The density of each sample was measured to be above 98% relative density using the Archimedes method according to the modified standard procedure C20-00[166], described in more detail elsewhere [167, 168].

Each sample was initially tested on the commercially available Quasar RUS system with PZT transducers to ensure each sample had no defects from processing. Samples were then placed in the custom built RUS stage[165] for testing up to 700 °C in the ambient air. The high temperature RUS setup uses two 6 inch single crystal alumina rods glued to PZT transducers to transmit ultrasonic vibrations at sweeping frequency and constant amplitude to the sample, and receive signal form the sample. . Each sample was tested in the 20 kHz - 500 kHz frequency range, from 20 °C to 700 °C, in 10 °C temperature increments. Platinum electrodes were then applied to both sides of the samples using a thin layer platinum paste (Fuel Cell Materials, Ohio, USA). A 0.1 mm thick 99.95% pure gold wires (Alfa Aesar, USA) were attached to electrodes. The gold

wires were then connected to C.B.S. Scientific EPS 300 X Power Supply, with the maximum output of to 300 V DC. Samples with the coated electrode where then tested using RUS at extremal electric fields of 0 V/mm, 50 V/mm, 100 V/mm, and 150 V/mm. RUSpec Software from Magnaflux was used to determine the elastic constants at each temperature and electric field, from the collected resonant spectra, as described in more details elsewhere[165]. The attenuation or mechanical damping was determined by measuring the full width at half maximum (FWHM) of selected resonant peaks at every temperature using Fityk software[171] with Pearson 7 peaks models.

The attenuation of the 8YSZ sample with and without the electrode is shown in **Figure 6.2**, an additional attenuation peak is observed in the sample with the electrodes at approximately 130 °C. This peak is solely due to the platinum electrode and thus it will be ignored when analyzing attenuation of 8YSZ in the remainder of this paper.

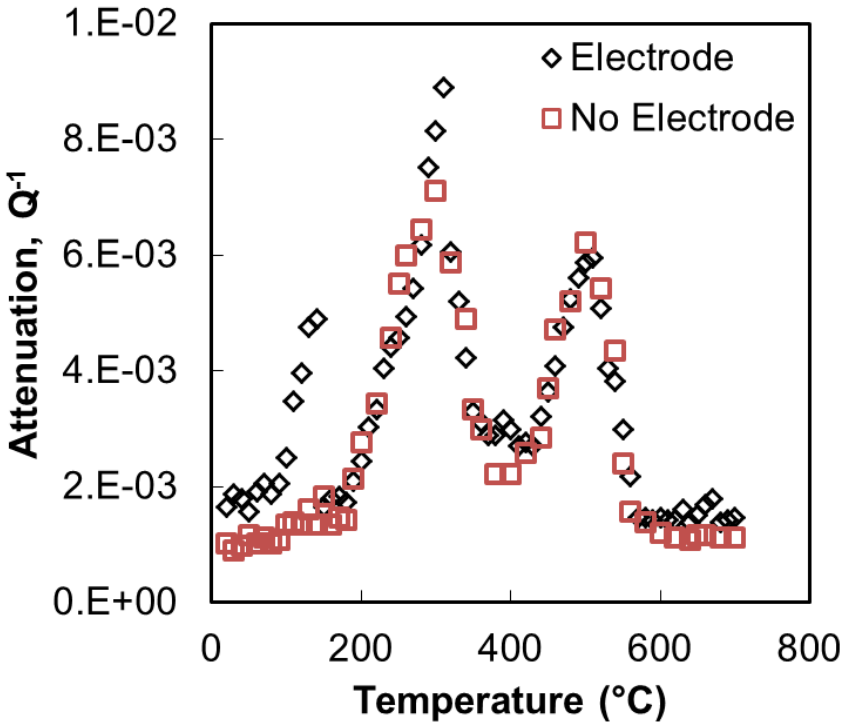

Figure 6.2. The comparison attenuation, Q^{-1}, of 8YSZ sample with and without platinum electrode at different temperatures, without applied electric field. Q^{-1} was determined for resonant peak at 90 kHz.

Anelastic and dielectric relaxation are both frequency dependent processes caused by defect motion during due to either a mechanical or electric field[74, 80]. These processes can be described using an Arrhenius relationship:

$$f = f_0 \exp\left(\frac{-H_r}{kT}\right) \qquad \textbf{(6.5)}$$

where H_r is the activation energy for the relaxation process[81], k is Boltzmann constant, T is the temperature in Kelvin and f_0 is the relaxation frequency. The attenuation of at

least four different resonant peaks was determined to calculate the activation energy as the slope of the Arrhenius plot (lnf vs 1/T).

6.3 Results and Discussion

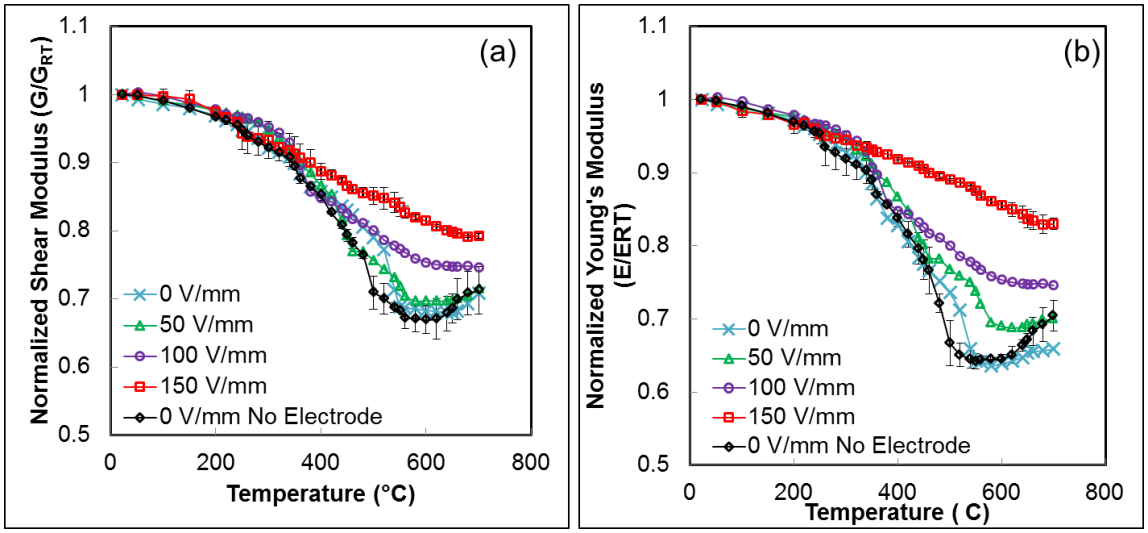

Figure 6.3. Normalized (a) shear (G) modulus and (b) Young's modulus (E) of 8YSZ vs. temperature under the four different electric fields: 0 V/mm, 50 V/mm, 100 V/mm, and 150 V/mm. In addition, elastic moduli of 8YSZ determined using sample without electrodes are also plotted in this figure. As the stronger electrical field is applied, the samples show smaller decrease in the elastic moduli at higher temperatures.

When compared to other typical oxides, 8YSZ shows a large drop in modulus in approximately 200 - 600 °C temperature range, referred to as the "elastic anomaly"[87, 141, 159, 173]. This large decrease in elastic moduli at high temperatures can be detrimental to the operation of SOFCs or other applications. **Figure 6.3** shows the elastic moduli for 8YSZ under different electric fields up to 150 V/mm. At 0 V/mm the platinum electrode has little effect on the elastic moduli. It is clear from **Figure 6.3** that 8YSZ becomes

stiffer with increasing intensity of electric field and elastic anomaly can be barely observed in 200 - 600 °C at the field of 150 V/mm. This observation can be directly related to the reorientation defect complexes as electro-elastic dipoles. In other words, application of elastic field freezes electro-elastic dipoles in one direction and their movement applied external strains becomes more difficult. The latter results in an apparently stiffer material.

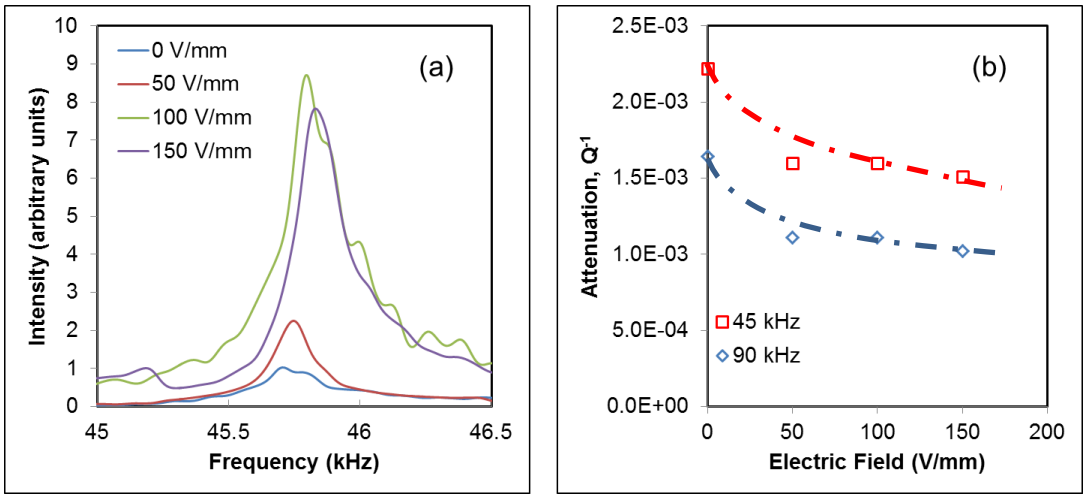

Figure 6.4. (a) The 45 kHz resonant peak normalized to the same height for comparison shows a frequency shift towards higher frequencies and higher intensity of resonant peaks with increasing electric field for the 150 V/mm peak and (b) the attenuation determined as FWHM of the 45 and 90 kHz resonant peaks at room temperature vs. electric field.

The internal friction, Q^{-1}, for resonant peaks at different frequencies is determined by calculating their full width at half maximum (FWHM), as a function of applied electric field. The resonant peak at approximately 45 kHz is shown in **Figure**

6.4a. It can be seen that the peak at 0 V/mm (blue line) is broader than the peaks under an electric field. Changes of internal friction with applied electric field at room temperature for resonant peaks at 45 and 90 kHz are shown in **Figure 6.4b.**

The attenuation curves for the entire temperature range are shown **Figure 6.5** for the resonant peak at 90 kHz at under different electric fields. The curves for 0 V/mm (**Figure 6.5a**) were done at a much finer temperature steps of every 10 °C. In those curves, a sharp Q^{-1} peak can be observed at approximately 130 °C that can be attributed to the platinum electrode. The attenuation curves for 50 V/mm (**Figure 6.5b**) and 100 V/mm (**Figure 6.5c**) do not show the platinum peaks since the temperature step was too large to detect that sharp peak at around 130 °C. The internal friction curves for 0 V/mm, 50 V/mm and 100 V/mm all show two major peaks that were further deconvoluted into the six peaks, following the deconvolution method discussed in Section 5. Here is can be seen that although the peaks remain in the same approximate place, the strength of some of the peaks decreases as the electric field is applied. The peak at approximately 300 °C for both 0 V/mm and 50 V/mm has a strength of approximately 0.65, however when the field is increased to 100 V/mm, the relaxation strength decreases to approximately 0.3.

The activation energies for each attenuation peak were calculated at different electric fields and the results are given in **Table 6.1.** Results in **Table 6.1** shows that activation energy for different relaxation mechanisms is not affected by electric field, i.e. it remains the same with the error margin with increasing electric field. Therefore, application of electric field does not change activation energy of different relaxation

processes, but it only changes amount of dipoles that can reorient with the ultrasonic strain.

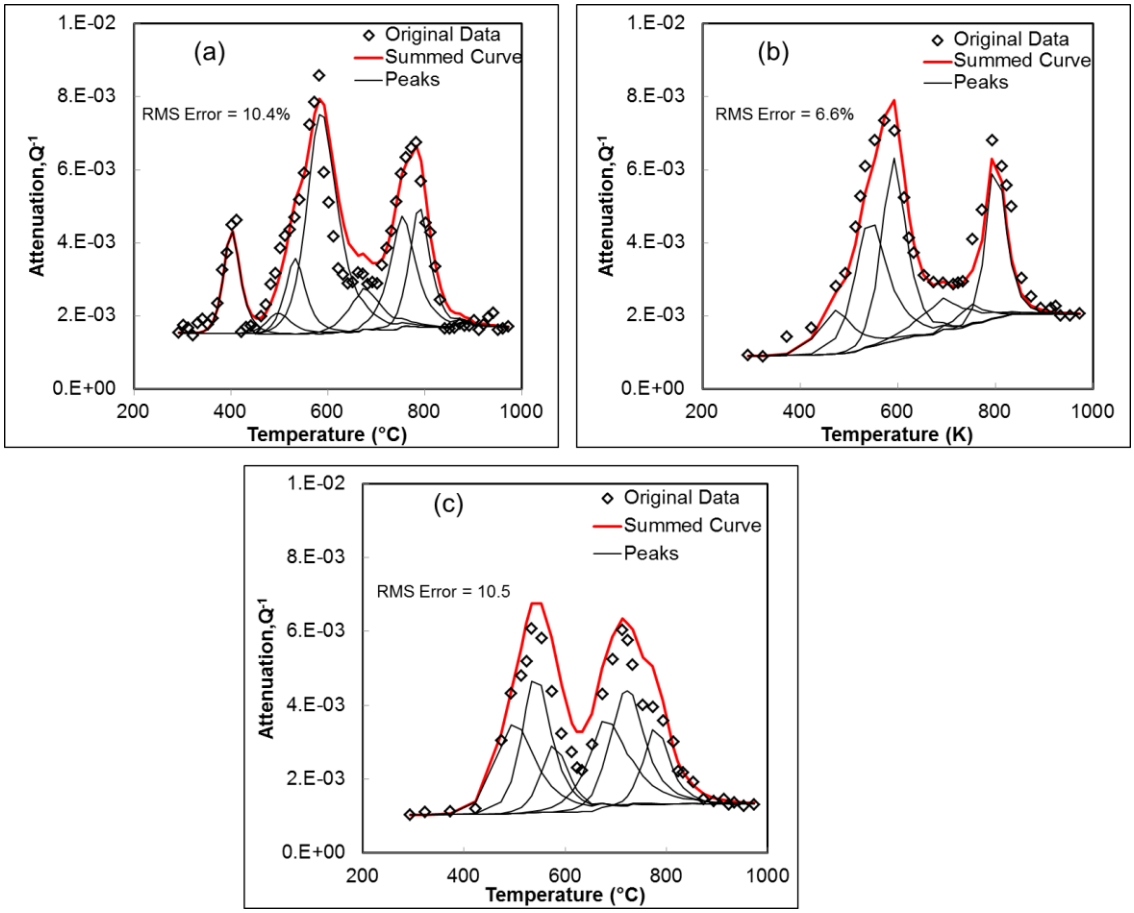

Figure 6.5. Attenuation v.s. temperature for resonant peak at 90 kHz under electric field of (a) 0 V/mm, (b) 50 V/mm, and (c) 100 V/mm; the 0 V/mm had a finer step size of 10 ºC and reveals an additional peak at 130 kHz corresponding to the platinum electrode. Results of deconvolution of relaxation spectra using six independent relaxation curves (black lines) are shown together with the cumulative relaxation curves (red lines) obtained by summing deconvoluted ones.

Table 6.1. The activation energy for the six relaxation peaks at different electric fields. There is good agreement between the temperatures ranges that the peaks occur and the activation energies for the first three fields.

	200-230 C	250-290 C	300-330 C	400-420 C	460-500 C	500-530 C
0 V/mm	0.59 ± 0.138	0.98 ± 0.123	1.25 ± 0.317	0.98 ± 0.166	1.92 ± 0.219	2.44 ± 0.437
50 V/mm	0.61	0.88	1.38	0.97	1.88	3.20
100 V/mm	0.63	1.01	1.23	1.10	1.55	2.34

6.4 Conclusions

Resonant Ultrasound Spectroscopy (RUS) results are present for 8 mol% yttria stabilized zirconia (8YSZ) under a constant electric field. As reported previously, a large drop in shear and young's moduli was observed with corresponding internal friction peaks under no electric field. However, application of electric field results in smaller drop of elastic properties in 200-600 °C temperature range. The internal friction vs. temperature curves peaks obtained from RUS spectra for the resonant peaks at different frequencies were further deconvoluted assuming six independent Single Debye relaxation mechanisms, and activation energies for each of them were determined. The activation energies for the mechanisms remained approximately the same for each peak as the field increased to 100 V/mm. results presented here suggest that application of the electric field freezes out electro-elastic dipoles in 8YSZ, making it apparently stiffer at higher electric field due more difficult reorientation of those dipoles with the applied stress.

7. CONCLUSIONS AND FUTURE WORK

In this study, the elastic properties and anelastic relaxation of doped zirconia and ceria were studied with a custom built High Temperature Resonant Ultrasound Spectroscopy (HT-RUS) setup. The results can be summarized as follows:

1. A high temperature resonant ultrasound spectroscopy (HT-RUS) tripod setup was developed for measurements up to 1300 °C that is capable of working in different environments. The specially designed buffer rods and transducer jackets keep the PZT transducers at temperatures below their operation limit. The resonant spectra measured using the HT-RUS setup are in excellent agreement with those from commercially available room temperature setups and the calculated Young's and shear modulus of a variety of materials are in good agreement with previously published results.
2. Using the developed HT-RUS setup, elastic properties and anelastic relaxation of stabilized zirconia samples (8 mol% and 10 mol% yttria stabilized zirconia (8YSZ and 10YSZ), gadolinia stabilized zirconia (GSZ), and 10mol% Scandia – 1mol% Ceria stabilized Zirconia (SCZ)) were studied up to 1000 °C, in the ambient air. The large decrease in Young's and shear modulus corresponds to two large mechanical damping (Q^{-1}) peaks observe in 200-600 °C temperature range, and they can be explained by anelastic relaxation mechanisms by hopping of and local order of oxygen vacancies. The mechanical damping peaks of 8YSZ, and 10YSZ were compared to DMA results on the Arrhenius type plots of relaxation frequency vs. temperature of the maximum internal friction at

particular frequency, and good agreement was found between the two sets of data despite the large difference in the frequency range between two methods. In the case of SCZ, a good agreement between RUS and DMA results was achieved only for the first relaxation peak, because the second peak was not clearly detected in DMA. More importantly, relaxation peak previously observed in DMA of SCZ due to stress induced phase transformation from cubic to rhombohedral was not observed in RUS results, while that one attributed to the frequency independent rhombohedral to cubic transformation was observed in both RUS and DMA.

3. Ceria doped with trivalent dopants (Gd^{3+}, Y^{3+}, Sm^{3+} and La^{3+}) were studied with RUS up to 1000 °C to determine the effect of dopant radius on the activation energy for anelastic relaxation. Reduced ceria samples were also studied, and the reduced Ce^{3+} acted like a trivalent dopant in the system. The elastic moduli were calculated and all samples showed a monotonic decrease in moduli across the entire temperature range. Two internal friction peaks were observed in each sample and the corresponding activation energies were calculated. These energies were plotted to compare the effect of dopant ion radius to the difference between the dopant radius and either the host radius or the critical ionic radius which is based on minimizing the lattice strain. A slight trend was observed when compared to the difference between the dopant ionic radius and the critical ionic radius where the activation energy initially increase then decrease.

4. The RUS results collected for 8YSZ were further analyzed to elucidate the number of relaxation mechanisms occurring as a result of the applied stress field. It was found that six peaks minimize the RMS error between experimental results and reconstructed mechanical loss spectra, when assuming that each mechanism can be described using single Debye relaxation mechanism. With the six peak model, the two major peaks corresponding to the previously assumed two peak model can clearly be observed and have similar activation energies to that determined form the model based on only two relaxation peaks.
5. HT-RUS was used to study 8YSZ under different electric field of constant voltage. It was found that the drop of modulus in 200-600 °C temperature range was less pronounced while the internal friction peaks showed a suppression of some peaks in favor of others, as the magnitude of electric field increases. The mechanical loss peaks were deconvoluted into six relaxation peaks according to the previous model and the activation energies were determined with good agreement between 0 V/mm, 50 V/mm and 100 V/mm.

To continue study into relaxation mechanisms in doped zirconia and ceria, the following questions should be addressed:

1. *How many relaxation mechanisms and what are the relaxation mechanisms occurring in doped zirconia and ceria?* This work studied only limited number of the possible relaxation mechanisms, but the actual number could be a different amount. In addition, recent computation studies suggest a wide array of possible

oxygen vacancy motions around dopant that vary depending on the dopant radius compared to the host lattice, hopping direction, etc. Further studies, particularly on single crystal samples with different orientations should be carried out to determine the number of types of defect motion.

2. *What is the effect of ageing on elastic and dialectic relaxation in doped oxides?* It is has been established by now that defect structure and their ordering changes as a result if long term ageing of doped oxides. However, it is not clear what the effect of stress and electric field on this process and how it would affect relaxation due to oxygen vacancy hopping.
3. *Can we build molecular dynamics model that would help understanding anelastic relaxation and dielectric relaxation of doped oxides with different confirmations of defect clusters?*
4. *What is the optimal electric field voltage to suppress defect motion in 8YSZ?* This worked studied four different electric fields, 0, 50, 100 and 150 V/mm and saw a suppression of some peaks before a sudden shift in the internal friction peaks. More refined measurements at smaller electric field increments should be performed. In addition, to understand the exact relaxation mechanism that is being suppressed, single crystal 8YSZ of different orientations should be studied.
5. *Can this mechanism be observed in other oxides having cubic structure?* In addition to doped ceria and zirconia, other materials such as uranium oxide (UO_2), thorium oxide (ThO_2) and hafnium oxide (HfO_2) have a stable cubic fluorite structure at room temperature when stabilized with trivalent dopants.

Some initial studies have begun investigating the conductivities and defect formation of within these doped oxides. Further investigation of their mechanical properties and their mechanical damping should be performed.

REFERENCES

1. S. P. S. Badwal, "Zirconia-based solid electrolytes - microstructure, stability and ionic-conductivity," *Solid State Ion.*, 52[1-3] 23-32 (1992).

2. H. Inaba and H. Tagawa, "Ceria-based solid electrolytes - review," *Solid State Ion.*, 83[1-2] 1-16 (1996).

3. T. Inoue, T. Setoguchi, K. Eguchi, and H. Arai, "Study of a solid oxide fuel-cell with a ceria-based solid electrolyte," *Solid State Ion.*, 35[3-4] 285-91 (1989).

4. S. Kim, S. Yamaguchi, and J. A. Elliott, "Solid-state ionics in the 21st century: Current status and future prospects," *MRS Bull.*, 34[12] 900-06 (2009).

5. P. Knauth and H. L. Tuller, "Solid-state ionics: Roots, status, and future prospects," *Journal of the American Ceramic Society*, 85[7] 1654-80 (2002).

6. N. M. Sammes and Z. H. Cai, "Ionic conductivity of ceria/yttria stabilized zirconia electrolyte materials," *Solid State Ion.*, 100[1-2] 39-44 (1997).

7. A. Tarancon, "Strategies for lowering solid oxide fuel cells operating temperature," *Energies*, 2[4] 1130-50 (2009).

8. O. Yamamoto, Y. Arachi, H. Sakai, Y. Takeda, N. Imanishi, Y. Mizutani, M. Kawai, and Y. Nakamura, "Zirconia based oxide ion conductors for solid oxide fuel cells," *Ionics*, 4[5-6] 403-08 (1998).

9. B. C. H. Steele, "Ceramic ion conducting membranes," *Curr. Opin. Solid State Mat. Sci.*, 1[5] 684-91 (1996).

10. N. Q. Minh, "Ceramic fuel cells," *Journal of the American Ceramic Society*, 76[3] 563-88 (1993).

11. H. L. Tuller, "Defect engineering: Design tools for solid state electrochemical devices," *Electrochim. Acta,* 48[20-22] 2879-87 (2003).

12. L. J. Gauckler, D. Beckel, B. E. Buergler, E. Jud, U. R. Muecke, M. Prestat, J. L. M. Rupp, and J. Richter, "Solid oxide fuel cells: Systems and materials," *Chimia,* 58[12] 837-50 (2004).

13. G. Stapper, M. Bernasconi, N. Nicoloso, and M. Parrinello, "Ab initio study of structural and electronic properties of yttria-stabilized cubic zirconia," *Phys. Rev. B,* 59[2] 797-810 (1999).

14. R. H. J. Hannink, P. M. Kelly, and B. C. Muddle, "Transformation toughening in zirconia-containing ceramics," *Journal of the American Ceramic Society,* 83[3] 461-87 (2000).

15. X. M. Zeng, A. Lai, C. L. Gan, and C. A. Schuh, "Crystal orientation dependence of the stress-induced martensitic transformation in zirconia-based shape memory ceramics," *Acta Mater.,* 116 124-35 (2016).

16. A. Lai, Z. H. Du, C. L. Gan, and C. A. Schuh, "Shape memory and superelastic ceramics at small scales," *Science,* 341[6153] 1505-08 (2013).

17. D. W. Strickler and W. G. Carlson, "Electrical conductivity in zro2-rich region of several m2o3-zro2 systems," *Journal of the American Ceramic Society,* 48[6] 286-+ (1965).

18. T. Y. Tien and E. C. Subbarao, "X-ray and electrical conductivity study of fluorite phase in system zro2-cao," *J. Chem. Phys.,* 39[4] 1041-& (1963).

19. R. C. Garvie, "Cubic field in system cao-zro2," *Journal of the American Ceramic Society*, 51[10] 553-& (1968).

20. C. F. Grain, "Phase relations in zro2-mgo system," *Journal of the American Ceramic Society*, 50[6] 288-& (1967).

21. E. N. S. Muccillo and M. Kleitz, "Impedance spectroscopy of mg-partially stabilized zirconia and cubic phase decomposition," *J. Eur. Ceram. Soc.*, 16[4] 453-65 (1996).

22. D. N. Argyriou, M. M. Elcombe, and A. C. Larson, "A neutron scattering investigation of cubic stabilised zirconia (csz) .1. The average structure of y-csz," *J. Phys. Chem. Solids*, 57[2] 183-93 (1996).

23. J. R. Brandon and R. Taylor, "Phase-stability of zirconia-based thermal barrier coatings .1. Zirconia yttria alloys," *Surface & Coatings Technology*, 46[1] 75-90 (1991).

24. H. P. Ding, A. V. Virkar, and F. Liu, "Defect configuration and phase stability of cubic versus tetragonal yttria-stabilized zirconia," *Solid State Ion.*, 215 16-23 (2012).

25. P. Duwez, F. H. Brown, and F. Odell, "The zirconia-yttria system," *J. Electrochem. Soc.*, 98[9] 356-62 (1951).

26. R. Krishnamurthy, Y. G. Yoon, D. J. Srolovitz, and R. Car, "Oxygen diffusion in yttria-stabilized zirconia: A new simulation model," *Journal of the American Ceramic Society*, 87[10] 1821-30 (2004).

27. K. Eguchi, T. Setoguchi, T. Inoue, and H. Arai, "Electrical-properties of ceria-based oxides and their application to solid oxide fuel-cells," *Solid State Ion.*, 52[1-3] 165-72 (1992).

28. S. L. Reis, E. C. C. Souza, and E. N. S. Muccillo, "Solid solution formation, densification and ionic conductivity of gd- and sm-doped ceria," *Solid State Ion.*, 192[1] 172-75 (2011).

29. D. A. Andersson, S. I. Simak, N. V. Skorodumova, I. A. Abrikosov, and B. Johansson, "Optimization of ionic conductivity in doped ceria," *Proceedings of the National Academy of Sciences of the United States of America,* 103[10] 3518-21 (2006).

30. H. Yamamura, S. Takeda, and K. Kakinuma, "Dielectric relaxations in the ce1-xsmxo2-delta system," *J. Ceram. Soc. Jpn.,* 115[1340] 264-68 (2007).

31. R. Gerhardt, W. K. Lee, and A. S. Nowick, "Anelastic and dielectric relaxation of scandia doped ceria," *J. Phys. Chem. Solids*, 48[6] 563-69 (1987).

32. B. C. H. Steele, "Appraisal of ce1-ygdyo2-y/2 electrolytes for it-sofc operation at 500 degrees c," *Solid State Ion.*, 129[1-4] 95-110 (2000).

33. B. Dalslet, P. Blennow, P. V. Hendriksen, N. Bonanos, D. Lybye, and M. Mogensen, "Assessment of doped ceria as electrolyte," *J. Solid State Electrochem.*, 10[8] 547-61 (2006).

34. M. Yashima and T. Takizawa, "Atomic displacement parameters of ceria doped with rare-earth oxide ce0.8r0.2o1.9 (r = la, nd, sm, gd, y, and yb) and correlation with oxide-ion conductivity," *J. Phys. Chem. C,* 114[5] 2385-92 (2010).

35. V. P. Gorelov, V. B. Balakireva, I. Y. Yaroslavtsev, V. A. Kazantsev, and E. G. Vaganov, "Conductivity and thermal expansion of the ce0.8gd0.2o1.9 solid electrolyte in the oxidizing and reducing atmospheres," *Russ. J. Electrochem.*, 43[8] 888-93 (2007).

36. D. Y. Wang and A. S. Nowick, "Dielectric-relaxation in yttria-doped ceria solid solutions," *J. Phys. Chem. Solids,* 44[7] 639-46 (1983).

37. K. Sato, K. Suzuki, K. Yashiro, T. Kawada, H. Yugami, T. Hashida, A. Atkinson, and J. Mizusaki, "Effect of y2o3 addition on the conductivity and elastic modulus of (ceo2)(1-x)(yo1.5)(x)," *Solid State Ion.,* 180[20-22] 1220-25 (2009).

38. K. P. Padmasree, R. A. Montalvo-Lozano, S. M. Montemayor, and A. F. Fuentes, "Electrical conduction and dielectric relaxation process in ce0.8y0.2o1.9 electrolyte system," *J. Alloy. Compd.,* 509[34] 8584-89 (2011).

39. J. H. Lee, S. M. Yoon, B. K. Kim, J. Kim, H. W. Lee, and H. S. Song, "Electrical conductivity and defect structure of yttria-doped ceria-stabilized zirconia," *Solid State Ion.*, 144[1-2] 175-84 (2001).

40. J. M. Solomon, V. Alexandrov, B. Sadigh, A. Navrotsky, and M. Asta, "Computational study of the energetics and defect clustering tendencies for y- and la-doped uo2," *Acta Mater.*, 78 282-89 (2014).

41. L. Minervini, M. O. Zacate, and R. W. Grimes, "Defect cluster formation in m2o3-doped ceo2," *Solid State Ion.*, 116[3-4] 339-49 (1999).

42. K. Ahn, Y. C. Chung, K. J. Yoon, J. W. Son, B. K. Kim, H. W. Lee, and J. H. Lee, "Lattice-strain effect on oxygen vacancy formation in gadolinium-doped ceria," *J. Electroceram.,* 32[1] 72-77 (2014).

43. M. Mogensen, N. M. Sammes, and G. A. Tompsett, "Physical, chemical and electrochemical properties of pure and doped ceria," *Solid State Ion.,* 129[1-4] 63-94 (2000).

44. R. Gerhardtanderson and A. S. Nowick, "Ionic conductivity of ceo2 with trivalent dopants of different ionic radii," *Solid State Ion.,* 5[OCT] (1981).

45. C. R. A. Catlow, "Transport in doped fluorite oxides," *Solid State Ion.,* 12[MAR] 67-73 (1984).

46. D. J. Kim, "Lattice-parameters, ionic conductivities, and solubility limits in fluorite-structure hf-4+o2, zr-4+o2, ce-4+o2, th-4+o2, v-4+o2 oxide solid-solutions," *Journal of the American Ceramic Society,* 72[8] 1415-21 (1989).

47. S. J. Hong and A. V. Virkar, "Lattice-parameters and densities of rare-earth-oxide doped ceria electrolytes," *Journal of the American Ceramic Society,* 78[2] 433-39 (1995).

48. G. B. Balazs and R. S. Glass, "Ac-impedance studies of rare-earth-oxide doped ceria," *Solid State Ion.,* 76[1-2] 155-62 (1995).

49. H. Yokokawa, N. Sakai, T. Horita, K. Yamaji, and M. E. Brito, "Electrolytes for solid-oxide fuel cells," *MRS Bull.,* 30[8] 591-95 (2005).

50. Y. Wang, K. L. Duncan, E. D. Wachsman, and F. Ebrahimi, "Effects of reduction treatment on fracture properties of cerium oxide," *Journal of the American Ceramic Society*, 90[12] 3908-14 (2007).

51. M. A. Panhans and R. N. Blumenthal, "A thermodynamic and electrical conductivity study of nonstoichiometric cerium dioxide," *Solid State Ion.*, 60[4] 279-98 (1993).

52. Z. P. Li, T. Mori, F. Ye, D. R. Ou, G. J. Auchterlonie, J. Zou, and J. Drennan, "Cerium-reduction-induced defects clustering, ordering, and associated microstructure evolution in yttrium-doped ceria," *J. Phys. Chem. C*, 116[9] 5435-43 (2012).

53. H. Yahiro, K. Eguchi, and H. Arai, "Electrical-properties and reducibilities of ceria rare earth oxide systems and their application to solid oxide fuel-cell," *Solid State Ion.*, 36[1-2] 71-75 (1989).

54. D. Schneider, M. Godickemeier, and L. J. Gauckler, "Nonstoichiometry and defect chemistry of ceria solid solutions," *J. Electroceram.*, 1[2] 165-72 (1997).

55. F. A. Kroger, "The chemistry of imperfect crystals.″ North-Holland Pub.: Amsterdam, (1964).

56. M. Weller, "Anelastic relaxation of point defects in cubic crystals," *J. Phys. IV*, 6[C8] 63-72 (1996).

57. J. B. Wachtman, "Mechanical and electrical relaxation in tho2 containing cao," *Physical Review*, 131[2] 517-& (1963).

58. A. S. Nowick, "The combining of dielectric and anelastic relaxation measurements in the study of point-defects in insulating ceramics," *Journal De Physique,* 46[C-10] 507-11 (1985).

59. A. S. Nowick and W. R. Heller, "Dielectric and anelastic relaxation of crystals containing point defects," *Adv. Phys.*, 14[54] 101-& (1965).

60. F. Pietrucci, M. Bernasconi, A. Laio, and M. Parrinello, "Vacancy-vacancy interaction and oxygen diffusion in stabilized cubic zro(2) from first principles," *Phys. Rev. B,* 78[9] 7 (2008).

61. A. Kushima and B. Yildiz, "Oxygen ion diffusivity in strained yttria stabilized zirconia: Where is the fastest strain?," *Journal of Materials Chemistry,* 20[23] 4809-19 (2010).

62. B. W. Veal, A. G. McKale, A. P. Paulikas, S. J. Rothman, and L. J. Nowicki, "Exafs study of yttria stabilized cubic zirconia," *Physica B & C,* 150[1-2] 234-40 (1988).

63. C. R. A. Catlow, A. V. Chadwick, G. N. Greaves, and L. M. Moroney, "Exafs study of yttria-stabilized zirconia," *Journal of the American Ceramic Society,* 69[3] 272-77 (1986).

64. P. Li, I. W. Chen, and J. E. Pennerhahn, "X-ray-absorption studies of zirconia polymorphs .1. Characteristic local structures," *Phys. Rev. B,* 48[14] 10063-73 (1993).

65. D. Steele and B. E. F. Fender, "Structure of cubic zro2-yo1.5 solid-solutions by neutron-scattering," *Journal of Physics C-Solid State Physics,* 7[1] 1-11 (1974).

66. K. Kawata, H. Maekawa, T. Nemoto, and T. Yamamura, "Local structure analysis of ysz by y-89 mas-nmr," *Solid State Ion.*, 177[19-25] 1687-90 (2006).

67. A. Bogicevic, C. Wolverton, G. M. Crosbie, and E. B. Stechel, "Defect ordering in aliovalently doped cubic zirconia from first principles," *Phys. Rev. B,* 64[1] 14 (2001).

68. A. Bogicevic and C. Wolverton, "Nature and strength of defect interactions in cubic stabilized zirconia," *Phys. Rev. B,* 67[2] 13 (2003).

69. M. S. Khan, M. S. Islam, and D. R. Bates, "Cation doping and oxygen diffusion in zirconia: A combined atomistic simulation and molecular dynamics study," *Journal of Materials Chemistry,* 8[10] 2299-307 (1998).

70. M. Nakayama and M. Martin, "First-principles study on defect chemistry and migration of oxide ions in ceria doped with rare-earth cations," *Physical Chemistry Chemical Physics,* 11[17] 3241-49 (2009).

71. A. Kossoy, A. I. Frenkel, Q. Wang, E. Wachtel, and I. Lubomirsky, "Local structure and strain-induced distortion in ce0.8gd0.2o1.9," *Advanced Materials,* 22[14] 1659-+ (2010).

72. H. Inaba, R. Sagawa, H. Hayashi, and K. Kawamura, "Molecular dynamics simulation of gadolinia-doped ceria," *Solid State Ion.*, 122[1-4] 95-103 (1999).

73. M. P. Anderson and A. S. Nowick, "Relaxation peaks produced by defect complexes in cerium dioxide doped with trivalent cations," *Journal De Physique,* 42[NC5] (1981).

74. R. G. Breckenridge, "Low frequency dispersion in ionic crystals," *J. Chem. Phys.*, 16[10] 959-67 (1948).

75. S. Komine and F. Munakata, "Dielectric relaxation analysis for 8 mol% ysz single crystal," *J. Mater. Sci.*, 40[15] 3887-90 (2005).

76. M. Weller and H. Schubert, "Internal-friction, dielectric loss, and ionic-conductivity of tetragonal zro2-3-percent y2o3 (y-tzp)," *Journal of the American Ceramic Society*, 69[7] 573-77 (1986).

77. G. M. Rignanese, F. Detraux, X. Gonze, and A. Pasquarello, "First-principles study of dynamical and dielectric properties of tetragonal zirconia," *Physical Review B*, 64[13] 7 (2001).

78. M. Weller, R. Herzog, M. Kilo, G. Borchardt, S. Weber, and S. Scherrer, "Oxygen mobility in yttria-doped zirconia studied by internal friction, electrical conductivity and tracer diffusion experiments," *Solid State Ion.*, 175[1-4] 409-13 (2004).

79. J. Kondoh, S. Kikuchi, Y. Tomii, and Y. Ito, "Effect of aging on yttria-stabilized zirconia iii. A study of the effect of local structures on conductivity," *J. Electrochem. Soc.*, 145[5] 1550-60 (1998).

80. A. S. Nowick and B. S. Berry, "Anelastic relaxation in crystalline solids." Academic Press, Inc.: New York, (1972).

81. R. Schaller, G. Fantozzi, and G. Gremaud, "Mechanical spectroscopy q-1 2001: With applications to materials science." Trans Tech Publications Limited: Zuerich-Uetikon, Switzerland, (2001).

82. P. P. Gao, E. Lara-Curzio, R. Trejo, and M. Radovic, "Dynamic mechanical analysis of phase transformations and anelastic relaxation in stabilized zirconias," *J. Electrochem. Soc.*, 162[1] F14-F22 (2015).

83. A. Lakki, R. Herzog, M. Weller, H. Schubert, C. Reetz, O. Gorke, M. Kilo, and G. Borchardt, "Mechanical loss, creep, diffusion and ionic conductivity of zro2-8 mol%y2o3 polycrystals," *J. Eur. Ceram. Soc.*, 20[3] 285-96 (2000).

84. A. Atkinson and A. Selcuk, "Mechanical behaviour of ceramic oxygen ion-conducting membranes," *Solid State Ion.*, 134[1-2] 59-66 (2000).

85. J. Laurencin, G. Delette, F. Lefebvre-Joud, and A. Dupeux, "A numerical tool to estimate sofc mechanical degradation: Case of the planar cell configuration," *J. Eur. Ceram. Soc.*, 28[9] 1857-69 (2008).

86. T. Kushi, K. Sato, A. Unemoto, S. Hashimoto, K. Amezawa, and T. Kawada, "Elastic modulus and internal friction of sofc electrolytes at high temperatures under controlled atmospheres," *J. Power Sources*, 196[19] 7989-93 (2011).

87. M. Radovic, E. Lara-Curzio, and G. Nelson, "Fracture toughness and slow crack growth behavior of ni-ysz and ysz as a function of porosity and temperature," pp. 373-81 in 30th International Conference and Exposition on Advanced Ceramics and Composites. Vol. 27.

88. E. Ivers-Tiffee, A. Weber, and D. Herbstritt, "Materials and technologies for sofc-components," *J. Eur. Ceram. Soc.*, 21[10-11] 1805-11 (2001).

89. A. Atkinson and A. Selcuk, "Mechanical properties of ceramic materials for solid oxide fuel cells," *Proceedings of the Fifth International Symposium on Solid Oxide Fuel Cells (Sofc-V)*, 97[40] 671-80 (1997).

90. M. Belmonte, "Advanced ceramic materials for high temperature applications," *Adv. Eng. Mater.*, 8[8] 693-703 (2006).

91. P. Holtappels, U. Vogt, and T. Graule, "Ceramic materials for advanced solid oxide fuel cells," *Adv. Eng. Mater.*, 7[5] 292-302 (2005).

92. J. W. Fergus, "Electrolytes for solid oxide fuel cells," *J. Power Sources*, 162[1] 30-40 (2006).

93. W. Araki and Y. Arai, "Oxygen mobility under mechanical stress," *Solid Oxide Fuel Cells 11 (Sofc-Xi)*, 25[2] 1593-98 (2009).

94. W. Araki, Y. Imai, and T. Adachi, "Mechanical stress effect on oxygen ion mobility in 8 mol% yttria-stabilized zirconia electrolyte," *J. Eur. Ceram. Soc.*, 29[11] 2275-79 (2009).

95. L. Jin, Q. H. Yu, A. Rauf, and C. G. Zhou, "Elastic, electronic and thermal properties of ysz from first principles," *Solid State Sciences*, 14[1] 106-10 (2012).

96. Y. Liu, "Dielectric and electrical properties of gadolinia doped ceria," *J. Alloy. Compd.*, 479[1-2] 769-71 (2009).

97. S. Giraud and J. Canel, "Young's modulus of some sofcs materials as a function of temperature," *J. Eur. Ceram. Soc.*, 28[1] 77-83 (2008).

98. N. E. Dowling, "Mechanical behavior of materials." Prentice Hall: New Jersey, (1998).

99. A. Migliori and J. D. Maynard, "Implementation of a modern resonant ultrasound spectroscopy system for the measurement of the elastic moduli of small solid specimens," *Review of Scientific Instruments,* 76[12] 7 (2005).

100. R. G. Leisure and F. A. Willis, "Resonant ultrasound spectroscopy," *J. Phys.-Condes. Matter,* 9[28] 6001-29 (1997).

101. A. Migliori, J. L. Sarrao, W. M. Visscher, T. M. Bell, M. Lei, Z. Fisk, and R. G. Leisure, "Resonant ultrasound spectroscopic techniques for measurement of the elastic modulus of solids," *Physica B,* 183[1-2] 1-24 (1993).

102. A. M. a. J. L. Sarrao, "Resonant ultrasound spectroscopy: Applications to physics, materials measurements, and nondestructive evaluation.″ Wiley: New York, (1997).

103. A. Migliori and T. W. Darling, "Resonant ultrasound spectroscopy for materials studies and non-destructive testing," *Ultrasonics,* 34[2-5] 473-76 (1996).

104. R. G. Leisure, K. Foster, J. E. Hightower, and D. S. Agosta, "Internal friction studies by resonant ultrasound spectroscopy," *Mater. Sci. Eng. A-Struct. Mater. Prop. Microstruct. Process.,* 370[1-2] 34-40 (2004).

105. K. Foster, R. G. Leisure, and A. V. Skripov, "Ultrasonic evidence for strong isotope effects on the local motion of h(d) in tav2h(d)(x)," *Phys. Rev. B,* 64[21] art. no.-214302 (2001).

106. F. M. Mazzolai, A. Biscarini, B. Coluzzi, G. Mazzolai, E. Villa, and A. Tuissi, "Low-frequency internal friction of hydrogen-free and hydrogen-doped niti alloys," *Acta Mater.,* 55[13] 4243-52 (2007).

107. A. V. Granato and K. Lucke, "Temperature-dependence of amplitude-dependent dislocation damping," *Journal of Applied Physics,* 52[12] 7136-42 (1981).

108. R. J. Harrison, S. A. T. Redfern, and E. K. H. Salje, "Dynamical excitation and anelastic relaxation of ferroelastic domain walls in laalo3," *Phys. Rev. B,* 69[14] 10 (2004).

109. P. E. Armstrong, "Measurement of mechanical properties, techniques of metals research," Vol. 5. Wiley: New York, (1971).

110. P. J. Shull, "Nondestructive evaluation: Theory, techniques, and applications." Marcel Dekker: New York, NY, (2002).

111. K. Flynn and M. Radovic, "Evaluation of defects in materials using resonant ultrasound spectroscopy," *J. Mater. Sci.,* 46[8] 2548-56 (2011).

112. R. B. Schwarz and J. F. Vuorinen, "Resonant ultrasound spectroscopy: Applications, current status and limitations," *J. Alloy. Compd.,* 310 243-50 (2000).

113. M. Radovic, E. Lara-Curzio, and L. Riester, "Comparison of different experimental techniques for determination of elastic properties of solids," *Mater. Sci. Eng. A-Struct. Mater. Prop. Microstruct. Process.,* 368[1-2] 56-70 (2004).

114. J. Maynard, "Resonant ultrasound spectroscopy," *Physics Today,* 49[1] 26-31 (1996).

115. B. J. Zadler, J. H. L. Le Rousseau, J. A. Scales, and M. L. Smith, "Resonant ultrasound spectroscopy: Theory and application," *Geophysical Journal International,* 156[1] 154-69 (2004).

116. W. M. Visscher, A. Migliori, T. M. Bell, and R. A. Reinert, "On the normal-modes of free-vibration of inhomogeneous and anisotropic elastic objects," *Journal of the Acoustical Society of America*, 90[4] 2154-62 (1991).

117. H. Ekstein and T. Schiffman, "Free vibrations of isotropic cubes and nearly cubic parallelepipeds," *Journal of Applied Physics*, 27[4] 405-12 (1956).

118. R. Holland, "Resonant properties of piezoelectric ceramic rectangular parallelepipeds," *Journal of the Acoustical Society of America*, 43[5] 988-& (1968).

119. P. Heyliger, A. Jilani, H. Ledbetter, R. G. Leisure, and C. L. Wang, "Elastic constants of isotropic cylinders using resonant ultrasound," *Journal of the Acoustical Society of America*, 94[3] 1482-87 (1993).

120. E. Mochizuki, "Sphere-resonance method to determine elastic constants of crystal," *Journal of Applied Physics*, 63[12] 5668-73 (1988).

121. O. Heczko, J. Kopecek, D. Majtas, and M. Landa, "Magnetic and magnetoelastic properties of ni-mn-ga - do they need a revision?," in Joint European Magnetic Symposia (JEMS). Vol. 303, *Journal of Physics Conference Series*. I. P. Jagiellonian Univ, U. Jagiellonian, and I. P. P. C. R. Acad Sci Czech Republic. BRISTOL, (2011).

122. O. Heczko, H. Seiner, P. Sedlak, J. Kopecek, V. Kopecky, and M. Landa, "Resonant ultrasound spectroscopy - a tool to probe magneto-elastic properties of ferromagnetic shape memory alloys," *Eur. Phys. J. B*, 86[2] 5 (2013).

123. J. Schiemer, D. O'Flynn, G. Balakrishnan, and M. A. Carpenter, "Strain coupling in multiferroic phase transitions of samarium yttrium manganite sm0.6y0.4mno3," *Phys. Rev. B,* 88[5] 6 (2013).

124. J. A. Schiemer, R. L. Withers, Y. Liu, and M. A. Carpenter, "Ca-doping of bifeo3: The role of strain in determining coupling between ferroelectric displacements, magnetic moments, octahedral tilting, and oxygen-vacancy ordering," *Chem. Mat.,* 25[21] 4436-46 (2013).

125. V. F. Correa, W. E. Okraku, J. B. Betts, A. Migliori, J. L. Sarrao, and A. H. Lacerda, "High-magnetic-field thermal expansion and elastic properties of cerhin(5)," *Phys. Rev. B,* 72[1] 4 (2005).

126. T. W. Darling, A. Migliori, E. G. Moshopoulou, S. A. Trugman, J. J. Neumeier, J. L. Sarrao, A. R. Bishop, and J. D. Thompson, "Measurement of the elastic tensor of a single crystal of la0.83sr0.17mno3 and its response to magnetic fields," *Phys. Rev. B,* 57[9] 5093-97 (1998).

127. R. E. A. McKnight, T. Moxon, A. Buckley, P. A. Taylor, T. W. Darling, and M. A. Carpenter, "Grain size dependence of elastic anomalies accompanying the alpha-beta phase transition in polycrystalline quartz," *J. Phys.-Condes. Matter,* 20[7] 18 (2008).

128. Z. Zhang, J. Koppensteiner, W. Schranz, and M. A. Carpenter, "Anelastic loss behaviour of mobile microstructures in srzr1-xtixo3 perovskites," *J. Phys.-Condes. Matter,* 22[29] (2010).

129. S. J. Zhang, R. Xia, L. Lebrun, D. Anderson, and T. R. Shrout, "Piezoelectric materials for high power, high temperature applications," *Mater. Lett.*, 59[27] 3471-75 (2005).

130. J. F. Tressler, S. Alkoy, and R. E. Newnham, "Piezoelectric sensors and sensor materials," *J. Electroceram.*, 2[4] 257-72 (1998).

131. R. A. Wolf and S. Trolier-McKinstry, "Temperature dependence of the piezoelectric response in lead zirconate titanate films," *Journal of Applied Physics*, 95[3] 1397-406 (2004).

132. T. Goto and O. L. Anderson, "Apparatus for measuring elastic-constants of single-crystals by a resonance technique up to 1825-k," *Review of Scientific Instruments*, 59[8] 1405-08 (1988).

133. T. Goto, O. L. Anderson, I. Ohno, and S. Yamamoto, "Elastic-constants of corundum up to 1825-k," *Journal of Geophysical Research-Solid Earth and Planets*, 94[B6] 7588-602 (1989).

134. J. B. Wachtman and D. G. Lam, "Young modulus of various refractory materials as a function of temperature," *Journal of the American Ceramic Society*, 42[5] 254-60 (1959).

135. X. F. Fan, E. D. Case, Q. Yang, and J. D. Nicholas, "Room temperature elastic properties of gadolinia-doped ceria as a function of porosity," *Ceram. Int.*, 39[6] 6877-86 (2013).

136. D. Hardy and D. J. Green, "Mechanical-properties of a partially sintered alumina," *J. Eur. Ceram. Soc.*, 15[8] 769-75 (1995).

137. Z. W. Cui, Y. Sun, Y. J. Chen, and J. M. Qu, "Semi-ab initio interionic potential for gadolinia-doped ceria," *Solid State Ion.,* 187[1] 8-18 (2011).

138. Z. W. Cui, Y. Sun, and J. M. Qu, "Thermomechanical properties of non-stoichiometric gadolinium doped ceria by molecular dynamics simulations," *Journal of Computational and Theoretical Nanoscience,* 10[6] 1359-65 (2013).

139. Y. Sun, C. Wang, and Y. J. Chen, "Molecular dynamics simulations of the deformation behavior of gadolinia-doped ceria solid electrolytes under tensile loading," *J. Power Sources,* 233 131-38 (2013).

140. P. Gao, Bolon A.M., Tanej Pathak, M., Xie, Z., Orlovskaya, N., and Radovic, M., "Thermal expansion and elastic moduli of electrolyte materials for high and intermediate temperature solid oxide fuel cell," *Solid State Ion.,* Under Review (2016).

141. A. M. Bolon, Gao, P. and Radovic, M., "Study of anelastic relaxation in stabilized zirconias by resonant ultrasound spectroscopy," *In preparation* (2016).

142. J. R. Kelly and I. Denry, "Stabilized zirconia as a structural ceramic: An overview," *Dental Materials,* 24[3] 289-98 (2008).

143. S. Fabris, A. T. Paxton, and M. W. Finnis, "A stabilization mechanism of zirconia based on oxygen vacancies only," *Acta Mater.,* 50[20] 5171-78 (2002).

144. R. Devanathan, W. J. Weber, S. C. Singhal, and J. D. Gale, "Computer simulation of defects and oxygen transport in yttria-stabilized zirconia," *Solid State Ion.,* 177[15-16] 1251-58 (2006).

145. Y. Arachi, H. Sakai, O. Yamamoto, Y. Takeda, and N. Imanishai, "Electrical conductivity of the zro2-ln(2)o(3) (ln = lanthanides) system," *Solid State Ion.*, 121[1-4] 133-39 (1999).

146. P. S. Manning, J. D. Sirman, R. A. DeSouza, and J. A. Kilner, "The kinetics of oxygen transport in 9.5 mol % single crystal yttria stabilised zirconia," *Solid State Ion.*, 100[1-2] 1-10 (1997).

147. M. Martin, "On the ionic conductivity of strongly acceptor doped, fluorite-type oxygen ion conductors," *J. Electroceram.*, 17[2-4] 765-73 (2006).

148. V. V. Kharton, F. M. B. Marques, and A. Atkinson, "Transport properties of solid oxide electrolyte ceramics: A brief review," *Solid State Ion.*, 174[1-4] 135-49 (2004).

149. J. P. Goff, W. Hayes, S. Hull, M. T. Hutchings, and K. N. Clausen, "Defect structure of yttria-stabilized zirconia and its influence on the ionic conductivity at elevated temperatures," *Phys. Rev. B*, 59[22] 14202-19 (1999).

150. P. Li, I. W. Chen, and J. E. Pennerhahn, "X-ray-absorption studies of zirconia polymorphs .2. Effect of y2o3 dopant on zro2 structure," *Phys. Rev. B*, 48[14] 10074-81 (1993).

151. M. Weller, B. Damson, and A. Lakki, "Mechanical loss of cubic zirconia," *J. Alloy. Compd.*, 310 47-53 (2000).

152. M. Weller and A. Lakki, "Defects in cubic zirconia studied by mechanical loss spectroscopy," *Ber. Bunsen-Ges. Phys. Chem. Chem. Phys.*, 101[9] 1297-302 (1997).

153. W. Araki and Y. Arai, "Oxygen diffusion in yttria-stabilized zirconia subjected to uniaxial stress," *Solid State Ionics,* 181[8-10] 441-46 (2010).

154. M. Weller, "Mechanical loss measurements on yttria-stabilized and calcia-stabilized zirconia," *J. Alloy. Compd.,* 212 66-70 (1994).

155. J. Kondoh and H. Shiota, "Frequency dispersion of the internal friction in tetragonal and cubic zirconia polycrystals stabilized with yttria," *J. Mater. Sci.,* 38[17] 3689-94 (2003).

156. J. Kondoh, H. Shiota, S. Kikuchi, Y. Tomii, Y. Ito, and K. Kawachi, "Changes in aging behavior and defect structure of y2o3 fully stabilized zro2 by in2o3 doping," *J. Electrochem. Soc.,* 149[8] J59-J72 (2002).

157. M. Weller, F. Khelfaoui, M. Kilo, M. A. Taylor, C. Argirusis, and G. Borchardt, "Defects and phase transitions in yttria- and scandia-doped zirconia," *Solid State Ion.,* 175[1-4] 329-33 (2004).

158. H. Fujimori, M. Yashima, M. Kakihana, and M. Yoshimura, "Beta-cubic phase transition of scandia-doped zirconia solid solution: Calorimetry, x-ray diffraction, and raman scattering," *Journal of Applied Physics,* 91[10] 6493-98 (2002).

159. N. Orlovskaya, S. Lukich, G. Subhash, T. Graule, and J. Kuebler, "Mechanical properties of 10 mol% sc2o3-1 mol% ceo2-89 mol% zro2 ceramics," *J. Power Sources,* 195[9] 2774-81 (2010).

160. A. Migliori and J. L. Sarrao, "Resonant ultrasound spectroscopy: Applications to physics, materials measurements, and nondestructive evaluation." Wiley: New York, (1997).

161. J. L. Sarrao, D. Mandrus, A. Migliori, Z. Fisk, I. Tanaka, H. Kojima, P. C. Canfield, and P. D. Kodali, "Complete elastic-moduli of la2-xsrxcuo4 (x=0.00 and 0.14) near the tetragonal-orthorhombic structural phase-transition," *Phys. Rev. B,* 50[18] 13125-31 (1994).

162. K. Foster, R. G. Leisure, and A. V. Skripov, "An ultrasonic study of hydrogen (deuterium) motion in the c-15 laves phase compound tav2h(d)(x)," *J. Phys.-Condes. Matter,* 11[3] 799-806 (1999).

163. K. Foster, J. E. Hightower, R. G. Leisure, and A. V. Skripov, "Ultrasonic attenuation and dispersion due to hydrogen motion in the c15 laves-phase compound tav2hx," *J. Phys.-Condes. Matter,* 13[33] 7327-41 (2001).

164. Z. Y. Zhang, J. Koppensteiner, W. Schranz, D. Prabhakaran, and M. A. Carpenter, "Strain coupling mechanisms and elastic relaxation associated with spin state transitions in lacoo3," *J. Phys.-Condes. Matter,* 23[14] 12 (2011).

165. A. M. Bolon, Mahaffey, P., Benetiz, R., Gao, P., and Radovic, M., "Resonant ultrasound spectroscopy for determining elastic properties of solids at high temperatures," *In preparation* (2016).

166. A. S. C20-00, "Standard test methods for apparent porosity, water absorption, apparent specific gravity, and bulk density of burned refractory brick and shapes by boiling water." in. ASTM International, West Conshohocken, PA, 2015.

167. M. Radovic and E. Lara-Curzio, "Mechanical properties of tape cast nickel-based anode materials for solid oxide fuel cells before and after reduction in hydrogen," *Acta Mater.*, 52[20] 5747-56 (2004).

168. M. Radovic and E. Lara-Curzio, "Elastic properties of nickel-based anodes for solid oxide fuel cells as a function of the fraction of reduced nio," *Journal of the American Ceramic Society*, 87[12] 2242-46 (2004).

169. P. Gudlur, A. Forness, J. Lentz, M. Radovic, and A. Muliana, "Thermal and mechanical properties of al/al2o3 composites at elevated temperatures," *Mater. Sci. Eng. A-Struct. Mater. Prop. Microstruct. Process.*, 531 18-27 (2012).

170. J. F. Scott, E. K. H. Salje, and M. A. Carpenter, "Domain wall damping and elastic softening in srtio3: Evidence for polar twin walls," *Physical Review Letters*, 109[18] 5 (2012).

171. M. Wojdyr, "Fityk: A general-purpose peak fitting program," *Journal of Applied Crystallography*, 43 1126-28 (2010).

172. M. A. Carpenter, A. Buckley, P. A. Taylor, and T. W. Darling, "Elastic relaxations associated with the pm(3)over-barm-r(3)over-barc transition in laalo3: Iii. Superattenuation of acoustic resonances," *J. Phys.-Condes. Matter*, 22[3] 19 (2010).

173. E. L.-C. M. Radovic, R. Trejo, B. Armstrong, and C. Walls, "Elastic properties, equibiaxial strength and fracture toughness of 8mol%ysz electrolyte for sofc." in 28th Cocoa Beach Conference on Advanced Ceramics and Composites Ceramics. The American Ceramic Society, 2003.

174. A. M. Azad, S. A. Akbar, S. G. Mhaisalkar, L. D. Birkefeld, and K. S. Goto, "Solid-state gas sensors - a review," *J. Electrochem. Soc.,* 139[12] 3690-704 (1992).

175. M. Godickemeier and L. J. Gauckler, "Engineering of solid oxide fuel cells with ceria-based electrolytes," *J. Electrochem. Soc.,* 145[2] 414-21 (1998).

176. E. D. Wachsman and K. T. Lee, "Lowering the temperature of solid oxide fuel cells," *Science,* 334[6058] 935-39 (2011).

177. J. A. Kilner and M. Burriel, "Materials for intermediate-temperature solid-oxide fuel cells," pp. 365-93. in Annual review of materials research, vol 44, Vol. 44**.** *Annual review of materials research.* Edited by D. R. Clarke. Annual Reviews, Palo Alto, 2014.

178. N. Izu, W. Shin, I. Matsubara, and N. Murayama, "Development of resistive oxygen sensors based on cerium oxide thick film," *J. Electroceram.,* 13[1-3] 703-06 (2004).

179. Y. L. Xu, X. H. Zhou, and O. T. Sorensen, "Oxygen sensors based on semiconducting metal oxides: An overview," *Sens. Actuator B-Chem.,* 65[1-3] 2-4 (2000).

180. P. N. Dyer, R. E. Richards, S. L. Russek, and D. M. Taylor, "Ion transport membrane technology for oxygen separation and syngas production," *Solid State Ion.,* 134[1-2] 21-33 (2000).

181. J. A. Kilner and R. J. Brook, "A study of oxygen ion conductivity in doped nonstoichiometric oxides," *Solid State Ion.,* 6[3] 237-52 (1982).

182. S. Omar, E. D. Wachsman, J. L. Jones, and J. C. Nino, "Crystal structure-ionic conductivity relationships in doped ceria systems," *Journal of the American Ceramic Society,* 92[11] 2674-81 (2009).

183. A. S. Nowick, "Study of defect reactions in crystals by anelastic and dielectric relaxation," *Bulletin of the American Physical Society,* 13[11] 1392-& (1968).

184. R. A. Gerhardt and A. S. Nowick, "Ionic conductivity of ceo2 doped with various trivalent dopants," *Bulletin of the American Physical Society,* 25[3] 414-14 (1980).

185. A. S. Nowick, "Kinetics of anelastic and dielectric relaxation due to reacting point defects," *J. Phys. Chem. Solids,* 31[8] 1819-& (1970).

186. D. Y. Wang, D. S. Park, J. Griffith, and A. S. Nowick, "Oxygen-ion conductivity and defect interactions in yttria-doped ceria," *Solid State Ion.,* 2[2] 95-105 (1981).

187. A. V. Vaysleyb, B. S. Lim, and A. S. Nowick, "Study of ac conductivity in dilute ceo2:Y3+ ceramics,″ pp. 421-26 in Symposium on Solid State Ionics IV, at the 1994 MRS Fall Meeting. Vol. 369, *Materials Research Society Symposium Proceedings*. Mrs and S. M. D. M. S. N. Y. N. Columbia Univ. PITTSBURGH, (1995).

188. M. P. Anderson and A. S. Nowick, "Study of defect clusters in solid electrolyte ceo2-y2o3 by anelastic relaxation," *Bulletin of the American Physical Society,* 24[1] 68-68 (1979).

189. R. Gerhardtanderson, F. Zamaninoor, A. S. Nowick, C. R. A. Catlow, and A. N. Cormack, "Study of sc2o3-doped ceria by anelastic relaxation," *Solid State Ion.*, 9-10[DEC] 931-36 (1983).

190. A. S. Nowick, A. V. Vaysleyb, and I. Kuskovshy, "Universal dielectric response of variously doped ceo2 ionically conducting ceramics," *Phys. Rev. B,* 58[13] 8398-406 (1998).

191. R. Korobko, A. Patlolla, A. Kossoy, E. Wachtel, H. L. Tuller, A. I. Frenkel, and I. Lubomirsky, "Giant electrostriction in gd-doped ceria," *Advanced Materials,* 24[43] 5857-61 (2012).

192. D. Marrocchelli, S. R. Bishop, H. L. Tuller, and B. Yildiz, "Understanding chemical expansion in non-stoichiometric oxides: Ceria and zirconia case studies," *Adv. Funct. Mater.*, 22[9] 1958-65 (2012).

193. S. Ling, "High-concentration point-defect chemistry - statistical-thermodynamic approach applied to nonstoichiometric cerium dioxides," *Phys. Rev. B,* 49[2] 864-80 (1994).

194. A. Migliori, J. L. Sarrao, W. M. Visscher, T. M. Bell, M. Lei, Z. Fisk, and R. G. Leisure, "Resonant ultrasound spectroscopic techniques for measurement of the elastic-moduli of solids," *Physica B,* 183[1-2] 1-24 (1993).

195. R. D. Shannon, "Revised effective ionic-radii and systematic studies of interatomic distances in halides and chalcogenides," *Acta Crystallographica Section A,* 32[SEP1] 751-67 (1976).

196. J. Faber, C. Geoffroy, A. Roux, A. Sylvestre, and P. Abelard, "A systematic investigation of the dc-electrical conductivity of rare earth doped ceria," *Appl. Phys. A-Mater. Sci. Process.,* 49[3] 225-32 (1989).

197. P. Sarkar and P. S. Nicholson, "Electric field relaxation studies in the ceo2-y2o3 system," *J. Phys. Chem. Solids,* 50[2] 197-206 (1989).

198. D. Y. Wang and A. S. Nowick, "Dielectric relaxation from a network of charged defects in dilute ceo2-y2o3 solid-solutions," *Solid State Ion.,* 5[OCT] (1981).

199. J. A. Kilner, "Defects and conductivity in ceria-based oxides," *Chemistry Letters,* 37[10] 1012-15 (2008).

200. P. Sarkar and P. S. Nicholson, "Electric relaxation studies of defects and defect associates in dilute ceria lanthanum oxide solid solutions," *Journal of the American Ceramic Society,* 72[8] 1447-49 (1989).

201. S. R. Wang, T. Kobayashi, M. Dokiya, and T. Hashimoto, "Electrical and ionic conductivity of gd-doped ceria," *J. Electrochem. Soc.,* 147[10] 3606-09 (2000).

202. P. P. Dholabhai and J. B. Adams, "A blend of first-principles and kinetic lattice monte carlo computation to optimize samarium-doped ceria," *J. Mater. Sci.,* 47[21] 7530-41 (2012).

203. P. P. Dholabhai, J. B. Adams, P. Crozier, and R. Sharma, "Oxygen vacancy migration in ceria and pr-doped ceria: A dft plus u study," *J. Chem. Phys.,* 132[9] 8 (2010).

204. A. S. Nowick, "Anelastic studies of intrinsic atomic defects," *J. Nucl. Mater.,* 69-7[1-2] 215-27 (1978).

205. R. Pornprasertsuk, P. Ramanarayanan, C. B. Musgrave, and F. B. Prinz, "Predicting ionic conductivity of solid oxide fuel cell electrolyte from first principles," *Journal of Applied Physics,* 98[10] 8 (2005).

206. A. Kushima and B. Yildiz, "Role of lattice strain and defect chemistry on the oxygen vacancy migration at the (8.3%y2o3-zro2)/srtio3 hetero-interface: A first principles study," *Solid Oxide Fuel Cells 11 (Sofc-Xi),* 25[2] 1599-609 (2009).

207. A. Predith, G. Ceder, C. Wolverton, K. Persson, and T. Mueller, "Ab initio prediction of ordered ground-state structures in zro2-y2o3," *Phys. Rev. B,* 77[14] 7 (2008).

208. M. Weller, "Point defect relaxations," *Mechanical Spectroscopy Q-1 2001,* 366-3 95-137 (2001).

209. W. K. Lee, R. Gerhardt, and A. S. Nowick, "Anelastic and dielectric-relaxation of scandia-doped ceria," *Journal De Physique,* 48[C-8] 251-56 (1987).

210. A. K. Jonscher, "Dielectric relaxation in solids," *Journal of Physics D-Applied Physics,* 32[14] R57-R70 (1999).

211. A. S. Nowick and B. S. Lim, "Electrical relaxations: Simple versus complex ionic systems," *Phys. Rev. B,* 63[18] 7 (2001).